TWO-DIMENSIONAL MODELLING OF THE HALL THRUSTER DISCHARGE: FINAL REPORT

Authors:

> E. Ahedo
>
> D. Escobar

with contributions from:

> A. Antón
>
> F. Parra
>
> V. de Pablo

E.T.S.I. AERONÁUTICOS
UNIVERSIDAD POLITÉCNICA DE MADRID
SPAIN

Final Report, September 10th, 2007.

REPORT DOCUMENTATION PAGE

Form Approved OMB No. 0704-0188

Public reporting burden for this collection of information is estimated to average 1 hour per response, including the time for reviewing instructions, searching existing data sources, gathering and maintaining the data needed, and completing and reviewing the collection of information. Send comments regarding this burden estimate or any other aspect of this collection of information, including suggestions for reducing the burden, to Department of Defense, Washington Headquarters Services, Directorate for Information Operations and Reports (0704-0188), 1215 Jefferson Davis Highway, Suite 1204, Arlington, VA 22202-4302. Respondents should be aware that notwithstanding any other provision of law, no person shall be subject to any penalty for failing to comply with a collection of information if it does not display a currently valid OMB control number.
PLEASE DO NOT RETURN YOUR FORM TO THE ABOVE ADDRESS.

1. REPORT DATE *(DD-MM-YYYY)*	2. REPORT TYPE	3. DATES COVERED *(From – To)*
25-09-2007	Final Report	1 August 2006 - 01-Aug-07

4. TITLE AND SUBTITLE	5a. CONTRACT NUMBER
Two dimensional modeling of Hall thruster discharge	FA8655-06-1-3032
	5b. GRANT NUMBER
	5c. PROGRAM ELEMENT NUMBER

6. AUTHOR(S)	5d. PROJECT NUMBER
Professor EDUARDO A Ahedo	
	5d. TASK NUMBER
	5e. WORK UNIT NUMBER

7. PERFORMING ORGANIZATION NAME(S) AND ADDRESS(ES)	8. PERFORMING ORGANIZATION REPORT NUMBER
Universidad Politécnica de Madrid ETSI Aeronauticos Plaza Cardenal Cisneros Madrid 28040 Spain	N/A

9. SPONSORING/MONITORING AGENCY NAME(S) AND ADDRESS(ES)	10. SPONSOR/MONITOR'S ACRONYM(S)
EOARD Unit 4515 BOX 14 APO AE 09421	
	11. SPONSOR/MONITOR'S REPORT NUMBER(S) Grant 06-3032

12. DISTRIBUTION/AVAILABILITY STATEMENT
Approved for public release; distribution is unlimited. (approval given by local Public Affairs Office)

13. SUPPLEMENTARY NOTES

14. ABSTRACT

A model of the plasma interaction with the dielectric walls of a Hall thruster has been presented. It accounts for partial thermalization of the electron population through a single parameter ¾ and includes a two-population, four-parameter model for SEE. Analytical expressions are obtained for the main parameters characterizing that interaction, such as the particle and energy fluxes to the walls and sheaths, which are needed as boundary conditions of quasineutral models of the full discharge.

The behavior for low thermalization is shown to differ greatly from the commonly-used, high-thermalization case. This is very relevant for Hall thrusters, where there is a growing conviction that electron thermalization is low. At low thermalization, energy losses are close to its minimum, the charge saturation limit is not attainable, and the sheath potential is small; the different roles of beam and primary electrons on these characteristics have been analyzed. Significant decreases of the parallel temperature of primary electrons and, therefore, of the plasma flux into the sheath take place only at the very-low thermalization limit.

The investigation of the emission model for secondary electrons has shown that the presence of a relevant fraction of elastically reflected electrons affects greatly the response. They tend to amplify the relative densities of untrapped electrons; their effect on the net primary and beam fluxes comes out from the zero electrical current balance. It is reiteratively found that the role of the sheath potential fall is to adjust the primary electron flux to wall and not vice versa. Although most of the analysis is carried out for an energy-independent yield of reflected electrons, a temperature-dependent yield expression is proposed, which avoids integrals expressions at the same time that it recovers approximately the reduction of that yield with the impact energy.

15. SUBJECT TERMS
Plasma Physics, Hall effect thrusters, EOARD

16. SECURITY CLASSIFICATION OF:			17. LIMITATION OF ABSTRACT	18, NUMBER OF PAGES	19a. NAME OF RESPONSIBLE PERSON
a. REPORT	b. ABSTRACT	c. THIS PAGE	UL	118	BARRETT A. FLAKE
UNCLAS	UNCLAS	UNCLAS			**19b. TELEPHONE NUMBER** *(Include area code)* +44 (0)1895 616144
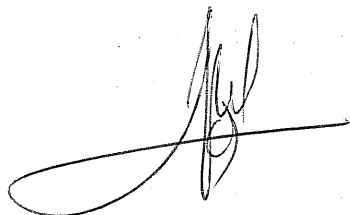
Standard Form 298 (Rev. 8/98)
Prescribed by ANSI Std. Z39-18

The views and conclusions contained herein are those of the authors and should not be interpreted as necessarily representing the official policies or endorsements, either expressed or implied, of the Air Force Office of Scientific Research or the U.S. Government.

The Contractor, UNIVERSIDAD POLITECNICA DE MADRID, hereby declares that, to the best of its knowledge and belief, the technical data delivered herewith under Award No. FA8655-06-1-3032 is complete, accurate, and complies with all requirements of the contract.

We certify that there were no subject inventions to declare during the performance of this award.

September 10, 2007

Eduardo Ahedo
Main Investigador

Gonzalo León
Vicerector for Research

Contents

List of Figures

List of Tables

Chapter 1

INTRODUCTION

1.1   Overview of the simulation code HPHall-2

HPHall-2[3] is a two-dimensional(2D), non-stationary, hybrid (PIC-fluid) and quasineutral code for Hall Effect Thruster (HET) simulation. Heavy species(ions and neutrals) are modelled with a particle-in-cell plus Monte-Carlo Collisions(PIC-MCC) method while electrons are modelled macroscopically. This procedure is a good trade-off between fully fluid models, which are not well suited for Hall thrusters where particle densities are too low, and fully kinetic models where computational time is enormous. In addition, HPHall-2 assumes cylindrical symmetry and lateral ceramic walls and uses an externally-imposed magnetic field, $\mathbf{B}$. Plasma quasi-neutrality is based on the Debye length being much smaller than typical lengths of Hall thrusters. Therefore, electron density and singly and doubly charged ion densities are directly related. However, due to boundary conditions the quasi-neutrality assumption is not valid in very thin layers, called sheaths, tied to the walls. As a consequence the boundaries of the simulation domain are not the walls but the transition surfaces to the space-charge sheaths tied to the chamber walls. This requires to solve independently in a sheath subcode the different sheath problems in order to determine the correct conditions at the boundaries of the quasineutral domain. Figure 1.1 shows the different elements of the simulated thruster, the mesh used by the PIC part of the code, the magnetic field profile at the channel median, and the magnetic streamsurfaces used by the electron subcode.

PIC methods simulate species as a group of macroparticles, each one of them representing a large number of particles. Macro-particle motion is computed by integrating Newton´s law while collision processes, such as ionization or charge exchange collisions, are modelled using a Monte-Carlo Collision algorithm. Forces acting on particles are due to the electric field, the externally applied magnetic field and ion-neutral collisions. Macroscopic magnitudes for ions and neutrals (density, flux, temperature,...) are computed by weighting particle magnitudes at every node of the mesh. Typical numbers are macro-particles 30.000 per species (neutrals, singly charged ions and doubly charged ions) and about 1000 cells in the mesh.

The strong magnetic field causes a high anisotropy in the electron macroscopic dynamics, which allows to treat the directions parallel and perpendicular to $\mathbf{B}$ in different manner. In particular, Boltzmann equilibrium is assumed along magnetic lines while an Ohm's law (with pressure effects) is used in the perpendicular direction. The 2D energy equation is transformed into a 1D problem by first integrating electron equations along the magnetic field lines.
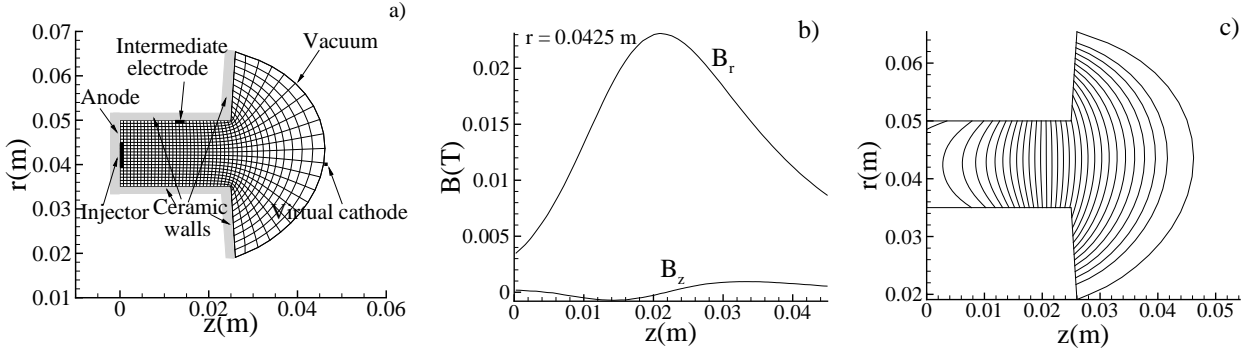
Figure 1.1: Elements of the simulated SPT-100 type simulated thruster and PIC-mesh(a), reference magnetic field at the chamber median, B_r and B_z are the radial and axial components respectively(b) and magnetic streamsurfaces used in the electron-mesh(c).

The main outputs of the PIC sub-code are densities and particle fluxes computed by weighting algorithms. These values are needed by the electron sub-code that, in turn, computes the electron temperature, necessary to evaluate collisional processes, and the electric potential, which defines the electric field to be applied on ions.

1.2 Objectives of the project

This project is aimed to improve HPHall-2 (as delivered in grant FA8655-04-1-3003) in two categories of objectives:

1. A better modelization and more accurate algorithms of the main phenomena of the discharge. This includes:

   (a) Detailed treatment of the near anode region for oblique magnetic fields. The difficulty lies in matching the 1D electron equations at each magnetic line to the anode sheath boundary, which is not a magnetic streamline. The handling of boundary conditions for the case of an anode sheath, that can be electron-repelling in certain zones and ion-repelling in others, is an important issue, partially unsolved yet.

   (b) Implementation of more accurate sheath models.

   (c) Improvement of algorithms for moving and injecting particles in the PIC subcode. The objective is a reduction of temporal errors by one-order of magnitude. Apart from obtaining a higher accuracy, this will allow to carry out long runs and numerically-reliable parametric studies.

   (d) Improvement of magnitude weighting at the domain boundaries.

   (e) The development of a more accurate electron subcode. A new differential formulation of the electron equations, totally based on curvilinear magnetic coordinates is being derived. Modified algorithms try to increase the spatial and temporal accuracy of the solution. Effects previously neglected like electric work parallel to B-lines are being included. A modification of the constant-temperature, Boltzmann equilibrium

model in the B-parallel direction and a more detailed model of anomalous diffusion are pending on advances on parallel researches.

2. To increase the capabilities of the code.

   (a) High specific impulse performances. Double ions become a significant population at high discharge voltages. The new code includes double ions at a separate species. Effects of double ions on the sheath conditions are included too. A higher flexibility on the magnetic meshes to be managed by the electron subcode is necessary.

   (b) Two-stage discharges. This consists mainly on considering the presence of internal electrodes in certain regions of the inner or outer walls. The implications for the code are: (1) another major modification on the electron subcode, since the discharge current cannot be considered constant along all magnetic streamlines; (2) the formulation of a sheath model for different electrode types, in particular for highly-emissive ones.

1.3 Organization of the report

The changes implemented in the code are detailed in chapters 2 to 6. Chapter 2 is devoted to changes in the general structure of the code and in the pre-process subroutines (mesh and wall definitions, etcetera). Chapters 3 to 5 are devoted to explain the theoretical advances that have been implemented in the sheath, PIC, and electron subcodes, respectively. Chapter 6 illustrates some of the capabilities of the new version. Finally Annexes A and B present on-going theoretical advances that have not been implemented in the code yet.

Chapter 2

GENERAL FEATURES OF THE CODE

2.1   Improved code structure

HPHall-2 has been modified in order to make it easy-to-use by people not familiar with the computational code itself. It has been divided into several applications each one of them designed to perform a different task. In this manner, there are separate programs to:

- load a spatial grid computed with TecPlot and generate a file in the format required by HPHall.

- load a magnetic field computed with Maxwell and generate a file in the format required by HPHall.

- generate a magnetic field file in the format required by HPHall based on a theoretical law that can be defined by the user.

- generate files containing tables that represent the wall interaction models.

- execute HPHall using the different files generated in the previous steps as well as other physical and numerical parameters contained in a unique file.

Apart from the files generated by the previous applications, HPHall needs one input file where both physical constants (e.g. Xenon properties) and numerical parameters (e.g. ion and electron time steps) are defined. In this way, the whole execution can be set up from one single file. The main variables that must be defined in this file are shown in several tables at the end of this chapter.

HPHall generates as output self-explanatory data files that can be analyzed either using TecPlot or a simple text editor. For instance, the program generates an output file containing the main parameters regarding thruster operation: efficiency, thrust, power, discharge voltage, etc. Besides, several files are generated containing different spatial and temporal profiles for both wall properties and plasma magnitudes inside the thruster. All this files are generated in an independent directory so that results from different executions can be compared easily.

2.2   New algorithm to compute the magnetic grid

HPHall-2 solves electron equations using a 'magnetic grid' derived from the magnetic field topology and the spatial grid. However, it fails to compute properly this magnetic grid and consequently, errors are propagated to the electron equations.

In order to solve that problem a new algorithm has been implemented that ensures the magnetic grid is computed consistently. In fact, this new algorithm is more consistent with the geometrical grid because it reproduces any grid refinement that may appear near the lateral walls.

Figure(2.1) depicts a comparison between the magnetic grids obtained using the algorithm in HPHall-2 and the new one. HPHall-2 fails to reproduce properly the lateral walls as well as the near plume region. This fact causes wall properties are not evaluated in the wall but inside the computational domain. Thus plasma-wall interaction properties are not computed accurately.
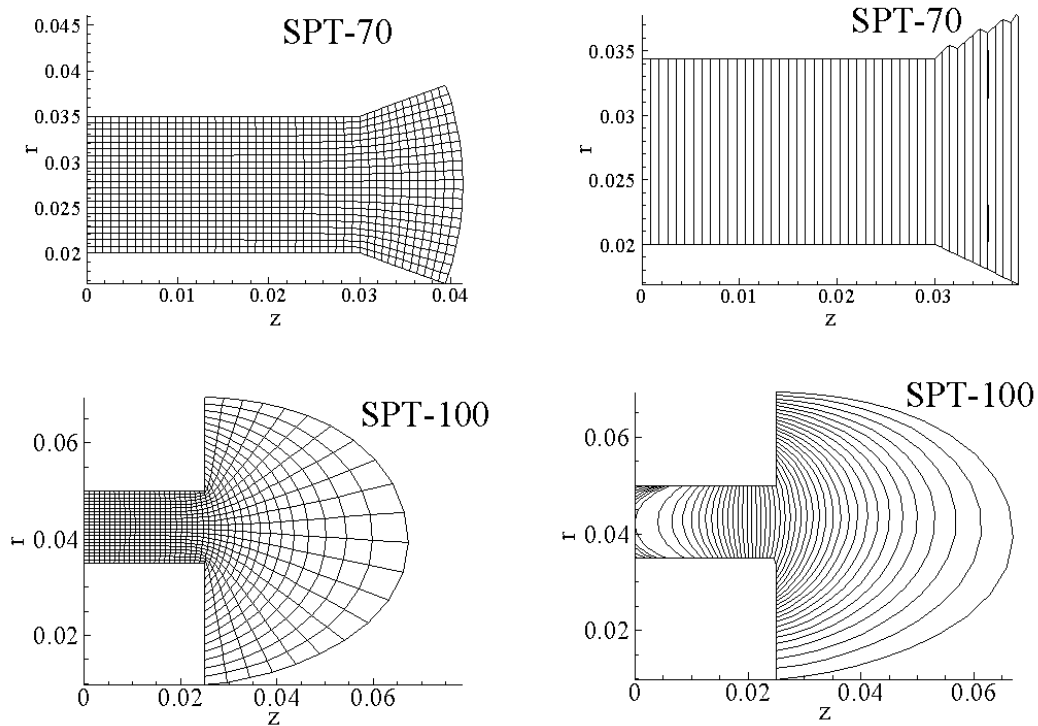
Figure 2.1: Spatial(left) and magnetic(right) grids computed by HPHall-2 (upper figures) for the SPT-70 thruster and computed by the new version with the new algorithm (lower figures) for the SPT-100 thruster.

In the upper figures (i.e., SPT-70 figures) it can be observed that the algorithm implemented in HPHall-2 does not compute accurately the simulation domain and the near plume region upper limits. In fact, the upper lateral wall should be at 0.035 m from the centerline (see geometric grid) while the magnetic grid does not reach that value at any point. On the other hand, the new algorithm (i.e., SPT-100 figures) generates a magnetic grid completely equivalent to the geometric grid.

2.3   Channel geometry with curved walls

Another interesting improvement is the added capability of the new code to deal with curved walls. This is interesting in case the influence of wall erosion is to be analyzed on thruster performance.

Figure 2.2 shows the results obtained with the new code for both a curved and non-curved wall. Obviously, to make full profit of this improvement a sputtering algorithm must be implemented to compute the wall erosion rate. However, this is out of the scope of the current project.

As expected, as the cross section area increases near the exit, the plasma density decreases, the ion flux is spread and the temperature decreases.
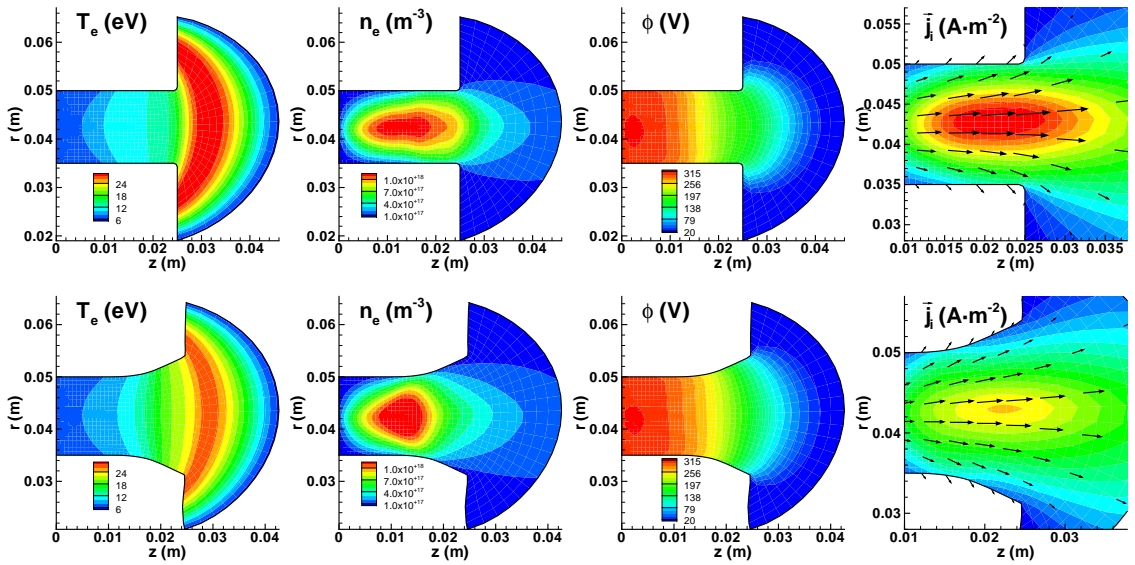
Figure 2.2: 2D maps comparing results for curved and non-curved walls.

2.4   Local definition of wall properties

In order to increase the capabilities of the code an additional feature has been added. Now it is possible to define as many different materials (or even different models for the same material) as desired. This is controlled in HPHall main input file. In this file there is a group of variables that can be used to define the different material geometries, properties, models, etc. At the end of the chapter the main values to be defined are presented in a table. The different wall segments made of a given material must be defined with r and z coordinates. Besides, each material must have specified the material name, type and file containing the plasma-wall interaction table.

In the last chapter results are presented for a two-stage thruster where an intermediate electrode (modeled as an ideal electron emitter) is presented. This is a good example of the flexibility allowed with this new feature.

Parameter name	Value	Description
B_FILE	mag_SPT100.dat	magnetic field input file
GRID_TECPLOT_FILE	grid_SPT100.dat	grid input file

Table 2.1: HPHall input parameters (INPUT FILES).

Parameter name	Value	Description
RUN_MODE	0	0 = normal, 1 = neut., 2 = ions, 3 = particles
N_ITS	10000	number of iterations
TRANSIENT_ITS	0	number of iterations considered as transient
SAVE_ITS	2000	save data every x iterations
CONCATENATE	0	concatenate averaged values
N_CONCAT_ITS	0	number of previous iterations to concatenate

Table 2.2: HPHall input parameters (PROGRAM FLOW).

Parameter name	Value	Description
MOVIES	0	save movies
MOVIE_ITS	50	save movie frame every x iterations
MOVIE_FLUID	1	save fluid movie
MOVIE_PARTICLE	0	save particle movie
N_IONS_MOVIE	1000	number of ions for the particle movie
N_NEUTRALS_MOVIE	1000	number of neutrals for the particle movie

Table 2.3: HPHall input parameters (MOVIES).

Parameter name	Value	Description
SAVE_ELECTRON_INFO	0	save electron information (y/n)
SAVE_ELECTRON_ITS	1	save electron information every x electron iterations

Table 2.4: HPHall input parameters (ELECTRON MOVIE AND MAP).

Parameter name	Typical value	Description
PROPELLANT	2	ARGON: 1 XENON: 2
M_DOT	4.8e-6	mass flow rate in kg/s
PPU_TYPE	1	CONSTANT_VOLTAGE=1 CONSTANT_CURRENT=2 CONSTANT_POWER=3
V_DISCHARGE	300.0	discharge voltage (for constant voltage)
I_DISCHARGE	6.5	total current at cathode (for constant current)
P_DISCHARGE	2000	total power (for constant power)

Table 2.5: HPHall input parameters (OPERATION PARAMETERS).

Parameter name	Value	Description
WALL_FLUX_V_BBC	1	wall normal velocity is defined using the wall flux
CORRECTED_WEIGHTING	0	new algorithms to weight at the boundaries
SURFACE_WEIGHTING	1	new algorithms to weight at boundaries
BOHM_FORCING	0	apply Bohm forcing algorithm
ANODE_BOHM_FORCING	0	anode is included in bohm forcing
NEW_IONIZATION_LAW	1	new ionization law for particle number control
NEW_CATHODE	0	new cathode model

Table 2.6: HPHall input parameters (MODELLING OPTIONS).

Parameter name	Value	Description
N_MATS	3	number of different materials
WALL_TYPE_1	1	anode(1), ceramic(2), electrode(3), cathode(4)
MATERIAL_NAME_1	Anode_ERF_200eV	material-model name
SEE_COEFF_P_1	0.000	SEE law coefficient p (meaningless for anode)
SEE_E1_1	0.000	SEE law energy (J) (meaningless for anode)
N_SEGMENTS_1	1	segment number for material 1
Z_BEGIN_1_1	0.0000	z-coordinate of segment 1 starting point
R_BEGIN_1_1	0.0350	r-coordinate of segment 1 starting point
Z_END_1_1	0.0000	z-coordinate of segment 1 ending point
R_END_1_1	0.0500	r-coordinate of segment 1 ending point
POTENTIAL_1_1	0.0	potential(V) (meaningless for ceramic material)
WALL_TYPE_2	2	
MATERIAL_NAME_2	BN_ERF_200eV	
SEE_COEFF_P_2	0.576	
SEE_E1_2	7,63E-15	
N_SEGMENTS_2	4	
Z_BEGIN_1_2	0.0000	
R_BEGIN_1_2	0.035	
Z_END_1_2	0.0250	
R_END_1_2	0.035	
POTENTIAL_1_2	0.0	
Z_BEGIN_2_2	0.0000	
R_BEGIN_2_2	0.050	
Z_END_2_2	0.025	
R_END_2_2	0.050	
POTENTIAL_2_2	0.0	
Z_BEGIN_3_2	0.025	
R_BEGIN_3_2	0.035	
Z_END_3_2	0.025	
R_END_3_2	0.00977	
POTENTIAL_3_2	0.0	
Z_BEGIN_4_2	0.025	
R_BEGIN_4_2	0.050	
Z_END_4_2	0.025	
R_END_4_2	0.0693	
POTENTIAL_4_2	0.0	
WALL_TYPE_3	3	
MATERIAL_NAME_3	electrode	
SEE_COEFF_P_3	0.576	
SEE_E1_3	7,63E-15	
N_SEGMENTS_3	0	
Z_BEGIN_1_3	0.0250	
R_BEGIN_1_3	0.0580	
Z_END_1_3	0.0250	
R_END_1_3	0.0600	
POTENTIAL_1_3	0.0	

Table 2.7: HPHall material definition

Chapter 3

IMPROVEMENTS IN SHEATH SUBCODE

HPHall is a quasineutral code, the simulation boundaries are not the walls but the transition surfaces to the space-charge sheaths tied to the chamber walls. This requires to solve independently the different sheath problems in order to define the correct conditions at the boundaries of the quasineutral domain. This chapter explains the different models used for the different kinds of sheaths that can appear inside a Hall thruster: anode, ceramic-wall sheaths and intermediate electrodes.

3.1   Anode sheath

A simple sketch of the anode is represented in figure 3.1(a). Because of its thinness, of the order of the Debye length, the sheath is considered collisionless, quasisteady, and, in principle, negative (meaning electron-repelling). Since the wall is considered metallic, the role of this sheath is to adjust the small, diffusive electron flux coming from the quasineutral plasma to the electron flux collected by the (perfectly-absorbing) anode. Hence, the main sheath characteristics depend only on electrons.

The anode sheath model used by Fife, Ahedo et al.[4, 5] and other researchers assumes a full Maxwellian distribution of electrons at the sheath entrance (point B). This model is inaccurate since the anode does not return back the electrons reaching it. A drifted Maxwellian, as assumed by Ahedo[6], is incorrect too, since the distribution must be symmetric on the normal velocity for electrons that are reflected back within the sheath.

The correct choice, within the 'family' of Maxwellian distributions, is a truncated, zero-drift distribution. Thus, taking into account the energy conservation of the electrons within the sheath, one has

$$f_e(v_\perp, v_\parallel, \phi) = n_\star \left(\frac{m_e}{2\pi T_\star} \right)^{(3/2)} \exp \left(\frac{e(\phi - \phi_B)}{T_\star} \right) \exp \left(-\frac{m_e(v_\perp^2 + v_\parallel^2)}{2T_\star} \right) H \left(v_\perp + \sqrt{\frac{2e(\phi - \phi_A)}{m_e}} \right)$$

(3.1)
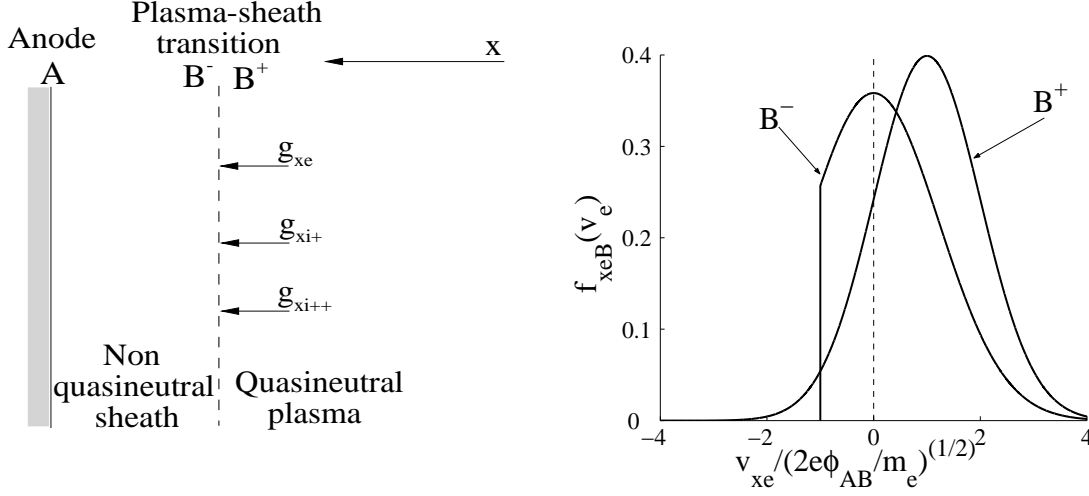
Figure 3.1: (a) Sketch of the anode sheath. (b) The truncated Maxwellian distribution at the sheath side of B, and the 'equivalent' drifted Maxwellian distribution corresponding to macroscopic magnitudes at the quasineutral side of B. In these figures the x axis represents the direction perpendicular to the wall

Here, f_e is the electron distribution function for the velocity component perpendicular to the anode surface, $v_\perp$, the parallel velocity component, $v_\parallel$, and the electric potential, ϕ, which plays the role of the spatial variable; $H(v)$ is the Heaviside step function of v; and $T_\star$ and $n_\star$ are constants characterizing the distribution. These constants are the temperature and density at B only in the limiting case of a non-truncated distribution.

Let us consider a one-dimensional problem where plasma magnitudes are constant along the whole surface transition B. If ϕ_{AB} is the sheath potential fall and taking the appropriate moments of f_e, the density, particle flux, temperature, and total energy flux to the sheath at point B are

$$n_{eB} = n_\star \frac{1 + \mathrm{erf}(\sqrt{e\phi_{AB}/T_\star})}{2}, \tag{3.2}$$

$$g_{\perp eB} = n_\star \sqrt{\frac{T_\star}{2\pi m_e}} \exp\left(-\frac{e\phi_{AB}}{T_\star}\right), \tag{3.3}$$

$$\frac{T_{eB}}{T_\star} = 1 + \frac{m_e u_{\perp eB}^2}{3T_\star} - \frac{2}{3\sqrt{\pi}}\left(\sqrt{\frac{2m_e u_{\perp eB}^2}{T_\star}} + \sqrt{\frac{e\phi_{AB}}{T_\star}}\right)\frac{\exp\left(-\frac{e\phi_{AB}}{T_\star}\right)}{1 + \mathrm{erf}(\sqrt{e\phi_{AB}/T_\star})}, \tag{3.4}$$

$$q_{\perp eB}^{tot} = g_{\perp eB}(2T_\star + e\phi_{AB}), \tag{3.5}$$

respectively, with $u_{\perp e} = g_{\perp e}/n_e$ the macroscopic electron velocity and $\mathrm{erf}(x)$ the error function.

These magnitudes must match with those known from the quasineutral macroscopic model at the sheath transition. Therefore, these four equations determine the potential fall ϕ_{AB}, the
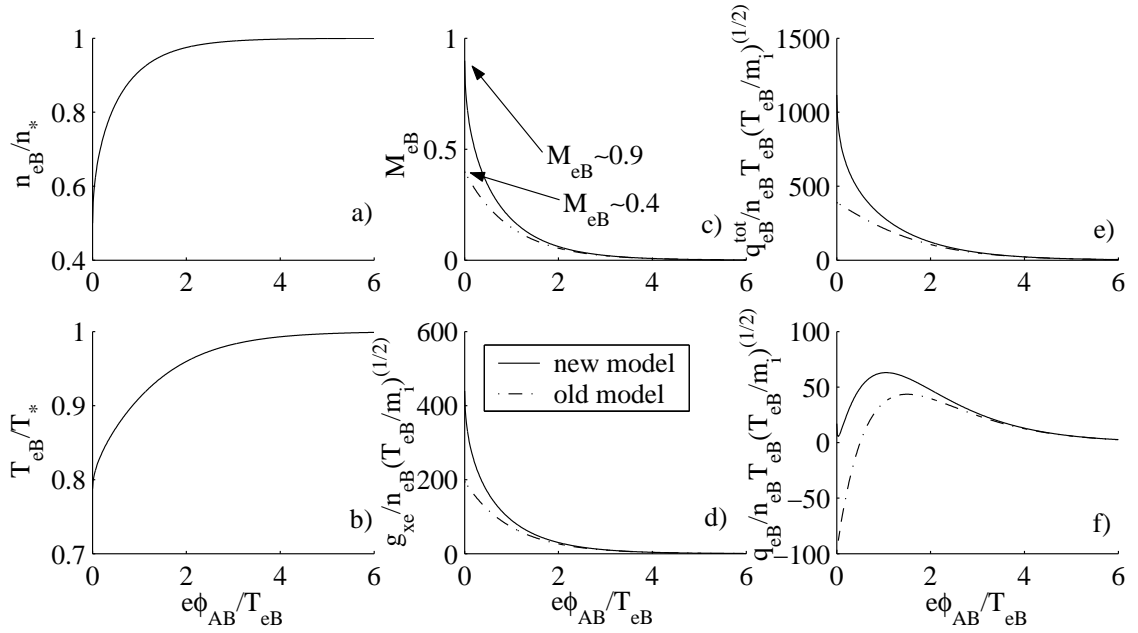
Figure 3.2: Comparison of anode models in terms of the non-dimensional electron density (a), non-dimensional electron temperature (b), electron Mach number (c), non-dimensional electron flux to anode (d), non-dimensional total energy flux to the anode (e) and non-dimensional heat flux to the anode (f).

constants of the distribution function, $n_\star$, $T_\star$, and the heat conduction flux to the sheath:

$$q_{\perp eB} = q_{\perp eB}^{tot} - \frac{5}{2} g_{\perp eB} T_{eB}$$

Figure 3.2 compares the sheath parameters for the new and old (i.e. full Maxwellian) sheath models. As expected, both models coincide exactly for an infinite sheath potential fall and approximately for $e\phi_{AB}/T_{eB} > 3$. The old model[7, 8] placed the transition to a no-sheath regime (i.e. $\phi_{AB}=0$) at $M_{eB} = (2\pi)^{-1/2} \simeq 0.4$, with $M_{eB} \equiv |u_{\perp eB}|/\sqrt{T_{eB}/m_e}$ the electron Mach number. The present model places it at $M_{eB} \sim 0.9$, much closer to $M_{eB} = 1$ where the quasineutral, macroscopic model of Ahedo [6] places the transition from a negative- to a positive- anode sheath (for near-cold ions). [A perfect parametric matching of the quasineutral and kinetic models is unlikely since they have been postulated independently.] Notice that the increment of $g_{\perp e}/n_{eB}$ and $q_{\perp eB}^{tot}/n_{eB}$ as the sheath vanishes is due to the increase of $u_{\perp eB}$ and decrease of n_{eB}, and not to changes of $g_{\perp e}$. Finally, another merit of the new model is that heat conduction to the anode is positive always; the old model predicted a negative heat conduction to the anode in the no-sheath limit, which did not look satisfactory.

In this analysis ions have played no role. The Bohm condition states that the ion flux must enter sonic-supersonically into a *negative* sheath. The fulfillment of this condition pertains to the PIC subcode and, particularly, to the topic of plasma weighting at the boundaries.

A recent improvement of this anode-sheath model, which places the vanishing of the negative sheath exactly at $M_{eB} = 1$ is presented in Annex A, but has not been implemented in the code yet.

3.2   Ceramic wall sheath

The sheath around ceramic walls is more complex, since (i) both the electron and ion dynamics must be taken into account, (ii) there is secondary electron emission (SEE) by electron impact in the walls, and (iii) space-charge saturation is possible[9].

Improvements on the sheath model are being implemented on three points. First, the use of truncated Maxwellian distribution for electrons, instead of the full Maxwellian distribution used originally by Hobbs and Wesson[9] and adopted by Ahedo[10]. Second, the inclusion of doubly-charged ions as an additional species, since they constitute a non-marginal population for high specific impulse operation [11, 1]. And third, the consideration of a supersonic ion flux as a likely sheath entrance condition, because of the discharge fluctuations. With respect to this last point, we know that the Bohm condition for the sheath states that ions must enter sonically or supersonically. At the same time, the stationary (and macroscopic) solution for the quasineutral plasma states that ions must enter into the sheath subsonically or sonically. However, supersonic ion fluxes are possible in a time-fluctuating quasineutral solution, as Parra et al.[12] showed. Finally observe that the sheath remains quasi-steady for a fluctuating discharge.
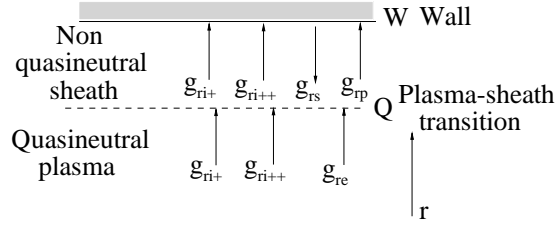
Figure 3.3: Sketch of ceramic wall fluxes and nomenclature.

The fundamentals of the improved model are those set by Ahedo[10] for total thermalization except, of course, for the aspects we want to improve. The issue of partial thermalization of the electron distribution is not treated here, thus, total thermalization is assumed. We omit here the derivation of the model and just include some notes on it. A sketch of the ceramic wall sheath is shown in figure 3.3. The plasma species within the sheath are: primary electrons(p) coming from the quasineutral plasma, secondary electrons(s) emitted by the wall, singly-charged ions($i+$) and doubly-charged ions($i++$). Primary and secondary electrons match into a single electron population (e) outside the sheath. Quasi cold beams are assumed for the non-confined populations ($i+$, $i++$, and s). The zero current condition leads to

$$g_{ri+W} + 2g_{ri++W} = (1 - \delta_w)g_{rpW}, \tag{3.6}$$

where g_r mean particle flux perpendicular to the (radial) wall, and δ_w is the effective SEE yield.

Plasma quasineutrality at the sheath entrance yields

$$n_{sQ} + n_{pQ} \equiv n_{eQ} = n_{i+Q} + 2n_{i++Q} \tag{3.7}$$

and the average ion charge number for ions at point Q is

$$Z_{iQ} = \frac{n_{eQ}}{n_{iQ}} = \frac{n_{i+Q} + 2n_{i++Q}}{n_{i+Q} + n_{i++Q}}. \tag{3.8}$$
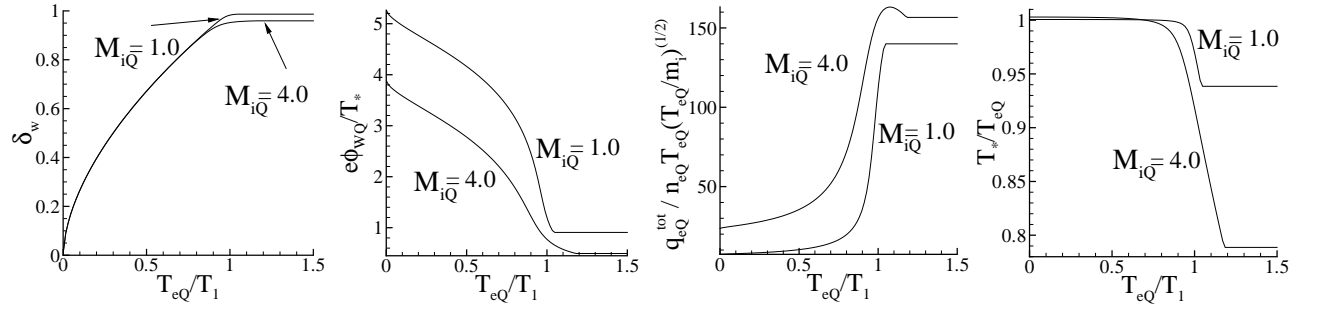
Figure 3.4: Ceramic material sheath model non-dimensional results and influence of the supersonic ion flow on the sheath properties.

When there is only one ion beam, the Bohm condition of the sheath is explicit for the ion macroscopic velocity, Eq.(18) of Ref.[10]. In the presence of singly-charged and doubly-charged ion beams the Bohm condition yields only one relation between the two beam velocities. A correct closure of the problem would require to involve the quasineutral solution, and this would be very costly. Two simple, alternative procedures are being studied. First, to take

$$u_{ri++Q} = \sqrt{2} u_{ri+Q} \qquad (3.9)$$

as if the two ion beams were accelerated freely in the presheath, with no ion production. Second, to consider a single ion beam of charge Z_{iQ}. Results here are presented for the first alternative.

The sheath potential fall, ϕ_{WQ}, turns out to verify

$$\frac{e\phi_{WQ}}{T_\star} = \ln \sqrt{\frac{m_i}{2\pi m_e}} + \ln(1 - \delta_w) + \ln\left(\frac{n_{pQ}}{n_{eQ}}\sqrt{\frac{T_\star}{T_{eQ}}}\right)$$

$$- \ln\left(2\sqrt{2} - 1 - 2(\sqrt{2} - 1)/Z_{iQ}\right) - \ln M_{iQ} - \ln \frac{1 + \mathrm{erf}\left(\sqrt{e\phi_{WQ}/T_\star}\right)}{2}, \quad (3.10)$$

where the second line groups the effects newly introduced: doubly-charge ions, $Z_{iQ} > 1$, supersonic ion flux $M_{iQ} = u_{i+Q}/\sqrt{T_{eQ}/m_i}$, and truncated Maxwellian distribution (based on 'temperature' $T_\star$) for primary electrons (yielding the term with the error function).

This new model depends on three dimensionless parameters coming from the quasineutral solution (i.e. from the simulation of the 2D discharge) and the wall material: T_{eQ}/T_1 (with T_1 the temperature for a 100% SEE yield[10]) M_{iQ}, and Z_{iQ}. Figure (3.4) shows that the ion Mach number is found to affect significantly the potential fall and, thus the energies of ions and electrons impacting the wall. The influence of the ion charge number can be interpreted as an increase of ion Mach number, as Eq. (3.10) shows. Since, according to Ref.[1], Z_{iQ} is between 1 and 1.1 its effect is small.

In the present model the charge saturation limit(CSL) is not universal, but depends on two parameters, M_{iQ} and Z_{iQ}. This is illustrated in figures (3.5) and (3.6). Both new effects tend to reduce the value of the SEE yield at the CSL, thus reducing the electron energy losses to the walls.

Finally, the use of a truncated distribution function for primary electrons at Q introduces modifications only at the CSL or close to it. For the basic case, $M_{iQ} = 1$ and $Z_{iQ} = 1$,
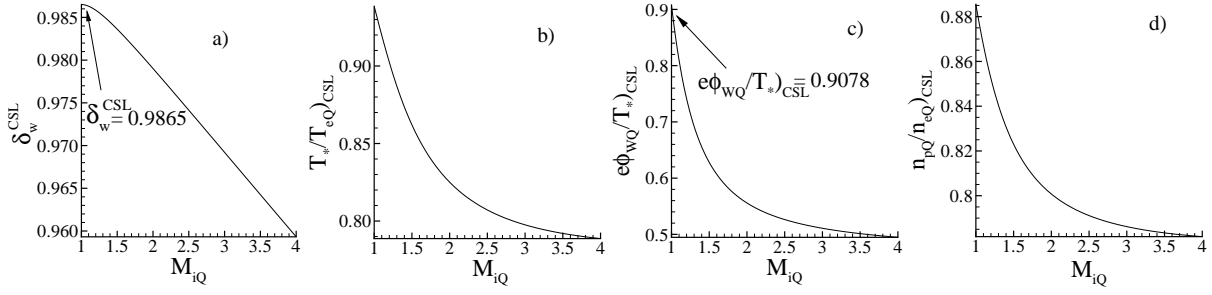
Figure 3.5: Influence of the ion Mach number on the properties at the saturation charge limit. SEE yield at CSL(a), non-dimensional temperature(b), non-dimensional sheath potential fall(c) and non-dimensional primary-electron density (d).
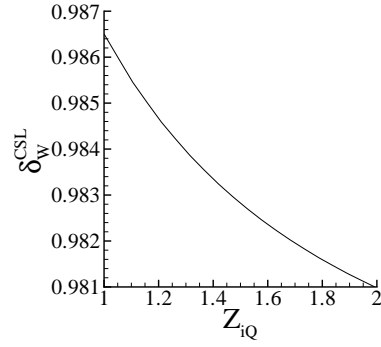
Figure 3.6: Influence of the equivalent charge number on the charge saturation limit.

Hobbs and Wesson had δ_W^{CSL} =0.983, whereas now we find δ_W^{CSL} =0.9865. One can be tempted to neglect this 0.3% difference on δ_W^{CSL}, unless one realizes that the important magnitude is $1/(1 - \delta_w^{CSL})$ which measures particle and energy fluxes to the walls. Then, one finds that the differences in energy deposition with Hobbs-Wesson amount to a 25% (larger in the present case).

Figure 3.7 displays a comparison of the results obtained with the simulation code of Ref.[1] using the old and new models for the lateral sheaths.
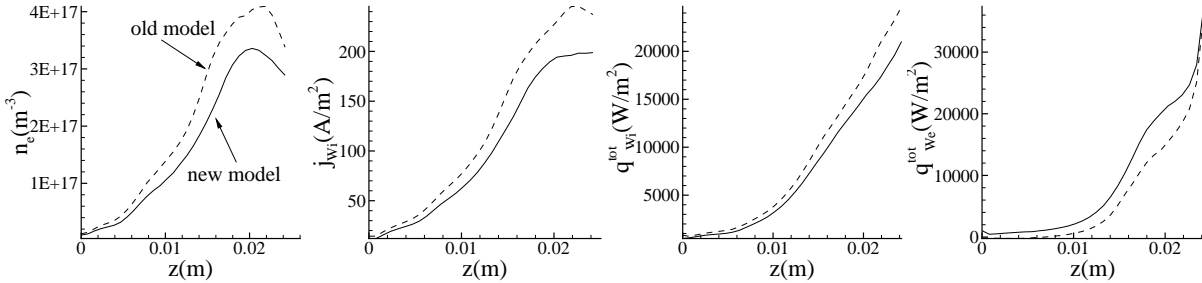
Figure 3.7: Plasma characteristics at the outer wall with the new (solid lines) and old (dashed lines) models for the lateral sheaths. The simulation data is the same used in Ref.[1].

3.3 Effects of electron partial thermalization

The sheath model at the lateral walls of the previous section is based on the assumption that the thermalization mean free-path for electrons is smaller than the channel width. In this case, the emitted beams of secondary electrons thermalize with the bulk electron population and the tail of electrons collected at one wall is quickly replenished. As a consequence, the velocity distribution function of 'primary' electrons flowing into the sheath edge can be considered semi-Maxwellian.

In practice, electron collisionality seems to be much smaller, and the electron velocity distribution function is more complex. A theory for the partial thermalization case is presented in Annex B. In the conclusions section of that Annex we comment on the pending work and the difficulties of implementing that theory in HPHall.

3.4 Sheath model for ideal electron emitter

Active electrodes are the preferred method when designing two-stage SPT-type Hall thrusters. Preferably this intermediate electrode is made of a high electron emissivity material.

This new element inside the chamber requires proper modelling and in particular, the plasma-wall interaction problem is modified with respect to the ceramic wall case treated in [10], [2] and in the previous section. The model we are implementing considers an active electrode operating continuously in the charge saturated regime(CSR) due to its high electron emissivity. The potential of the electrode should be a known parameter, whereas the electric current through the electrode would be the output. However, at present, and because of the unsteady behavior of the discharge potential, we are taken the electrode current as the known (and constant) parameter, and the electrode potential as the unknown.

Regarding the mathematical formulation of the model we can expect important similarities with respect to the ceramic wall model, including the usage of a truncated maxwellian distribution inside the sheath for primary electrons. In fact, the governing equations are the same except for a fundamental difference: the zero current condition is no longer applicable.

In the zero Debye-limit the sheath satisfies the following conservation equations:

- ion flux conservation: $g_{ri} = n_i u_{ri} = const = g_{riQ}$

- primary electron flux conservation: $g_{rp} = n_p u_{rp} = const = g_{rpW}$

- secondary electron flux conservation: $g_{rs} = n_s u_{rs} = const = g_{rsW}$

- ion energy conservation: $(1/2)m_i u_{ri}^2 + e\phi = const$

- secondary electron energy conservation: $(1/2)m_e u_{rs}^2 - e\phi = const \simeq -e\phi_W$

- primary electron Maxwell-Boltzmann equilibrium:

$$n_p(\phi) = n_{pQ} \exp\left(-\frac{e(\phi_Q - \phi)}{KT_p}\right) \frac{1 + erf(\sqrt{\frac{e(\phi - \phi_W)}{KT_p}})}{1 + erf(\sqrt{\frac{e\phi_{WQ}}{KT_p}})}$$

- primary electron semi-maxwellian wall flux:

$$g_{rpW}(\phi) = n_{pQ}\sqrt{\frac{KT_p}{2\pi m_e}}\exp\left(-\frac{e\phi_{WQ}}{KT_p}\right)\frac{2}{1 + erf(\sqrt{\frac{e\phi_{WQ}}{KT_p}})}$$

where $erf(x)$ is the error function and subindexes e, p and s refer to the thermalized electron population in the bulk of the plasma, the primary electrons and the emitted electrons respectively (we use the same subindex as for secondary electron due to similarity of the formulation). Additionally the following conditions are also applicable in the sheath edge:

- conservation of electron flux: $g_{reQ} = g_{rpQ} - g_{rsQ}$

- emitted charge current: $j_{rQ} = e(g_{riQ} - g_{reQ})$

- plasma quasi-neutrality: $n_{iQ} = n_{eQ} = n_{pQ} + n_{sQ}$

- charge saturation condition (ideal emitter): $U(e\phi_Q) = U(e\phi_W)$

- Bohm condition: $U(e\phi)''\big|_Q = U(e\phi)''\big|_W$

where $U(e\phi)$ is the so-called Sagdeev´s potential, a function that appears typically in sheath problems as a solution to Poisson´s equation. Because of the similarities with the ceramic wall sheath the form of this function is the same as in the problem presented in the previous section.

This closed set of equations can be solved in a non-dimensional form and yields results in terms of two main parameters, the ion Mach number and the non-dimensional potential sheath fall. Figure 3.8 presents the dimensionless sheath magnitudes for the active electrode. Both the non-dimensional current to the electrode sheath and the relationship between the emitted electron flux and net electron flux coming from the sheath are shown, for sonic and supersonic ion fluxes (see [2]). The higher the potential fall in the wall, the higher is the electric current. Notice that moderate sheath potential falls are enough to emit a significant electric current.
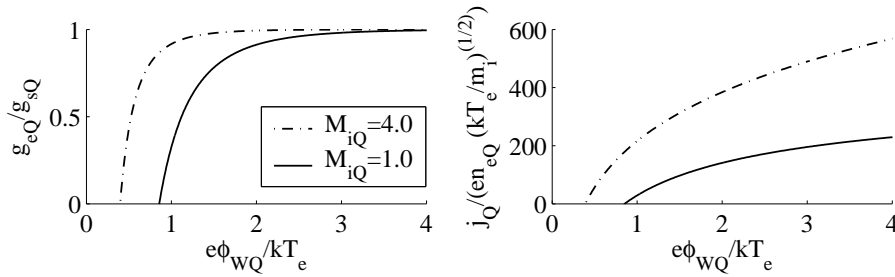
Figure 3.8: Net electron wall flux to electron emitted flux ratio (left) and non-dimensional wall current(right) as functions of the non-dimensional sheath potential fall for a high-emission electrode.

In chapter 6 this model is used to simulate an intermediate electrode inside a two-stage Hall thruster.

Chapter 4

IMPROVEMENTS IN PIC SUBCODE

This chapter explains the modifications implemented in the PIC sub-code of HPHall-2. Even though the basis of the method are mainly conserved, several improvements have been introduced in order to increase the accuracy of the numerical methods and thus of the simulation. Some of these changes are related to the so-called Bohm condition at the sheath edges, a topic that has received important attention lately since it affects greatly overall thruster performance predictions. Additionally, other topics such as multiple ionization have been reviewed and new and better algorithms have been implemented.

4.1   Independent doubly-charged ion population

As the discharge voltage increases, the electron temperature increases thus augmenting the multiple ionization fraction. The novelty reported here is to treat doubly-charged ions as an independent species from singly-charged ions. This allows to have reliable weighting magnitudes for these particles. The penalty is an increase of a 20% in overall computational time although, for a typical case, the total time remains within the order of an hour for a 2.4GHz PC.

A non-dimensional parameter that measures the relative importance of doubly-charged ions is the local ion charge number

$$Z_i \equiv \frac{n_e}{n_i} = \frac{n_{i+} + 2n_{i++}}{n_{i+} + n_{i++}}, \tag{4.1}$$

which usually takes values between 1 and 1.1. Figure 4.1 shows the effect of including double ionization for a SPT-100-like HET at nominal operation conditions(300V). Even for this moderate voltage the anode efficiency η_a increases a 5%, from 0.378 to 0.397, mainly due to a higher propellant utilization. Notice how the charge number increases with the temperature from the anode until the maximum T_e. Downstream of this point, the charge number value is due to ion convection. Additionally, the charge utilization is η_q =0.993. Hofer and Gallimore obtained experimentally, for the NASA-173Mv2 thruster and 300V, a lower value, η_q =0.986, which means larger multiple ionization. Thus, the need to consider multiply charged ions is justified even at moderate voltages.
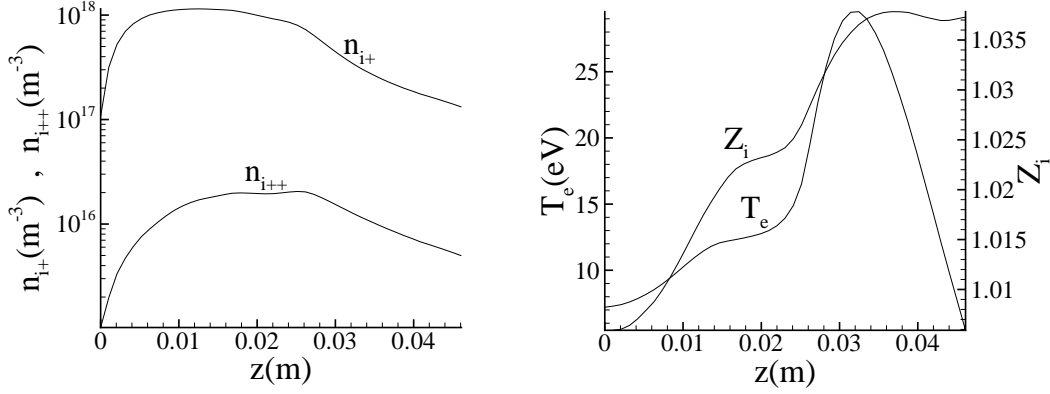
Figure 4.1: Singly- and doubly-charged ion densities along the channel, n_{i+} and n_{i++} respectively,(left figure) and electron temperature T_e and equivalent ion charge number Z_i along the channel (right figure). All variables are evaluated at the chamber median, r= 0.0425m.

4.2   Cell population control

4.2.1   Modified ionization algorithm

PIC methods obtain macroscopic variables (e.g. densities, particle fluxes) by weighting macropaticle magnitudes to the nodes of the computational domain. However, in order to avoid statistical oscillations, the number of macroparticles per cell must be high enough. A good trade-off between accuracy and computational cost is around 20 to 30 macroparticles per cell.

HPHall-2 fails to maintain an acceptable minimum number of macroparticles per cell, mainly near the anode where ionization is not strong enough and plasma density is small. This fact has important consequences since thruster efficiency depends on energy losses to walls that in turn depend on ion macroscopic variables, mainly density and particle flux to the walls. Thus, we decided to modify the ionization algorithm in order to control better the ion population. This algorithm is still of the MCC type and ensures a minimum number of particles.

The singly charged ion mass to be introduced into cell (j, k) at a given time step is computed from the PIC sub-code (see [3]) as:

$$(\Delta m_i)_{jk} \cong m_i \langle \dot{n}_i \rangle_{jk, t-\Delta t} \Delta V_{jk} \Delta t, \tag{4.2}$$

where ΔV_{jk} is the cell volume and

$$\langle \dot{n}_i \rangle_{jk} = \frac{(\dot{n}_i)_{jk} + (\dot{n}_i)_{j+1, k} + (\dot{n}_i)_{j, k+1} + (\dot{n}_i)_{j+1, k+1}}{4} \tag{4.3}$$

is the average ionization rate for cell (j, k).

MCC methods are based on performing a number $N_{prob, jk}$ of probability tests to determine the real number of macroions to be created, N_{jk}, in a particular cell and time step. The relationship between $N_{prob, jk}$ and $(\Delta m_i)_{jk}$ is given by:

$$M_{i, jk} N_{prob, jk} P_{jk} = (\Delta m_i)_{jk}, \tag{4.4}$$

where $M_{i,jk}$ is the mass of the created macroions and P_{jk} is a probability. Once $N_{prob,jk}$ is known the real number of macroions to be created in cell (j,k), N_{jk}, is determined comparing $N_{prob,jk}$ random numbers with P_{jk}. Notice that $N_{prob,jk}$ represents the maximum number of macroions that could be created in the cell in the time step considered.

Two of the three magnitudes of the left-hand-side of equation (4.4) can be chosen arbitrarily. HPHall and HPHall-2 take $P_{jk} = 0.30-0.85$ (depending on the ionization rate) and fix either the value of $M_{i,jk}$ or $N_{prob,jk}$ equal to one. In both cases, few particles are generated in low density regions. In order to control better the number of particles per cell, the ionization algorithm has been improved in the following way. First, a law for the probability P_{jk} is chosen; it can be constant (e.g., 0.5) or a function of the ionization rate as in the existing codes. Second, lower and upper limits of macroions per cell are defined, N_{min} and N_{max}. Then, three situations are considered, depending on the numbers of existing macroions in the cell $N_{i,jk}$:

1. If $N_{i,jk} < N_{min}$ then $N_{prob,jk}P_{jk} = N_{min} - N_{i,jk}$ (what ensures that the minimum of macroions is respected) and $M_{i,jk}$ is obtained from equation (4.4).

2. If $N_{min} < N_{i,jk} < N_{max}$ then $M_{i,jk}$ is chosen close to the average value of the mass of the macroions in the cell and the *integer* $N_{prob,jk}$ is computed from equation (4.4).

3. If $N_{i,jk} > N_{max}$ then $N_{prob,jk} = 1$ (what reduces the computational cost and ensures that there are no cells with too many particles) and $M_{i,jk}$ is obtained from equation (4.4).

4.2.2 Results

The main advantages of the new algorithm with respect to the previous one are:

1. it reduces statistical oscillations by ensuring a minimun number of particles in every cell.

2. the computational cost is reduced by controlling the maximum number of macroions per cell.

3. macroscopic variables are weighted properly near the walls since an acceptable number of macroions exists.

Figure (4.2) shows the differences between HPHall algorithms results and the results obtained with the algorithms proposed here. Clearly, the aforementioned advantages are achieved. The new algorithm is capable of limiting the ion population per cell between 20 and 50, approximately. In comparison, HPHall generated too many particles at the exit of the channel (~ 130), what increased the computational cost without improving simulation accuracy, whereas it worked with few particles (< 10) near the anode, what caused large temporal oscillations, in the scale Δt, of statistical character. Indeed, HPHall added an artificial background density of 10^{15} (part/m^3) to n_e to avoid 'near-singular' values. These minima are clearly observable in the plots of $n_e(t)$ for HPHall. The new population control algorithm solves excellently that issue. The statistical oscillations of $\phi(t)$ follow those of $n_e(t)$. Differences on the temporal evolution, in scales much larger than Δt are due to other improvements of the code [13, 14].
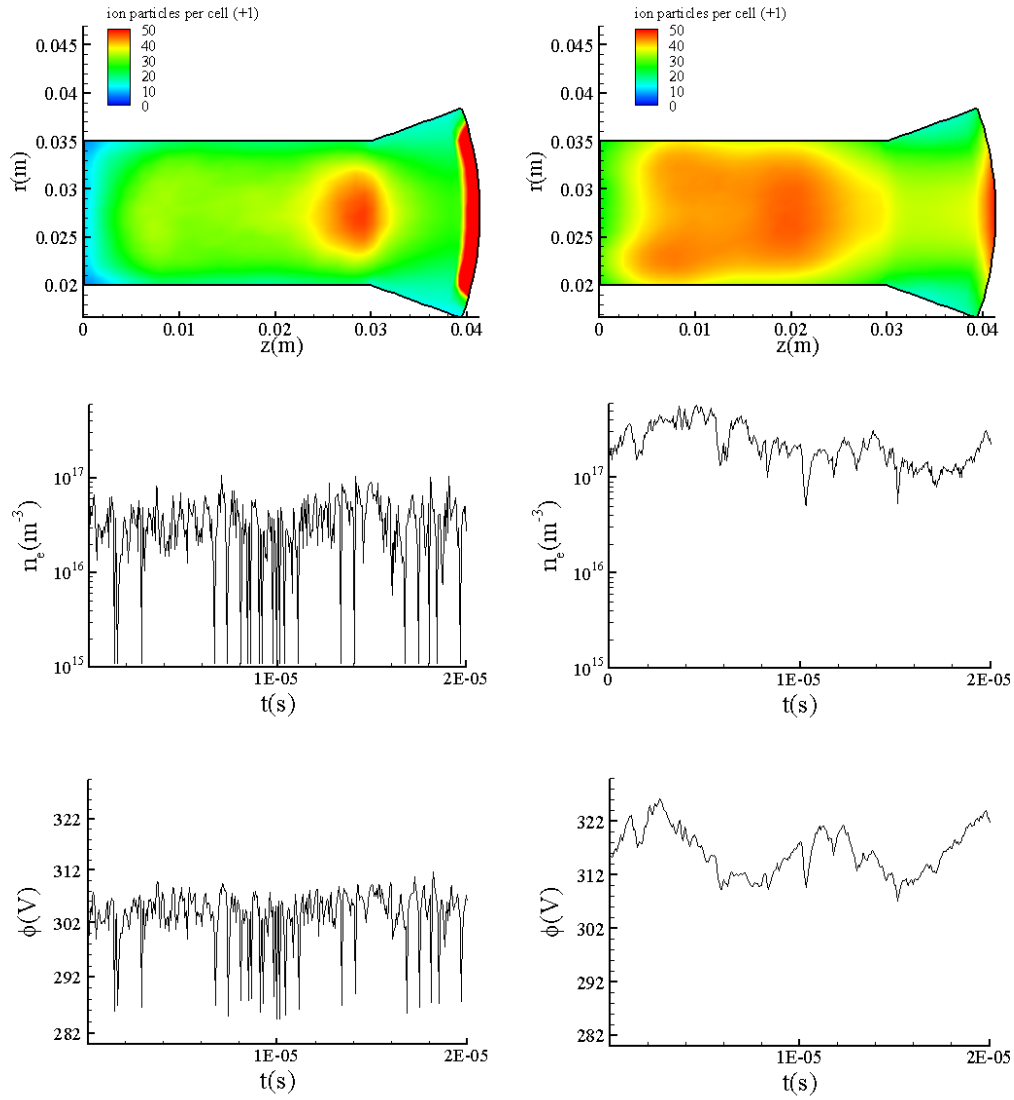
Figure 4.2: Comparison between HPHall-2 (left column) and the new hybrid simulation code (right column): Contour Number of macroions per cell, temporal evolution of plasma density and potential in a node of the anode sheath edge.

4.3 Bohm condition fulfilment: surface weighting

References [12] and [15] showed that a correct weighting of plasma magnitudes at the boundaries of the quasineutral computational domain was a delicate issue. In this section we review the methods that have been used in HPHall and HPHall-2 and we present a new scheme which compares advantageously with previous ones. The influence of the different schemes over the temporal oscillations is briefly discussed too.

Figure 4.3 shows the thruster geometry, the two test meshes and the magnetic field profile used in this section work. Parameters correspond to a SPT-70 thruster. To facilitate the understanding of wall effects, we use a rather simple geometry and a B-field satisfying $B_z = 0$ and $B_r \propto 1/r$; in this way $\nabla \cdot \mathbf{B} = 0$, but $\nabla \times \mathbf{B} \neq \mathbf{0}$.
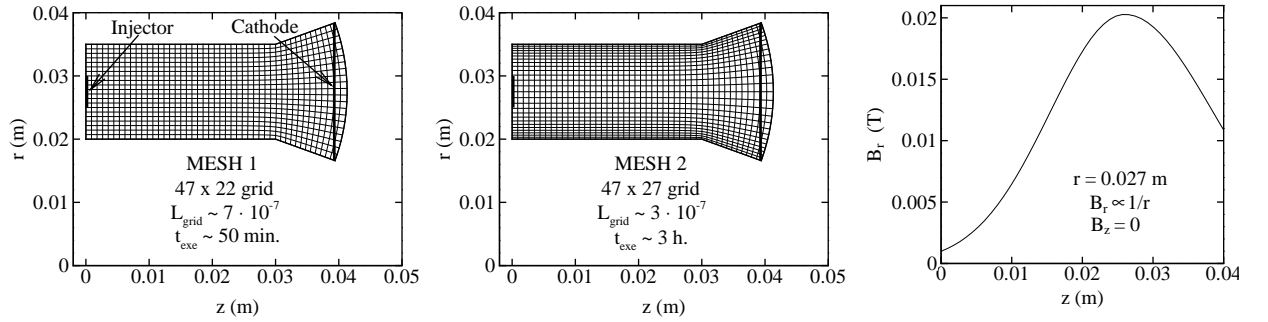
Figure 4.3: Geometry, test meshes and B-field for this work. Typical execution times (for a Pentium III at 2.4 GHz) to reach a steady-state response are included.

4.3.1 Weighting schemes

Volumetric Weighting(VW)

This is the original scheme used by Fife [16]. With this scheme, the magnitudes at nodes placed along the domain boundaries are computed using the typical PIC weighting algorithm. The ion density at a generic node T is determined from

$$(n_{eT})_{\mathrm{VW}} = \frac{1}{\Delta V_T} \sum_p \frac{Z_p m_p}{m_i} S_T(r_p, z_p), \tag{4.5}$$

where ΔV_T is the volume associated to node T, p refers to a particle being within the volume of influence of the node, m_p and (z_p, r_p) are particle mass and position, Z_p is one for single ions and two for double ions, and $S_T(r_p, z_p)$ is a bi-linear type weighting function for node T. This algorithm was applied to boundary nodes, even though the volume of influence at the boundaries is different (see Figure 6 of Ref. [15]). The one-side, asymmetric weighting at the boundary nodes tends to underestimate [overestimate] magnitudes that increase [decrease] toward the boundary. The error can be large for magnitudes that present large gradients near the sheath boundary (which include n_e, $\mathbf{v}_i$, and ϕ, but not $\mathbf{j}_i$).

In [12] we demonstrated that, using VW and as the cell size of the mesh is reduced, the ion flow at the boundary increases significantly and larger plasma gradients over the whole radial section develop. However, for the mesh sizes the ion flow remains well subsonic (i.e. still far from satisfying the Bohm condition), making it evident that a different numerical approach should be used in order to weight correctly magnitudes at the boundaries.

Corrected Volumetric Weighting(CW)

This scheme was proposed in Ref.[15]. The idea is to use the information of two nodes [the one in the boundary(T) and the internal one next to it(T+1)] in order to correct the $O(\Delta r)$ error induced by the asymmetric VW. With the information of two nodes, the error can be reduced to $O(\Delta r^2)$. The corrected plasma density is,

$$(n_{eT})_{\text{CW}} = \frac{3}{2}(n_{eT})_{\text{VW}} - \frac{1}{2}(n_{e,\,T+1})_{\text{VW}}, \tag{4.6}$$

with $(n_e)_{\text{VW}}$ the plasma density obtained from the VW. $(n_{eT})_{\text{CW}}$ is smaller than $(n_{eT})_{\text{VW}}$ for usual conditions. This correction lies on internal (i.e. PIC-computed) magnitudes only, but, at the same time, it depends on a second node, and thus errors depend on the cell size. Reference [15] proved the CW algorithm to give a reasonable fulfillment of the Bohm condition if the mesh is fine enough.

Bohm Condition Forcing (BCF)

This algorithm was presented in Ref.[15]. It consisted on forcing the ion flux to satisfy the (simple form of the) Bohm condition

$$\mathbf{j}_i \cdot \hat{\mathbf{N}} \geq n_e \sqrt{ZT_e/m_i} \tag{4.7}$$

whenever this was not achieved naturally by the VW algorithm; Z is the average ion charge-number. This the BCF algorithm for the density is

$$(n_{eT})_{BCF} = \min\left\{ \frac{(\mathbf{j}_{iT})_{\text{SW}} \cdot \hat{\mathbf{N}}}{e\sqrt{ZT_e/m_i}}, (n_{eT})_{\text{VW}} \right\} \tag{4.8}$$

With this algorithm, n_{eT} is lower in most points and instants than in the VW and, therefore, the electric field is larger near the boundaries. In Ref. [15] we showed that this algorithm provides excellent results even for relatively coarse meshes. This algorithm, contrary to the previous ones, relies on a property dictated by the space-charge sheath and, hence, extrinsic to the PIC code.

Surface Weighting (SW)

Although the CW algorithm was promising, the need of a fine mesh was evident. The idea of SW is to count the particles that cross the surface of influence of the node at the boundary. Thus, SW is a PIC-intrinsic algorithm but, at the same time, is independent of the cell size.

The density n_e in the boundary node T, as computed by SW, is

$$(n_{eT})_{\text{SW}} = \frac{1}{\Delta S_T \Delta t} \sum_p \frac{Z_p m_p}{m_i} \frac{1}{\mathbf{v}_p \cdot \hat{\mathbf{N}}}, \tag{4.9}$$

where the sum extends to all the ions that have crossed the boundary, $\hat{\mathbf{N}}$ is the normal to the wall, ΔS_T is the surface of influence of node T, and Δt is the timestep used by the PIC code.

This computation for n_{eT} can be used whenever the flow of particles is only in one direction, like in the boundary, where no ions are coming back. The obtained $(n_{eT})_{\mathrm{SW}}$ is a time average in Δt of n_{eT}, and its error is only $O(\Delta r^2)$ (associated to the discretization of the electric potential, mainly).

Similarly, the ion current density at the boundaries is given by

$$(\mathbf{j}_{iT})_{\mathrm{SW}} = \frac{e}{\Delta S_T \Delta t} \sum_p \frac{Z_p m_p}{m_i} \frac{\mathbf{v}_p}{\mathbf{v}_p \cdot \hat{\mathbf{N}}}. \tag{4.10}$$

4.3.2 Comparison of profiles for the different schemes

Figure 4.4 shows some radial profiles obtained with different algorithms and mesh sizes. The new SW is, like CW, intrinsic to the PIC model, but at the same time provides reasonably good results even for coarse meshes. The presheath potential drop for SW and mesh 1 is around 75% of the potential drop achieved with BCF, and the difference decreases to 5% just by dividing by two the mesh size around the walls. This large difference is mainly due to the steep slope that exists in the density and potential profiles near the boundaries of the quasineutral domain. Other magnitudes, like the ion density current flow to the walls $(\mathbf{j}_{iT})$ does not change as dramatically (see figure 4.5). The radial potential drop is not adequate to estimate the numerical errors induced by the hybrid model because it is very sensitive to the values near the boundaries, where the slope is extremely high. Magnitudes with flatter slopes are probably more suitable to analyze the accuracy of the schemes (as it is the case of $\mathbf{j}_{iT}$). However, radial profiles and their development give a good understanding of the problem, even if the exact values at the boundary are too sensitive to take them into account. Using $\mathbf{j}_{iT}$ as a criterium, we probably can say that BCF and SW are more accurate, since the change in ion flow with the mesh size is not as high as it is in CW.
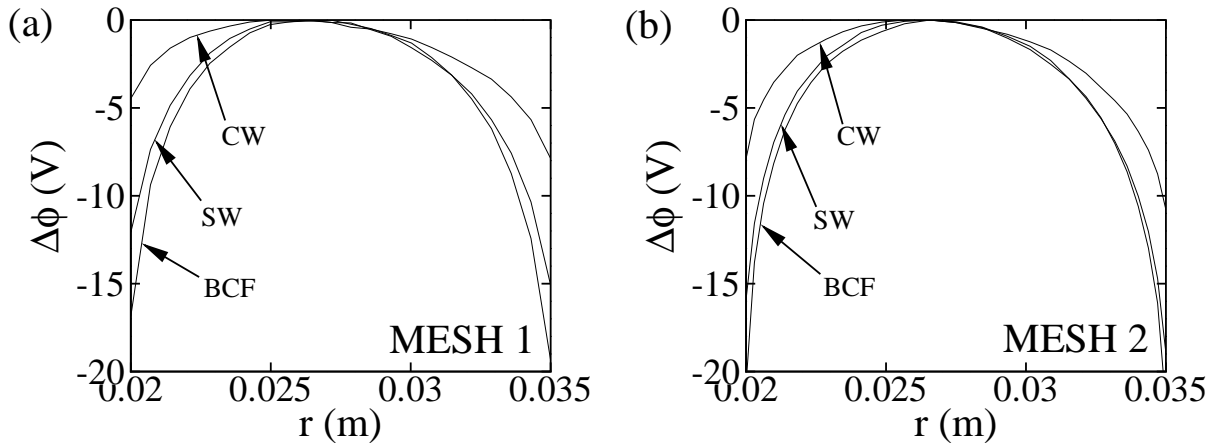
Figure 4.4: Radial profiles of electrostatic potential in $z = 0.0256$ m. (a) Comparison of results with the different algorithms in mesh 1. (b) Comparison of results with the different algorithms in mesh 2.

As observed in Ref. [12], the ion flow to the walls increases when the cell size decreases. Also, the schemes that provide more accuracy (BCF and SW) give a bigger ion flow to the walls. The ion flow can even be double with BCF and SW than it is with CW. Although BCF
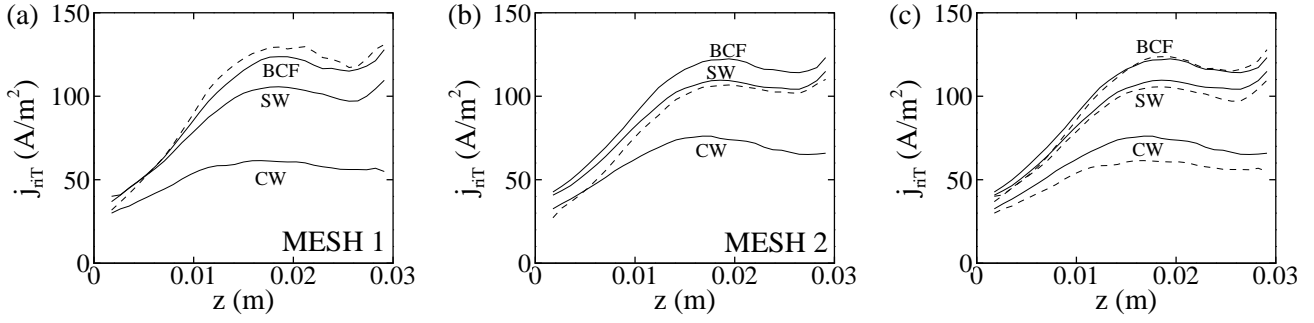
Figure 4.5: Axial profiles of ion current density to the inner wall for (a) mesh 1 and (b) mesh 2. In figures (a) and (b), the dashed line is the theoretical Bohm flux (j_{Bohm}) for SW and the corresponding mesh. (c) Comparison of sensitivities to the mesh size of CW, SW and BCF. Dashed lines represent results for mesh 1 and solid lines represent results for mesh 2.

and SW have similar accuracy - if we consider the sensitivity to mesh size a measure of the error -, there is a difference in the ion flow at the exit of the channel. This difference is small compared to the difference between those schemes and CW or VW, but it is still important and remains to be studied.

In figures 4.5(a) and 4.5(b) the resulting ion flow with SW is compared to the simple Bohm condition (4.8). With mesh 1, both results differ greatly, probably due to the very different values of n_e at the boundaries (we have already commented the sensitivity of boundary values). The comparison is much better for mesh 2, where both values are practically the same.

To sum up, surface Weighting and Bohm Condition Forcing yield the best results. The Corrected Weighting requires too fine of a mesh, although it can be good to confirm the results given by the two other methods. Between SW and BCF, SW has the advantage of being more self-consistent since it is PIC-intrinsic. If the error is estimated from the sensitivity of the current to the wall with respect to the mesh size, BCF and SW have similar performance. SW fits the Bohm condition (4.8) for reasonable mesh sizes, which confirms its accuracy.

4.3.3   Discharge oscillations

One of the uses of simulation codes is the study of plasma oscillations in Hall thrusters. Therefore, the effect of the different schemes on time oscillations is an important criterium to decide how appropriate the different schemes are. In figure 4.6, we present some time profiles for the discharge current. Two well-defined frequencies appear: one around 15 kHz, which seems to be related to the breathing mode, and another one near 170 kHz, which is, approximately, the ion transit frequency. These frequencies do not change with the mesh size or the weighting scheme, but their amplitude depends greatly on these parameters. The 15-kHz-oscillation amplitude is highly dependent on the weighting scheme: for mesh 2, the amplitude jumps from 35% for SW to 15% for BCF. It happens similarly for mesh 1. In the case of BCF, there must be two modes very near 15 kHz that produce, when they are added, the variable amplitude seen in figures 4.6(b) and 4.6(d) (it is especially clear in this last one). On the other hand, the 170 kHz oscillation is not as dependent on the weighting scheme. For mesh 2, its amplitude is 15% of the average current with both BCF and SW. For mesh 1, the amplitude decreases to 8% when we are using SW and is, again, around 15% with BCF. BCF seems to be able to reproduce

this mode correctly for coarse meshes, whereas with SW the amplitude of the high frequency oscillations is rather dependent on mesh size.

To sum up, BCF perturbs less the 170 kHz mode, but it provokes a variable amplitude for the breathing mode, perhaps due to the superposition of two modes of very similar frequency. SW is not as effective reproducing the high frequency oscillations as BCF is, but with fine enough mesh SW yields the same amplitude. There are still important differences in the breathing mode between both schemes, which remain to be studied.
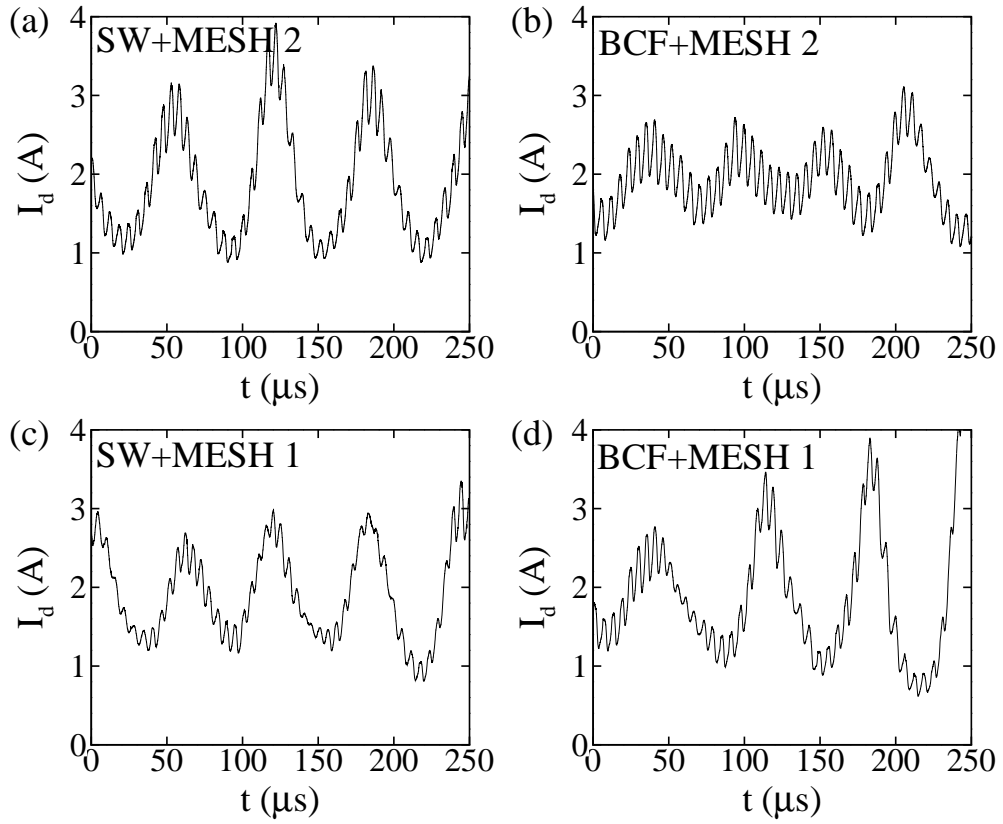
Figure 4.6: Time evolution of discharge current for different schemes and mesh sizes.

4.4   PIC subcode accuracy improvement

This work intends to correct certain inconsistencies found in both HPHall and its upgraded version HPHall-2 that mainly affect the PIC subcode. The problems are related to the 'leapfrog' integration scheme [17] and its connection with the weighting algorithms employed to transform macroparticle information into macroscopic variables such as densities, particle fluxes, energy fluxes, etcetera.

Macroparticle equations of motion are deduced from Newton´s law:

$$M_p \frac{d^2 \vec{x}_p}{dt^2} = \vec{F}(\vec{x}_p, \vec{v}_p, t) \equiv q_p \Big(\vec{E}(\vec{x}_p, t) + \vec{v}_p \times \vec{B}(\vec{x}_p) \Big) \tag{4.11}$$

where q_p, M_p, $\vec{x}_p$ and $\vec{v}_p$ are respectively macroparticle charge, mass, position and velocity and $\vec{E}$ and $\vec{B}$ are the electric and the magnetic fields respectively. Besides, another force term can be added accounting for both ion-neutral and charge-exchange collisions. The 'leapfrog' scheme permits to integrate numerically the equations of motion of all the macroparticles using the following algorithm:

$$\vec{v}_{p,t+\Delta t/2} = \vec{v}_{p,t-\Delta t/2} + \Delta t \cdot \vec{F}(\vec{x}_{p,t}, t) \tag{4.12}$$

$$\vec{x}_{p,t+\Delta t} = \vec{x}_{p,t} + \Delta t \cdot \vec{v}_{p,t+\Delta t/2} \tag{4.13}$$

where Δt is the PIC integration time step, $\vec{F}$ is the force on the macroparticle, and subindexes stand for the time step in which variables are computed. Notice that position and velocity are computed at instants that differ $\Delta t/2$, figure 4.7.
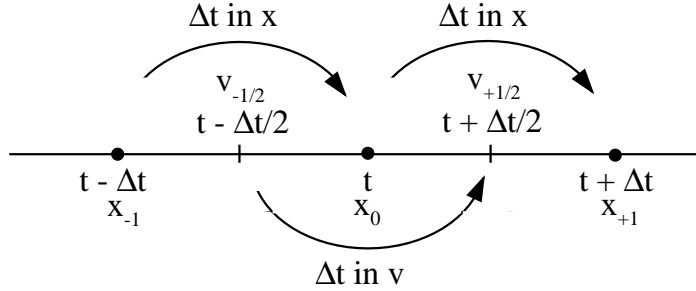
Figure 4.7: 'Leapfrog' integration scheme for macroparticle motion.

The numerical error associated to the 'leapfrog' scheme is O(Δt^2) in velocity and O(Δt^4) in position, *provided that* forces acting on macroparticles are known with O(Δt^2) accuracy. Therefore, the electric field, which is computed by the electron subcode, must have O(Δt^2) accuracy. In turn the electron sub-code needs, from the PIC sub-code, the electron density, n_e, and the ion current flux, $\vec{j}_i$. Thus, for the electric field to be known with O(Δt^2) accuracy, n_e and $\vec{j}_i$ must be computed with the same precision. Both HPHall and HPHall-2 fail to keep this level of accuracy. We explain next the corrections made to the different macroparticle algorithms in order to solve this precision problem.

4.4.1 Time-centered weighting of macroscopic variables

The ion density, n_i, and the ion current flux, $\vec{j}_i$, at a generic node (j, k), are obtained by the PIC sub-code from the weighting formulas[3]

$$(n_i)_{jk} = \frac{1}{m_i \Delta V_{\text{weight}, jk}} \sum_p M_p S_{jk}(\vec{x}_p), \tag{4.14}$$

$$(\vec{j}_i)_{jk} = \frac{e}{m_i \Delta V_{\text{weight}, jk}} \sum_p M_p \vec{v}_p S_{jk}(\vec{x}_p), \tag{4.15}$$

where $S_{jk}(\vec{x})$ is the (bi-linear) weighting function, $\Delta V_{\text{weight}, jk}$ is the volume of influence of the node[18], the summation extends to all macroions in the vicinity of the node (where $S_{jk} \neq 0$), M_p is the macroparticle mass (which varies as a result of ionization), and e and m_i are the charge and mass of the ion species. Similar weighting formulas apply for the pressure and higher-order variables.

In HPHall-2 the ionization process is modelled differently for the macroneutrals than for the much lighter (singly-charged) macroions: in each timestep, ionization leads to the loading of new macroions in the domain, but to a weak reduction of the mass of each macroneutral [16]. A similar process regulates the creation of doubly-charged macroions from macroneutrals or singly-charged macroions. Here, for simplicity, we consider that only one species of (singly-charged) ions is present, so that mass variation affects to macroneutrals only.

In HPHall-2, the macroscopic magnitudes are computed using position and mass at time t and velocity at time $t - \Delta t/2$, so their precision is only $O(\Delta t)$. In order to obtain all weighted variables at instant $t - \Delta t/2$ with precision $O(\Delta t^2)$, the position and mass of macroparticles at time $t - \Delta t/2$ must be used. The simple interpolation rules

$$\vec{x}_{p, t-\Delta t/2} = \frac{\vec{x}_{p, t} + \vec{x}_{p, t-\Delta t}}{2}, \tag{4.16}$$

$$M_{p, t-\Delta t/2} = \frac{M_{p, t} + M_{p, t-\Delta t}}{2}, \tag{4.17}$$

provide precision $O(\Delta t^2)$. Besides, the velocity obtained with the 'leapfrog' scheme has a numerical error of the same order. Therefore, the weighting process has the required $O(\Delta t^2)$ accuracy.

4.4.2 Time-centered loading of particles

At each timestep, HPHall-2 loads macroparticles into the simulation domain in order to account for different processes, such as neutral gas injection and ionization, particle wall recombination, etcetera. Care must be taken regarding the instant of loading. The MCC method of HPHall-2 provides an statistical distribution of the location and velocity of the loaded particles, but not on the instant of loading. Thus, the location and velocity are implicitly assigned to instants t and $t - \Delta t/2$, respectively. The enhancement proposed here is to determine randomly the instant of loading, that is $t - f\Delta t$, with $f \in [0, 1]$. Thus, the location and velocity provided by the MCC method correspond to that instant. It is then necessary to center the position and velocity of the loaded particles at times t and $t - \Delta t/2$, with errors $O(\Delta t^4)$ and $O(\Delta t^2)$, respectively, in

order to be consistent with the leapfrog scheme. The algorithm of Cartwright *et al.*[19] was adapted to HPHall in Ref. [20]. However, this complex procedure is not completely necessary since loaded particles are always macroneutrals (injection, wall accomodation or chamber flux modelling) and it is possible to assume constant mass and constant speed for the time step in which the particle is loaded. However, in order to be consistent with the leapfrog scheme position and velocity must be computed at t and $t-\Delta t/2$ respectively from position and velocity at the instant of injection.

4.4.3   Comments and results

The previous modifications have required several changes in the code since now it is necessary to distinguish two instants, $t-\Delta t/2$ and t. A second detail to take into account is that particles that are outside the computational domain at t cannot be removed from the computations until weighted magnitudes are computed at $t-\Delta t/2$. And inversely, injected particles can be inside the domain at t but outside at $t-\Delta t/2$ and thus, those particles must not be accounted for when weighting variables at $t-\Delta t/2$. This is particularly important in order to reproduce the desired mass flow through the injector.

However, there is a third improvement that is lacking in the current implementation. It is related to the computation of the exact instant in which a particle impacts the wall and the associated variables (mass, position and velocity).

The main consequence of these improvements is an increase of the PIC-subcode accuracy. This increase in time-accuracy of the code has some relevant effects on the simulation results regarding the mass conservation. The mass flow along the channel is conserved more accurately. Figure 4.8 depicts ion, neutral and total mass flow for an SPT-100 like simulated thruster (300 V, 4.8 mg/s) computed using both HPHall-2 and the modified algorithms. HPHall-2 presents a mass flow loss of 1.5% between the anode and the channel exit, while the error is below 0.4% with the new method. Note that the most important change takes place in the ion flow. This is likely due to proper account for the macroparticle position at $(t-\Delta t/2)$.
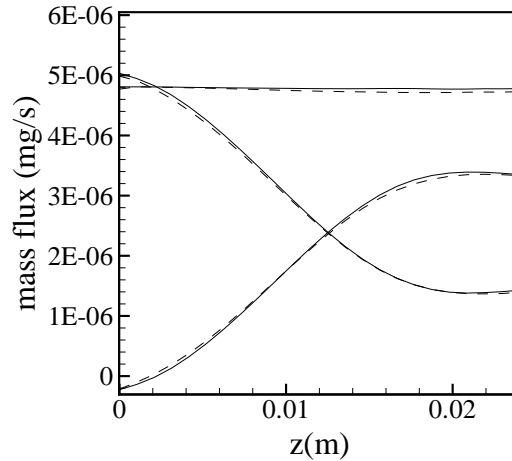
Figure 4.8: Mass flows in a SPT-100 like simulated Hall thruster computed by HPHall-2 (dashed lines) and the new algorithms (solid lines).

Notice that both results have been obtained running the program for more than 20000 iterations and therefore non-stationary effects are removed out when averaging discharge properties.

Chapter 5

NEW ELECTRON SUBCODE

This chapter is devoted to the electron subcode. The new electron differential formulation is explained in depth and the main advantages are highlighted. An additional section for the description of the near anode region is also included in order to explain the closure of the electron equations in this region of the thruster.

5.1 One-dimensional differential formulation

5.1.1 Magnetic-field-based reference frame

Electrons are highly magnetized inside Hall thrusters due to the strong magnetic field. Thus electron motions parallel and perpendicular to the magnetic field are completely different. This fact makes it convenient to describe electron physics in a magnetic-field-based reference frame. The induced magnetic field is negligible with respect to the externally applied magnetic field. Furthermore, the latter is assumed irrotational ($\nabla \times \vec{B} = \vec{0}$) and solenoidal ($\nabla \cdot \vec{B} = \vec{0}$) and therefore, potential ($\sigma(r, z)$) and stream ($\lambda(r, z)$) functions exist (see figure 1.1). These functions are defined by the following systems of equations:

$$\sigma: \quad \frac{\partial \sigma}{\partial r} = B_r, \quad \frac{\partial \sigma}{\partial z} = B_z, \qquad \lambda: \quad \frac{\partial \lambda}{\partial r} = -rB_z, \quad \frac{\partial \lambda}{\partial z} = rB_r. \qquad (5.1)$$

The resulting reference frame is defined by the coordinate set $(\sigma, \theta, \lambda)$ and the corresponding set of unit vectors $(\vec{u}_\parallel, \vec{u}_\theta, \vec{u}_\perp)$ where $\vec{u}_\theta$ is a unit vector along the azimuthal direction, $\vec{u}_\parallel = \vec{B}/B$, $\vec{u}_\perp = \vec{u}_\parallel \times \vec{u}_\theta$, $\vec{B}$ is the magnetic field vector and B is its modulus. The different vectors and coordinates are shown schematically in figure 5.1.

Additionally, it is useful to define spatial coordinates for arc lengths along the streamlines ($\lambda = $ const) and along the lateral walls ($r = r(z)$) called χ and s respectively:

$$\chi: \quad \frac{d\chi}{d\sigma}\bigg|_\lambda = \frac{1}{B}, \qquad s: \quad \frac{ds}{d\lambda}\bigg|_{r(z)} = \frac{1}{r(\vec{B} \cdot \vec{N})}, \qquad (5.2)$$

with $\vec{N}$ a vector perpendicular to the walls and oriented towards increasing radii, fig. 5.1 .
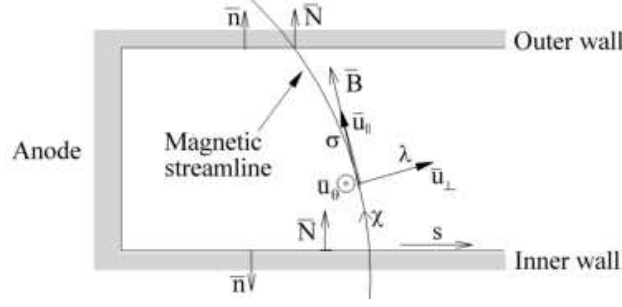
Figure 5.1: Magnetic-field-based reference frame.

5.1.2 Electron equations. General hypothesis.

Electron governing equations are charge, momentum and energy conservation. In the following subsections each one of them will be analyzed separately.

Charge conservation equation

Charge conservation law can be written as

$$\nabla \cdot \vec{j} = 0 \tag{5.3}$$

where $\vec{j} = \vec{j}_i + \vec{j}_e$ is the total charge current composed of the electron current, $\vec{j}_e = -en_e\vec{u}_e$, and the total ion current $\vec{j}_i = en_{i+}\vec{u}_{i+} + 2en_{i++}\vec{u}_{i++}$. Notice that $\vec{u}_j$ stands for the j-th species velocity vector.

Momentum conservation equation

Electron motion can be approximated as diffusive ($|\vec{u}_e| \ll \sqrt{T_e/m_e}$) because of the electromagnetic forces. Thus, inertial terms can be neglected in the momentum conservation law which yields the following simplified equation:

$$\vec{0} = -\nabla n_e T_e - en_e(\vec{E} + \vec{u}_e \times \vec{B}) - n_e m_e \nu_e \vec{u}_e, \tag{5.4}$$

where m_e and T_e are the electron mass and temperature, respectively, $\vec{E}$ is the electric field vector ($\vec{E} = -\nabla\phi$), ϕ is the electric potential and $\nu_e = \nu_{en} + \nu_{wm} + \nu_{ano}$ is the total electron collision frequency. Notice that electron-neutral collisions (ν_{en}) dominate with respect to other types of binary collisions[21], but two extra terms are added in order to account for near-wall conductivity (ν_{wm}) and anomalous diffusion (ν_{ano}). A detailed model of these terms will be given later.

The collision term is negligible with respect to the other terms along the streamlines and, thus, projecting equation (5.4) onto ($\vec{u}_\parallel$) yields:

$$0 = -\frac{\partial}{\partial\sigma}(n_e T_e) + en_e\frac{\partial\phi}{\partial\sigma} \tag{5.5}$$

The temperature is approximately constant along the streamlines (as we will justify later), and therefore, equation (5.5) can be integrated to yield the Maxwell-Boltzmann equilibrium relationship:

$$e\phi(\sigma, \lambda, t) = T_e(\lambda, t) \ln \frac{n_e(\sigma, \lambda, t)}{n_e^\star(\lambda, t)} + e\phi^\star(\lambda, t) \tag{5.6}$$

where $\phi^\star$ is the so-called thermalized potential, whose definition depends on the chosen reference density $n_e^\star$, that can be defined as a constant or as an average density along each streamline.

The projection of equation (5.4) onto the azimutal and perpendicular $(\vec{u}_\perp)$ directions yields:

$$0 = -en_e u_{\perp e} B - n_e m_e \nu_e u_{\theta e} \ , \tag{5.7}$$

$$0 = -rB\frac{\partial}{\partial\lambda}(n_e T_e) + en_e rB\frac{\partial\phi}{\partial\lambda} + en_e u_{\theta e} B - n_e m_e \nu_e u_{\perp e} \ . \tag{5.8}$$

The Hall parameter is defined as the ratio between the electron gyro-frequency and the electron collisional frequency, $\beta = \omega_e/\nu_e = (eB)/(m_e\nu_e)$, and its value is higher than 100 for typical Hall thruster conditions ($\beta \gg 1$). If expressions (5.7) and (5.8) are combined with the Maxwell-Boltzmann equilibrium relationship and the Hall parameter definition, the following expressions can be derived for the electron velocities $u_{\perp e}$ and $u_{\theta e}$:

$$u_{\theta e} = -\beta u_{\perp e} \ , \qquad u_{\perp e} = \frac{r\beta}{1+\beta^2}\left(\frac{\partial\phi}{\partial\lambda} - \frac{1}{en_e}\frac{\partial}{\partial\lambda}(n_e T_e)\right) \ . \tag{5.9}$$

Equations (5.9) show respectively the closed-drift described by electrons and a generalized Ohm's law relating the electron velocity with the electric field and the pressure gradient.

Energy conservation equation

Energy conservation can be expressed in the diffusive limit as:

$$\frac{\partial}{\partial t}\left(\frac{3}{2}n_e T_e\right) + \nabla \cdot \left(\frac{5}{2}n_e T_e \vec{u}_e + \vec{q}_e\right) = \vec{j}_e \cdot \vec{E} - \dot{n}_e \alpha_i(T_e) E_i \ , \tag{5.10}$$

where $\vec{q}_e$ is the heat conduction flux, $\vec{j}_e \cdot \vec{E}$ is the Joule heating and $\dot{n}_e \alpha_i(T_e) E_i$ are energy losses due to ionization. Here, $\dot{n}_e$ is the ionization rate, $\alpha_i(T_e)$ is the non-dimensional net energy loss per electron and E_i is the Xenon first ionization energy. Notice that elastic collision energy losses are negligible with respect to ionization losses[16].

The ionization rate ($\dot{n}_e$) can be computed as a combination of the different ionization processes:

$$\dot{n}_e = \dot{n}_{i+}^{X_e \to X_{e+}} + \dot{n}_{i++}^{X_{e+} \to X_{e++}} + 2\dot{n}_{i++}^{X_e \to X_{e++}} = n_e n_n(\zeta_{X_e \to X_{e+}} + 2\zeta_{X_e \to X_{e++}}) + n_e n_{i+}\zeta_{X_{e+} \to X_{e++}} \tag{5.11}$$

where n_n is the neutral density and variables ζ_j depend on the electron temperature[16]. These functions are plotted in figure 5.2(a) for each one of the different processes. Notice that multiple ionization is not negligible for moderate-to-high temperatures what makes it necessary to account for doubly-charged ions in Hall thrusters. Dugan's model for the ionization cost factor $\alpha_i(T_e)$, fig. 5.2(b), is used.
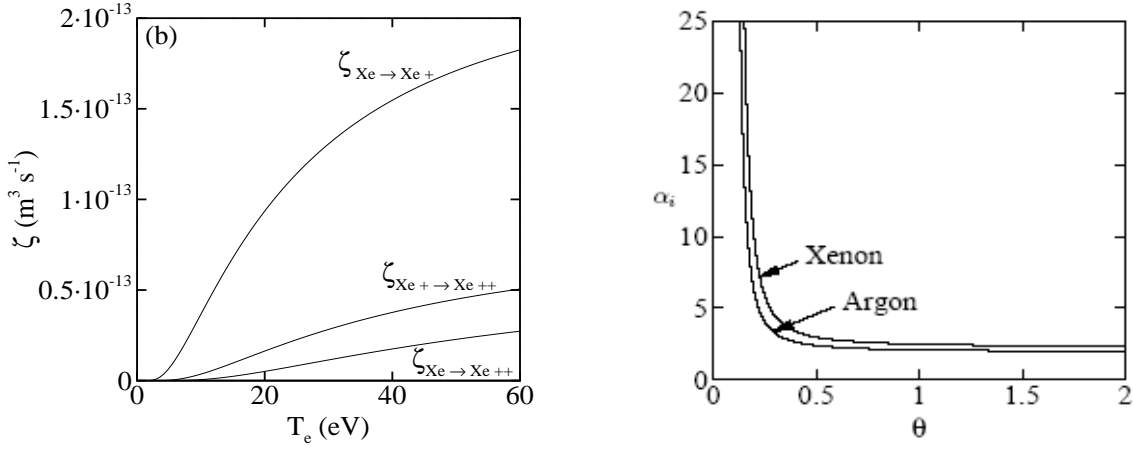
Figure 5.2: (a) Comparison of ionization rate parameters $\zeta_j(T_e)$ for Xenon different ionization processes. (b) Normalized electron production cost α_i versus normalized temperature $\theta = T_e/E_i$.

The appropriate diffusive model for heat conduction according to reference [22] is:

$$(5/2)n_e T_e \nabla T_e + e\vec{q}_e \times \vec{B} + m_e \nu_e \vec{q}_e = \vec{0}$$

Projecting it onto the magnetic reference frame yields:

$$q_{\|e} = -\frac{5}{2}\frac{n_e T_e \beta}{e}\frac{\partial T_e}{\partial \sigma} \,, \qquad q_{\perp e} = -\frac{5}{2}\frac{n_e r T_e}{e}\frac{\beta}{1+\beta^2}\frac{\partial T_e}{\partial \lambda} \,. \qquad (5.12)$$

The estimate of the relative order of magnitude of the derivatives of T_e yields

$$r\frac{\partial T_e/\partial \sigma}{\partial T_e/\partial \lambda} \sim \beta^2 \frac{q_{\perp e}}{q_{\|e}} \sim 10^4 \frac{q_{\perp e}}{q_{\|e}}.$$

Therefore, for any plausible ratio between heat conduction components, the variation of the electron temperature along the streamlines seems negligible, justifying the approximation of isothermal streamlines, i.e. $T_e = T_e(\lambda, t)$.

5.1.3   Evolution equations across streamlines

Let us consider a general conservation law of the form, $\nabla \cdot \vec{u} = f$, for certain functions $\vec{u}$ and f. The integration of this expression between two different streamsurfaces located at λ and $\lambda + d\lambda$, being $d\lambda$ an infinitesimal quantity, yields

$$\int_{\Gamma(\lambda)} 2\pi \frac{f}{B}\, d\chi = \frac{\partial}{\partial \lambda}\left(\int_{\Gamma(\lambda)} 2\pi r(\vec{u}\cdot\vec{u}_\perp)d\chi\right) + \sum_{i=1,2}\left.\frac{2\pi(\vec{u}\cdot\vec{n})}{(\vec{B}\cdot\vec{N})}\right|_i , \qquad (5.13)$$

where the summation is extended to the inner ($i = 1$) and the outer ($i = 2$) walls, $\vec{n}$ points out of the wall, fig. 5.1, and $\Gamma(\lambda)$ stands for the streamline located at λ.

The electron subcode of HPHall-2 was designed for ceramic walls only and thus considered that the discharge current was constant along the channel. This simplified enormously the electron continuity equation. The present code eliminates that constraint by accepting net exchanges of electric current at the lateral walls. The previous integration procedure is applied to the charge equation (5.3) in order to obtain a general charge conservation equation for the electron current across the streamlines:

$$\frac{\partial I_e}{\partial \lambda} = -\frac{\partial I_i}{\partial \lambda} - 2\pi \sum_{i=1,2} \frac{\vec{j} \cdot \vec{n}}{\vec{B} \cdot \vec{N}}\bigg|_i, \qquad I_{i,e}(\lambda) = \iint_{S(\lambda)} (\vec{j}_{i,e} \cdot \vec{u}_\perp) \, dS. \tag{5.14}$$

Here $\vec{j} \cdot \vec{n}$ is the electric current density to the lateral (sheaths and) walls, and the ion current density $\vec{j}_i$ is computed by the particle sub-code. This charge conservation equation is one of the main novelties of the present model. SPT-type thrusters normally have ceramic walls and therefore no net charge flux to lateral walls exists $(\vec{j} \cdot \vec{n} = 0)$. However, some new designs incorporate intermediate segmented electrodes[23] in the lateral walls in order to enhance performances and control. This new formulation permits to simulate these configurations. Additionally, a more physically meaningful cathode modelling is possible with this formulation as it is shown in reference [13].

Applying Eq. (5.13), the energy equation (5.10) is transformed into:

$$\frac{\partial}{\partial t}(aT_e) + \frac{\partial}{\partial \lambda}\big(b(T_e)T_e\big) = \frac{\partial}{\partial \lambda}\Big(c(T_e)T_e\frac{\partial T_e}{\partial \lambda}\Big) + Q(T_e) \,, \tag{5.15}$$

where coefficients a, $b(T_e)$, $c(T_e)$ and $Q(T_e)$ are defined as

$$a = \frac{3}{2}\left(\int_{\Gamma(\lambda)} \frac{2\pi e}{B}\, n_e\, d\chi\right),$$

$$b(T_e) = -\frac{5}{2}I_e + \Big(\frac{T_e}{n_e^\star}\frac{\partial n_e^\star}{\partial \lambda} - e\frac{\partial \phi^\star}{\partial \lambda}\Big)\Big(\int_{\Gamma(\lambda)} \frac{2\pi n_e r^2}{\beta(T_e)}\, \ln\frac{n_e}{n_e^\star}\, d\chi\Big),$$

$$c(T_e) = \int_{\Gamma(\lambda)} \frac{2\pi n_e r^2}{\beta(T_e)}\Big(\frac{5}{2} - \big(1 - \ln\frac{n_e}{n_e^\star}\big)\ln\frac{n_e}{n_e^\star}\Big) d\chi \,,$$

$$Q(T_e) = -I_e e\frac{\partial \phi^\star}{\partial \lambda} - \Big(\int_{\Gamma(\lambda)} \frac{2\pi e}{B}\, \dot{n}_e \alpha_i E_i\, d\chi\Big) + T_e\Big(\int_{\Gamma(\lambda)} \frac{2\pi e}{B}\big(\frac{\partial n_e}{\partial t} - \dot{n}_e\big)\, \ln\frac{n_e}{n_e^\star}\, d\chi\Big) +$$

$$-\sum_{i=1,2} \frac{2\pi \vec{n}}{\vec{B} \cdot \vec{N}} \cdot \Big(e\vec{q}_e^{\,tot} - \vec{j}_e T_e \ln\frac{n_e}{n_e^\star}\Big)\bigg|_i.$$

Coefficients $b(T_e)$ and $c(T_e)$ depend weakly on temperature through the Hall parameter $\beta = \omega_e/\nu_e(T_e)$. Coefficient $Q(T_e)$ is the energy source term and accounts for (from left to right in its definition) cross-field Joule heating, ionization losses, terms related to density variations along the streamlines, and energy fluxes to the sheaths. These exchanges with the sheaths are obtained from the wall interaction subcode.

Finally, the integration of equation (5.9) along the streamsurfaces yields a (linear) relation between $I_e(\lambda)$ and the derivatives of $T_e(\lambda)$ and $\phi^*(\lambda)$,

$$\left(\int_{\Gamma(\lambda)} \frac{2\pi n_e r^2}{\beta} \, d\chi \right) \left(e \frac{\partial \phi^\star}{\partial \lambda} - \frac{T_e}{n_e^\star} \frac{\partial n_e^\star}{\partial \lambda} \right) = \left(\int_{\Gamma(\lambda)} \frac{2\pi n_e r^2}{\beta} \left(1 - \ln \frac{n_e}{n_e^\star} \right) d\chi \right) \frac{\partial T_e}{\partial \lambda} - I_e \, . \tag{5.16}$$

Equations (5.14)-(5.16) form a system of coupled differential equations in λ for $T_e(\lambda, t)$, $\phi^\star(\lambda, t)$ and $I_e(\lambda, t)$. These equations depend only on one spatial variable, λ, thanks to the assumptions of constant electron temperature and Boltzmann equilibrium along magnetic field lines. The advantages of a differential formulation, compared to the integral one, is that it gives more flexibility on the choice of the most convenient numerical integration algorithm. Also, in the new code, we are trying to make the magnetic mesh fully independent from the PIC-mesh. In this manner, refinement can be achieved in the electron subcode without increasing the number of cells of the PIC-mesh. Besides, non-uniform electron meshes can be used to better model electron physics. Finally, the new formulation has allowed to account for the work of the electric field parallel to magnetic field lines, neglected in HPHall-2.

To sum up, the main assumptions and features of the macroscopic electron model are the following:

1. T_e is constant along the magnetic streamlines, so that $T_e = T_e(\lambda)$ with λ defining the streamline.

2. A generalized Maxwell-Boltzmann equilibrium applies for the electric potential:

$$e\phi(\lambda, \sigma) = e\phi^\star(\lambda) + T_e(\lambda) \ln \frac{n_e(\lambda, \sigma)}{n_e^\star} \tag{5.17}$$

   where σ is the spatial variable along a streamline, $\phi^\star(\lambda)$ is the 'thermalized' potential, $n^\star$ is a reference value, and $n_e(\lambda, \sigma)$ is provided by the particle sub-code.

3. The generalized Ohm's law relates linearly the derivatives of $T_e(\lambda)$ and $\phi^\star(\lambda)$, with the electron current $I_e(\lambda)$.

4. The electron current, $I_e(\lambda)$, is computed from a current conservation ordinary equation, which admits current sources from the walls:

$$\frac{\partial}{\partial \lambda}(I_e + I_i) = -2\pi \sum_{i=1,2} \frac{\vec{j} \cdot \vec{n}}{\vec{B} \cdot \vec{N}} \bigg|_i, \tag{5.18}$$

   where $I_i(\lambda)$ is the ion current function, provided by the particle sub-code, $\vec{j} \equiv \vec{j_i} + \vec{j_e}$ is the electric current density at the inner(1) or outer(2) walls, $\vec{n}$ is the unit vector pointing outwards of the domain and $\vec{N}$ is defined in Fig. 5.1.

5. The temperature profile $T_e(\lambda)$ is obtained from a parabolic heat equation on variables λ and time t. This equation includes $I_e(\lambda)$ and heat sources $\vec{q}_{eQ}^{tot}(\lambda)$ from the lateral contour of the domain (i.e. lateral thruster walls mainly).

5.1.4 Cross-field electron transport

Classical theory predicts an electron cross-field transport much smaller than the one measured experimentally in HET. Two physical mechanisms have been proposed to explain this high electron mobility: anomalous diffusion due to correlated azimuthal fluctuations of plasma density and electric field[24], and near wall conductivity due to secondary electron emission from ceramic walls[21, 25, 26]. These two mechanisms can be incorporated as additional electron cross-field transport through effective collision frequencies. Thus, the different terms in $\nu_e = \nu_{en} + \nu_{wm} + \nu_{ano}$ are modelled as follows[3, 27]:

$$\nu_{en} = n_n \sigma_{en} \sqrt{\frac{8T_e}{\pi m_e}}, \qquad \nu_{ano} = \alpha_{ano}\omega_e, \qquad \nu_{wm} = \frac{\sum_{i=1,2} \left. \frac{2\pi \vec{n} \cdot \vec{j}_e}{e\vec{B} \cdot \vec{N}} \right|_i}{\int_{\Gamma(\lambda)} \frac{2\pi n_e}{B} \, d\chi}, \qquad (5.19)$$

with $\sigma_{en} = 3 \cdot 10^{-19} m^2$ and $\alpha_{ano} \sim 10^{-2} - 10^{-1}$, a fitting parameter to match experiments and simulation results.

5.1.5 Boundary conditions and numerical method

In order to integrate electron equations proper boundary conditions must be imposed for the electron temperature, the thermalized potential and the discharge current. Electron temperature is assumed to be known at the cathode streamline (5 eV) while a zero heat conduction assumption is adopted for the anode. On the other hand, the discharge voltage is fixed between the anode and the cathode, and consequently, a shooting method is employed to verify this condition with the anode potential as a parameter. Clearly, the anode sheath presented in a previous chapter must be accounted for in these computations[2].

   The numerical method we employ is described next. Electron equations are discretized spatially with first-order finite differences while a explicit Euler scheme is used for the temporal discretization (i.e., forward in time and centered in space, FTCS). Figure (1.1) shows schematically the magnetic mesh used for electron equations as well as the corresponding magnetic field.

   PIC sub-code employs a time-step Δt such that most particles do not advance more than half a cell per time-step. However, electron equations must be integrated with a smaller time-step δt due to numerical stability constraints and therefore these equations must be solved several times per particle time-step. In fact, the ratio $\Delta t/\delta t$, which was about 1.000 in HPHall-2, has been reduced to about 100 with the new formulation. This change has more than offset some increases in computational cost that both the new electron formulation and the modifications in the PIC-subcode have introduced. So, this time step increase, together with other improvements, causes a 20% reduction in computational time and permits to simulate 1ms of thruster operation in less than 2 hours with a 2.5GHz PC computer.

5.2   Accuracy improvement

One of the advantages of the present formulation is related to numerical accuracy. In order to evaluate the numerical error it is useful to exploit the electron energy balance that can be expressed as:

$$P_{elec,e} + P_{cathode} = P_{ioniz} + P_{lateral,e} + P_{anode,e},$$

where $P_{elec,e}$ is the overall Joule heating, $P_{cathode}$ is the amount of energy introduced through cathode in the form of an electron current, P_{ioniz} represents losses due to ionization and excitation, and $P_{lateral,e}$ and $P_{anode,e}$ represent energy losses into lateral and anode sheaths respectively. This equation is derived by integrating in λ the electron energy conservation law (5.10).

Table 5.1 shows the electron energy balance of a simulation of a SPT-100 like thruster. The balance is almost perfect with an error of around 1% of the total electron power.

$P_{elec,e}$	$P_{cathode}$	P_{ioniz}	$P_{lateral,e}$	$P_{anode,e}$	$Error$
542.4 W	12.8 W	143.4 W	326.5 W	79.6 W	5.7 W

Table 5.1: Electron energy balance for an SPT-100 like thruster

It is possible to estimate the numerical error at every electron time step based on electron energy conservation and accounting for the temporal term of the energy equation. The evolution of the estimated numerical error is shown in figure 5.3. As can be seen it almost always remains below 0.5 W. Thus, those 6W of error in the stationary energy conservation check are mainly due to the temporal term. In any case, it is around 1% what is comparable to other errors already mentioned in this report.

Figure 5.3: Time evolution of the estimated numerical error associated to the electron energy equation

5.3   Near-anode region

The simulated spatial domain goes from the external plume to the anode. However the anode surface A (and thus the anode sheath edge B) is not a magnetic streamline; see figure 5.4. Let S: $\lambda = \lambda_S$ be the magnetic streamline separating those streamlines intersecting the anode from those without intersection. The electron model is not well designed to treat the near-anode region between S and the anode sheath edge B. We present here an approximate treatment for this region, which improves clearly previous algorithms used by HPHall-2.

For sake of simplicity, here we consider the anode (more precisely, the anode sheath edge) as a $z = const$ surface. The new algorithm consists on the following. First and in order to close the spatial domain of the heat equation, we consider the anode as a magnetic streamline. The virtual streamline value λ_* assigned to the anode is the average value of $\lambda(r)$ along the anode. Second, the heat and Ohm's equations are solved, thus yielding $T_e(\lambda_*)$ and $\phi_0(\lambda_*)$. Third, these values are not assigned to the anode sheath edge, but to the actual streamline $\lambda = \lambda_*$, which lies between B and S. Four, a linear interpolation based on values at λ_S and λ_* determines $T_e(\lambda)$ and $\phi_0(\lambda)$ in the whole BS region. Finally, Eq.(5.17) yields the potential $\phi(\lambda, \sigma)$, wherefrom the potential distribution at the sheath edge, $\phi_B(r)$, is obtained.

The new algorithm includes improvements in the model for the anode sheath and the iteration procedure to determine the current-voltage response, $I_d(V_d)$. Let $\phi_B(r)$, $T_{eB}(r)$, and $n_{eB}(r)$ be the plasma variables at the sheath edge, obtained from the integration of the electron equations. If we take $\phi = 0$ at the cathode point, the potential at the anode would coincide with the discharge voltage $\phi_A(r) = V_d$.

Figure 5.4: Scheme for the treatment of the near-anode region.

The model of the anode sheath, presented in chapter 3 yields a relation between the potential fall ϕ_{AB} (at a given location r) and the electron current j_{zeB} incident onto the sheath,

$$\frac{e\phi_{AB}}{T_{eB}} = f\left(\frac{j_{ezB}}{en_{eB}\sqrt{T_{eB}/m_i}}\right). \tag{5.20}$$

The algorithm we propose considers the anode potential, ϕ_A, as a known parameter and thus the anode potential fall profile $\phi_{AB}(r) = \phi_B(r) - \phi_A$ is known. This algorithm uses the sheath current-voltage curve to determine the anode electron density current,

$$j_{zeB}(r) = en_{eB}(r)\sqrt{\frac{T_{eB}(r)}{m_i}}f^{-1}\left(\frac{e\phi_{AB}(r)}{T_{eB}(r)}\right). \tag{5.21}$$

Then, in order to satisfy the anode sheath conditions, the discharge current through the external circuit should be

$$I_d = \int_{r_1}^{r_2} 2\pi dr[j_{ziB}(r) + j_{zeB}(r)], \tag{5.22}$$

where the ion current through the anode, $j_{ziB}(r)$, is provided by the particle code. This current I_d should coincide with the current injected into the discharge through the cathode (or the multiple cathodes, for multi-stage operation). This condition is used to compute the anode potential ϕ_A. In turn, this value should coincide with the discharge voltage V_d. If not, electron equations must be reintegrated until convergence is achieved; 2-3 iterations normally are enough.
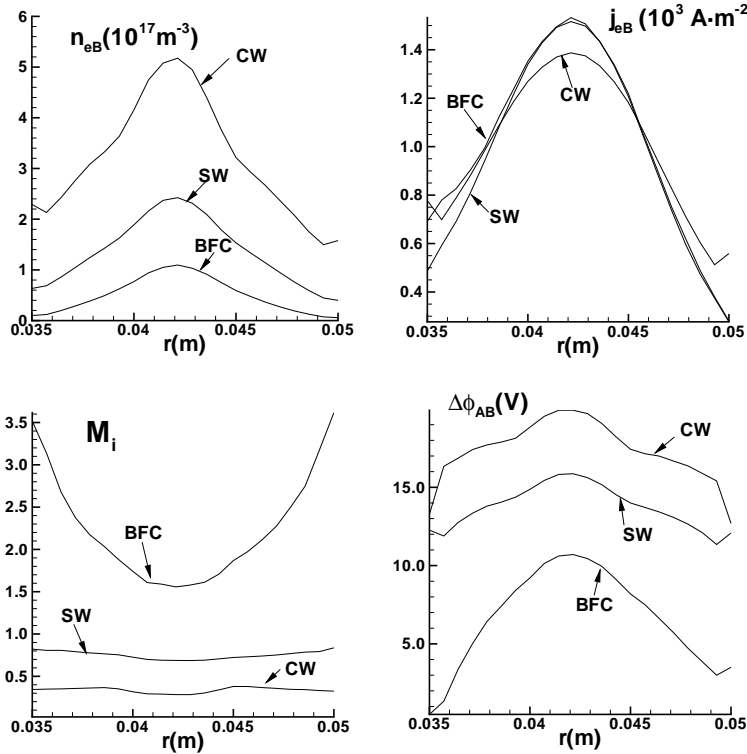
Figure 5.5: Radial profiles of plasma magnitudes at the anode sheath. CW, SW, and BFC mean corrected weighting, surface weighting, and Bohm forcing condition. M_i is the ion Mach number at the sheath edge. M_i and n_e are computed by the particle code. ϕ_{AB} is obtained from the anode sheath model of Ref. [2]. The anode potential is 300V. $j_{eB} = -\vec{j}_e \cdot \vec{n}$

At present, the anode sheath model is valid only for negative or electron-repelling sheaths. It could happen that $\phi_{AB}(r) < 0$ at certain zones on the anode. Provisionally, for these zones, we are taking from Eq.(5.20) the value of j_{zeB} for $\phi_{AB} = 0$.

In Fig. 5.5, CW, SW, and BCF indicate the weighting algorithms used by the particle code to weight magnitudes at the contour nodes [2]. The Surface Weighting algorithm seems the best and more consistent option. The correct value of ion Mach number should be a bit above one. The decay of plasma density and potential fall towards the lateral wall is consistent with the gas injector being at the center of the anode. Figure 5.6 shows 2D maps of the near anode region for the main plasma variables. The total chamber length is 25 mm. The separatrix intersects the inner and outer walls at 6 mm approximately. For this case, the ion backstreaming region extends only ~ 3 mm. The line of zero ion flux coincides approximately with the position of the point of maximum potential, $\sim 319V$. The large radial gradients of ϕ for BCF in Fig. 5.6 are a consequence of the high Mach numbers obtained with BCF, which leads to excessively low plasma densities at the lateral walls. The regular variation of the 2D profiles in the near-anode region can be presented as a proof of the suitability the algorithms presented here.[1]
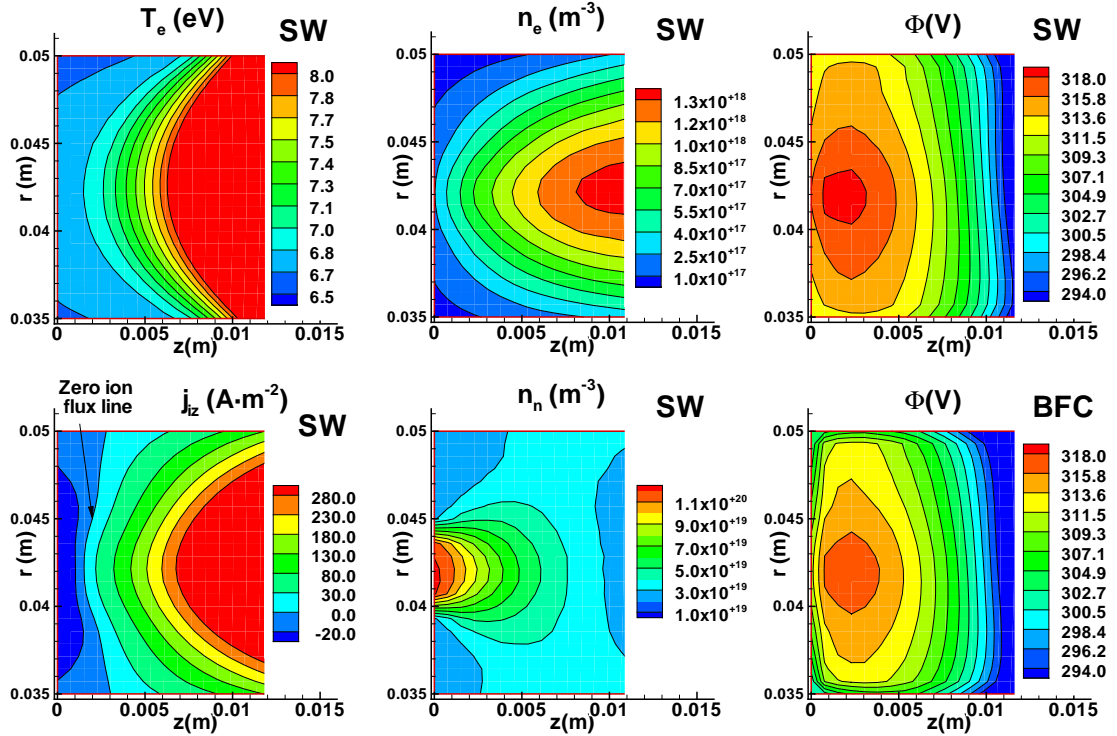
Figure 5.6: 2D maps of plasma variables in the near anode region. The left contour corresponds to the sheath edge B. Sheaths cannot be not shown in this (quasineutral) scale.

---

[1]One interesting observation is worth here. The particle sub-code assumes that all ions arriving to a sheath edge are collected by the wall. This is correct for negative sheaths. In regions with positive sheaths, part of the ions reaching them are reflected back to the quasineutral region. Positive sheaths remain to be implemented in the code. It should not be difficult to implement in the PIC subcode the reflection of ions in positive sheaths. The main problem lies on the electron model. As we prove in Annex A, for positive sheaths (and even for small negative sheaths) inertial effects on electrons become important and the present electron formulation is unable to include them. In any case, positive sheaths are not common in normal operation.

Chapter 6

SIMULATIONS AND TESTS

Recent trends in Hall thruster design have shown an increasing interest on dual-mode efficient operation. The advantages are clear for this type of operation: on the one hand, a high thrust but low specific impulse regime allows for efficient orbit raising where the minimization of the transfer duration is the main constraint; on the the other hand, orbit correction tasks such as north-south station keeping can take advantage of the high specific impulse regime, which minimizes the mass consumption[28].

Several programs have already been launched in the last few years to design and qualify dual-mode Hall thrusters and the main problem that still remains is the operation at high specific impulse (or high discharge voltage). It is usually found experimentally that a decrease on efficiency appears at voltages higher than 600V-700V and it is claimed that one of the possible reasons is, among others, the excessive generation of doubly-charged ions, leading to ion populations of very different average velocities at the thruster exhaust.

However, recent results from Hofer and Gallimore [11] have shown that a monotonically increasing efficiency is possible if the magnetic field topology is optimized for high discharge voltages. Thus, disadvantages of multiple ionization seem not to be the only reason for the efficiency decrease at high specific impulse operation measured in other experiments.

A promising Hall technology for dual-mode operation is the two-stage design where an intermediate electrode is used to enhance the ionization and acceleration processes. Although the theoretical advantages of this type of thrusters are obvious, experiments tend to show that no clear benefit appears when two-stage operation is used [29, 30, 31]. This might be due to a poor understanding of the physical processes involved in this kind of thrusters where the intermediate electrode can change significantly the discharge characteristics. Ahedo and Parra[32] published a model of the two-stage discharge where they demonstrate that performance and efficiency depend much on the position and current of the intermediate electrode and, technical issues apart, predict relative efficiency enhancements of 20% for optimal values of the intermediate electrode parameters.

This chapter is aimed to analyze the results the new code is capable of producing precisely for these two kinds thrusters: single-stage high specific impulse and two-stage models. Besides, some parametric variations are also included to show the flexibility of the simulation code.

6.1   Performances

6.1.1   Performance characterization

This paragraph is intended to summarize the main definitions regarding thruster performance. When we analyze the efficiency of the plasma discharge of a Hall thruster, the natural parameter is the so-called anode efficiency

$$\eta_a = \frac{F^2}{2\dot{m}_a P_d} \tag{6.1}$$

where F is the thrust, $\dot{m}_a$ is the mass flow through the anode and P_d is the electrical power to sustain electrode and cathode currents; for a simple, single-stage thruster, $P_d = I_d V_d$. The anode efficiency can be split up into several partial efficiencies accounting each one for a different process inside the thruster. Thus, we write

$$\eta_a = K \, \eta_u \, \eta_{cur} \, \eta_q \, \eta_{vol,i+} \, \eta_{p,i+} \tag{6.2}$$

where

$$\eta_u = \frac{\dot{m}_{i,c}}{\dot{m}_a} \tag{6.3}$$

is the mass or propellant utilization (subscripts a and c refer to the anode and the streamsurface containing the virtual cathode, respectively);

$$\eta_{cur} = \frac{I_{di,c} V_d}{P_d} \tag{6.4}$$

is the current utilization (it represents the additional necessary electron current to maintain the thruster operation and can also be considered a way to characterize the ionization process);

$$\eta_{vol,i+} = \frac{P_{jet,i+}}{I_{di+,c} V_d} \tag{6.5}$$

is the voltage utilization based on singly-charged ion acceleration ($P_{jet,i+}$ is the singly-charged ion jet power at the domain exit);

$$\eta_{p,i+} = \frac{F_{i+}^2 / 2\dot{m}_{i+,c}}{P_{jet,i+}} \tag{6.6}$$

is a plume-divergence efficiency, based on singly-charged ion magnitudes (F_{i+} is the thrust due exclusively to singly-charged ions);

$$\eta_q = \frac{(I_{di+,c} + I_{di++,c}/\sqrt{2})^2}{(I_{di+,c} + I_{di++,c})(I_{di+,c} + I_{di++,c}/2)} \tag{6.7}$$

is the charge utilization ($I_{di+,c}$ and $I_{di++,c}$ are singly- and doubly-charged ion currents), which measures the influence of doubly-charged ions on the thrust ; and K accounts for minor contributions to η_a like the part of the thrust due to neutrals and electrons. Sometimes it is useful to use an internal efficiency as the product of current utilization and voltage utilization.

6.1.2   Nominal operation results

The Hall thruster taken as reference for the computations is of the SPT-100 type, which is characterized by the nominal properties of Table 1.

V_d	$\dot{m}$	B_{max}		P_d	η	F	I_{sp}
300 V	4.8 mg/s	230 G		1350 W	0.48	83 mN	1600 s

Table 6.1: SPT-100 nominal operating and performance parameters.

P_d	η	F	I_{sp}
1220 W	0.39	68 mN	1434 s

Table 6.2: SPT-100 simulated performance parameters.

The simulation results obtained with the conditions sketched in Fig.1.1 for the above operating parameters are in Table 2. Many other averaged performance variables can be found in figure 6.1 that has been extracted directly from the performance file generated by HPHall.

```
Nominal Voltage   [V]           = 300           Thrust[N]                        = 0.0676132
Voltage [V]                     = 300
Current [A]                     = 4.06514        Total power [W]                  = 1219.55
Current Oscillation Level [A]   = 1.01048        Total lateral wall loss[W]       = 376.519
Power   [W]                     = 1219.55        Thrust power [W]                 = 546.121
Max magnetic field (B-ave)[G]   = 249.629        Useful power [W]                 = 758.932
Anode magnetic field(B-ave)[G]  = 33.5621
                                                 Thrust efficiency                = 0.389799
Total current at anode[A]       = 4.06514        Internal efficiency              = 0.622304
Anode total ion current [A]     = -0.1687        Specific impulse[s]              = 1433.9
Anode single ion current [A]    = -0.165812
Anode double ion current [A]    = -0.00288894    PARTIAL EFFICIENCIES
Ion current to lateral wall[A]  = 1.57981        Thrust efficiency       = 0.389799
                                                 Coefficient K1          = 1.08383
Total ion beam current[A]       = 3.08159        Coefficient K2          = 0.992821
Single ion beam current[A]      = 2.77374        Charge efficiency       = 0.991879
Double ion beam current[A]      = 0.307846       Plume efficiency        = 0.711358
                                                 Propellant utilization  = 0.828559
Nominal Mass flux[kg/s]         = 4.8e-006       Current utilization     = 0.758047
Mass flux anode line[kg/s]      = 4.80831e-006   Voltage utilization     = 0.817413
Mass flux thruster exit[kg/s]   = 4.81353e-006

Beam total ion mass flux[kg/s]  = 3.98397e-006
Beam single ion mass flux[kg/s] = 3.77453e-006
Beam double ion mass flux[kg/s] = 2.09458e-007
Maximum ion beam mass flux[A]   = 4.8e-006
```

Figure 6.1: Main performance variables for the SPT-100 simulated thruster

Clearly, this simulation underestimates thruster efficiency. There are two kind of reasons. First, no attempt was made to optimize the 'empirical' parameters of the model, like the anomalous diffusion or the wall accommodation coefficients, both having a relevant impact on performances. The second reason lies on the plasma-wall interaction model, which leads to excessively high plasma recombination and energy losses at the walls. Depletion of the the tail of primary electrons[33, 34], two electron temperature models[26], and partial trapping of secondary emission[35] have been suggested to modify the common plasma-wall interaction model.

Apart from this overestimate of wall losses, the code is capable of reproducing well the main physical aspects of the discharge and can be used to analyze (qualitatively, at least) the influence of different operating parameters as discharge voltage or mass consumption.

Figure 6.2 depicts the most important variables for the nominal operation point. These results must be taken as a reference for the following sections.
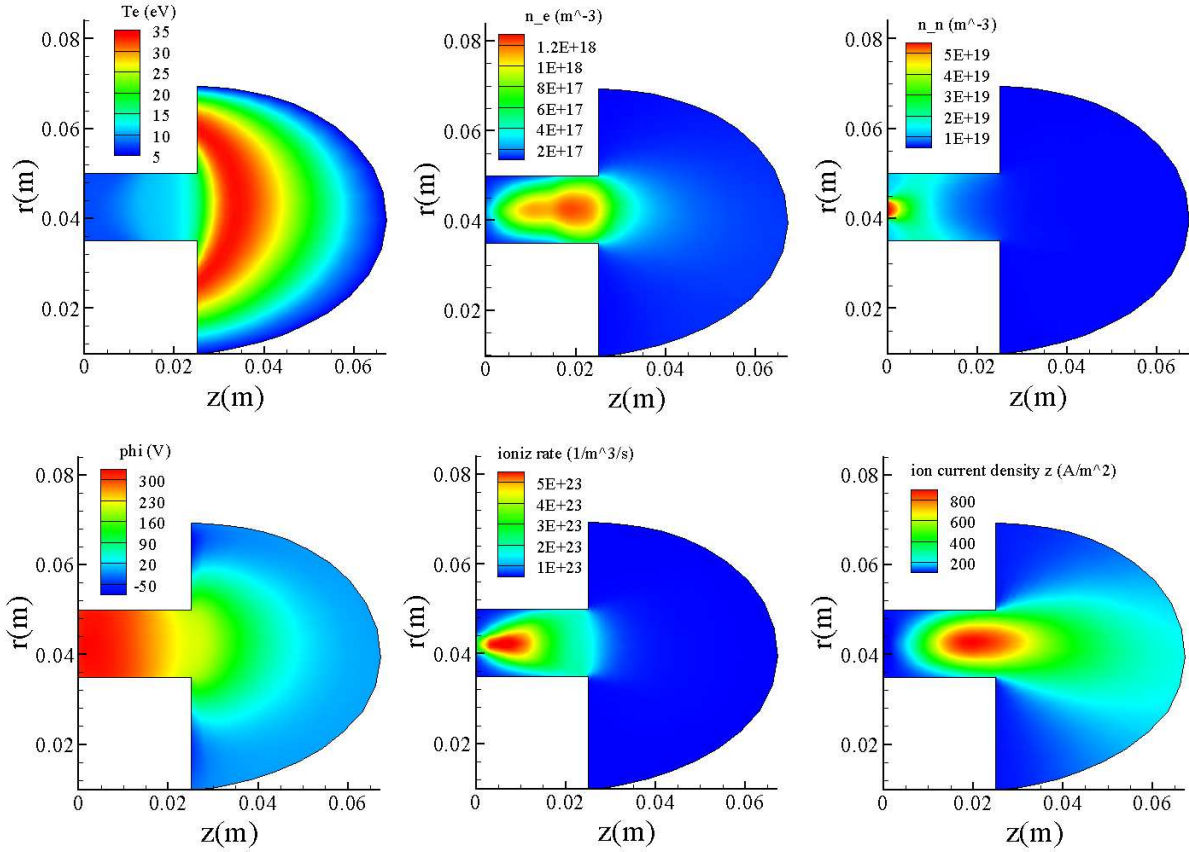
Figure 6.2: Temperature (T_e), electron density (n_e), neutral density (n_n) (upper figures), electric potential $(\phi(V))$, ionization rate $(\dot{n}_i)$ and ion current density (j_{iz})(lower figures) for the nominal operation point.

6.1.3 Estimates of numerical errors

HPHall is a non-stationary code with a strong oscillatory component in the solution. Thus, all 'time-averaged' variables have an associated error. This analysis is intended to evaluate the size of this error and determine the best trade-off between accuracy and computational effort.

To this end several runs have been performed with the same operating parameters and similar initial conditions. The only 'free' parameter in this study is the number of iterations used to average variables. In order to characterize the temporal error in averaged variables we define the following generic variables: the time-average and the typical deviation.

$$\langle X \rangle = \frac{1}{N_{its}} \sum_{i=1}^{N_{its}} X_i \qquad \sigma_X = \sqrt{\frac{1}{N_{its}} \sum_{i=1}^{N_{its}} (X_i - \langle X \rangle)^2} \qquad (6.8)$$

Figure 6.3 shows the results obtained for runs with 10000, 20000 and 40000 iterations. It can be seen that for all analyzed variables, the relative typical deviation is always smaller that 0.65% what implies that 75% of simulations have an uncertainty smaller than 1.3%. This value is acceptable and consistent with the numerical errors introduced with the different approximations.
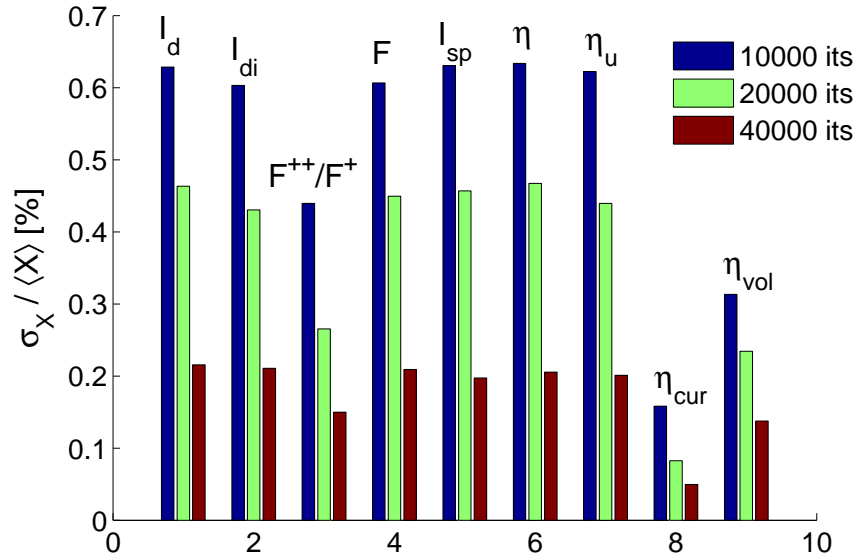
Figure 6.3: Relative typical deviation of different variables as a function of the number of averaged PIC iterations.

6.2   Parametric studies

In this paragraph some parametric variations are presented for the different parameters characterizing thruster operating conditions. To this end we start from the SPT-100 case analyzed in the previous chapter and the following parameters are varied continuously: anomalous diffusion coefficient, magnetic field strength, mass flow, thruster channel length. Note that multiple ionization is not considered in this analysis for the sake of simplicity.

6.2.1   Anomalous diffusion coefficient

In order to fit simulation results with experimental results the anomalous diffusion coefficient α_{ano} , Eq. (5.19), is normally modified until the performance is optimized. Figure 6.4 shows the corresponding results for this parametric variation. Increasing the anomalous diffusion coefficient causes the discharge current to increase and consequently the power also increases. Additionally, the higher the anomalous diffusion is, the lower the current utilization and internal efficiency are. Thus, the overall efficiency decreases dramatically as α_{ano} increases.
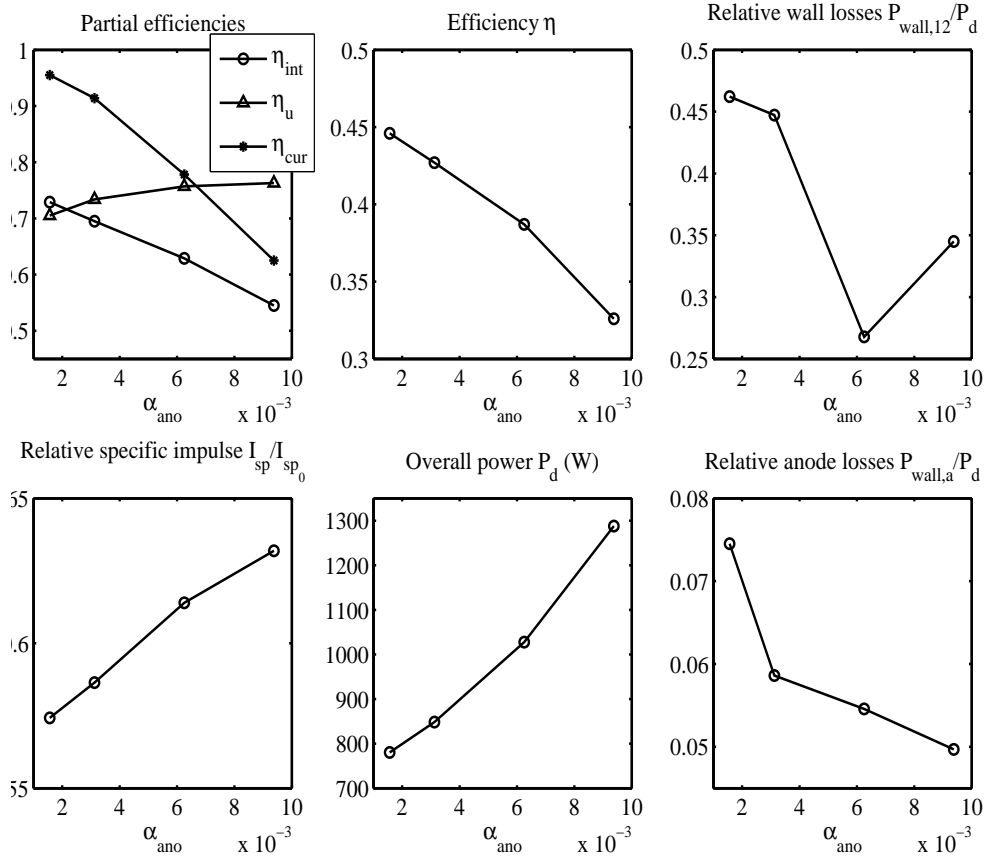
Figure 6.4: Parametric analysis. Anomalous diffusion coefficient variation α_{ano}.

6.2.2 Magnetic field strength

For a given magnetic circuit, increasing the current through the coils causes the magnetic field to increase proportionally. Then the magnetic field gradient also increases and consequently the thruster operation is greatly affected.

According to the results, increasing the magnetic field gradient tends to reduce the acceleration region and to move it downstream. Thus, it is closer to the maximum magnetic field. Normally, thrusters are designed so that the maximum magnetic field is at the thruster channel exit. That is why an improvement in the overall efficiency is observed due mainly to a better current utilization and lower wall losses. However, the non-dimensional specific impulse (I_{sp}/I_{sp_0} where $I_{sp_0} = \frac{1}{g_0} \cdot \sqrt{\frac{2eV_d}{m_i}}$) decreases slightly due to a poorer ionization. As expected, the overall power decreases because a lower electron current is required as the magnetic field strength increases.

Finally, anode losses are in general much smaller than ceramic wall losses since electron temperature near the anode is smaller and the ion back-streaming flow is much smaller the discharge current. Obviously, it is also important to take into account that the anode surface is also smaller than the ceramic wall surface.
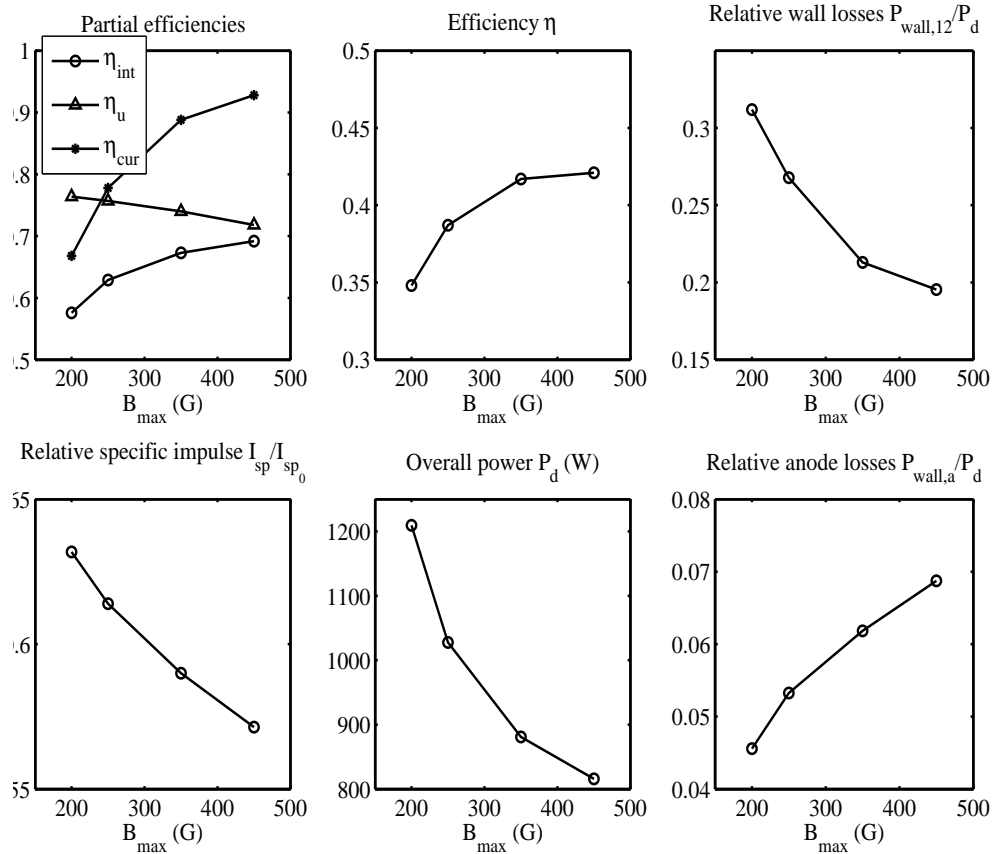
Figure 6.5: Parametric analysis. Magnetic field strength variation.

6.2.3   Channel length

This parametric variation consists on executing the program for several thruster geometries with a different channel length keeping the rest of geometrical parameters constant. The channel length is one of the most important variables from the design point of view. As it can be observed in figure 6.6, the current utilization η_{cur} decreases and the propellant utilization η_u increases due to the relative growth of the acceleration region and the relative reduction of the ionization region respectively. Thus, the overall efficiency shows a peak for a given optimal channel length (around 30 mm in this case). As in previous cases, the increase of the propellant utilization η_u also involves higher specific impulse and overall power (due to the increase of the discharge current I_d). Finally, as expected, wall losses increase as channel length increases.
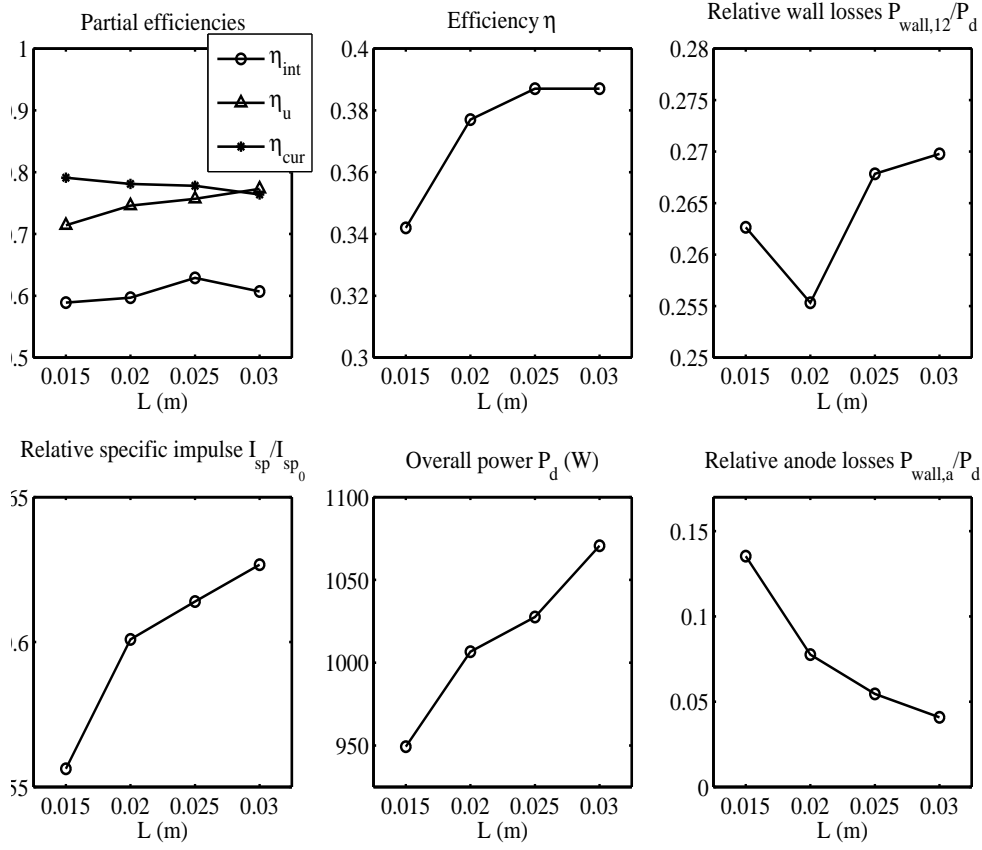
Figure 6.6: Parametric analysis. Channel length variation

6.2.4 Mass flow rate

Figure 6.7 shows the variation of some variables characterizing thruster operation. It can be observed that a higher mass flow rate causes an increase of the propellant utilization due to a more efficient ionization enhanced by a higher neutral density. On the other hand, both current utilization and internal efficiency decrease. Because of this behavior of the partial efficiencies the overall efficiency shows a minimum when increasing the mass flow rate. The overall power also changes due to the increase of the discharge current, which is proportional to the mass flow rate and the propellant utilization.
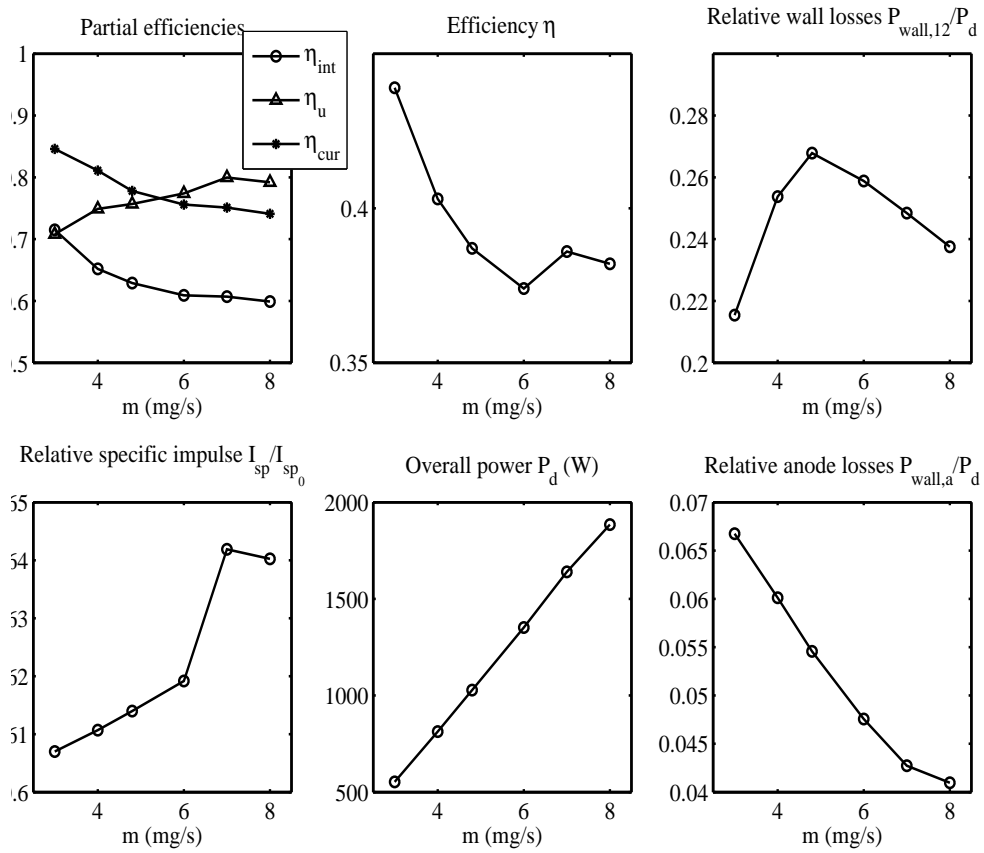
Figure 6.7: Parametric analysis. Mass flow rate variation $\dot{m}$.

6.3 High specific impulse thrusters

This section presents numerical results of Hall thrusters operating at high-specific impulse. The goal of these simulations is two-fold. On the one hand, we aim to better understand the plasma discharge at this operation conditions. On the other hand, we use them for testing the new simulation code. Here we focus on results for high-specific impulse and single-stage operation conditions.

Figure 6.8 displays the variation of the main parameters when the voltage is increased from 300V to 750V, and the magnetic field strength is increased proportionally to V_d; the rest of parameters remain nominal. As expected, the specific impulse and the thrust increase proportionally to $V_d^{1/2}$ rather well. Deviations are due to variations on propellant and voltage utilizations. The total discharge current remains constant through the entire range of variation of V_d due to the variation of the magnetic field strength commented above. As a consequence, the total power varies proportionally to the discharge voltage.
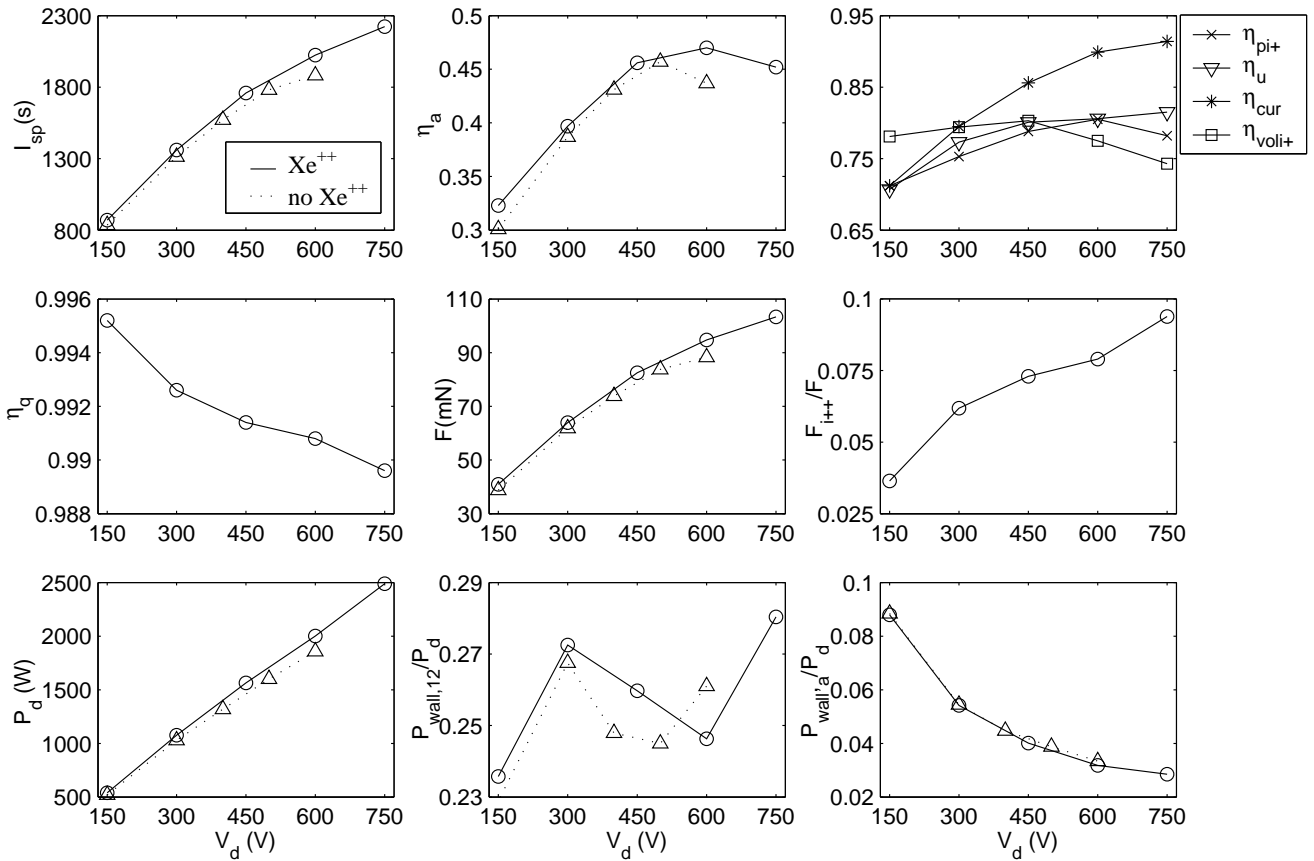
Figure 6.8: Variation of main operation parameters when varying the discharge potential V_d. $P_{wall,12}$ and $P_{wall,a}$ represent total energy losses to inner and outer walls and to the anode.

Efficiency increases up to 600V where a peak is found. The posterior decrease seems to be caused both by higher wall losses and a decrease of voltage utilization and plume divergence efficiency. The same parametric investigation has been performed switching off multiple ionization and the peak of efficiency remains. This contradicts the common argument that the decrease of efficiency at high voltages is due to doubly-charged ions, but seems to agree with Hofer and Gallimore who obtained a monotonically increasing efficiency by optimizing the magnetic field.

Multiple ionization influence is quantified by the charge utilization efficiency, η_q, and the contribution to thrust of doubly-charged ions (F_{i++}/F). At 750V the contribution of doubly-charged ions to thrust is as high as 10%, which emphasizes the importance of including and modelling them properly.

Figures 6.9 and 6.10 display profiles at the channel median and outer wall, respectively. Figure 6.11 shows 2D plots of the discharge at three discharge voltages. In all cases, time-averaged magnitudes (excluding initial transients) are plotted. Relative energy losses at the walls tend to decrease when increasing V_d except for the limiting case of 750V. This reduction on wall losses is due to a better acceleration process which prevents the ions from reaching the walls as shows the profile of the ion current to the outer wall, j_{Wi}, in figure 6.10. The anomaly encountered at 750V seems to be caused by a temperature peak inside the ionization chamber as it is shown on figure 6.9. This peak causes higher wall losses and modifies the electric potential fall through the channel. The optimized magnetic field topology proposed by Hofer-Gallimore in order to increase efficiency at high voltages is characterized by a near zero magnetic field strength precisely where our model predicts a peak on temperature. Thus, it must be numerically checked whether a magnetic field topology like that one could avoid the peak temperature and improve efficiency at high voltages. Figure 6.9 also plots the plasma density and equivalent charge number. Due to electron pressure and electric acceleration, the plasma tends to be confined near the anode for higher voltages. Thus, the ionization process is confined to that region too, as shown in figure 6.11.

Figure 6.9 also plots the plasma density and equivalent charge number. Due to electron pressure and electric acceleration, the plasma tends to be confined near the anode for higher voltages. Thus, the ionization process is confined to that region too, as shown in figure 6.11.
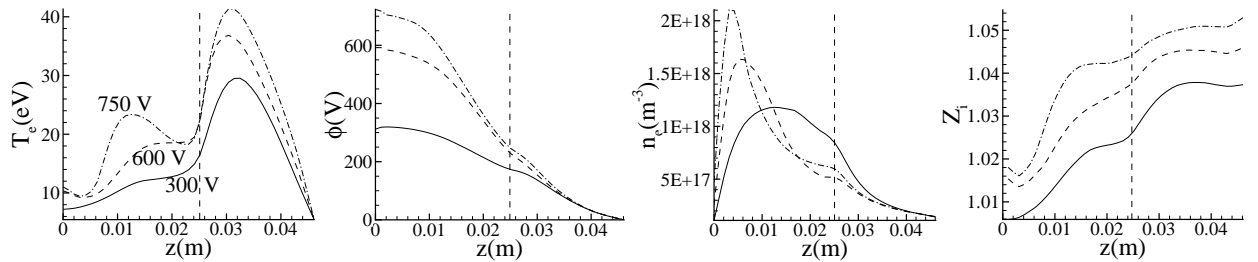
Figure 6.9: Electron temperature T_e, electric potential ϕ, electron density n_e and equivalent charge number Z_i profiles at different discharge voltages (V_d= 300 V(solid), 600 V(dashed) and 750 V(dashed-dotted)). All variables are evaluated at the chamber median (r=0.0425m). The vertical dashed line represents the thruster exit.
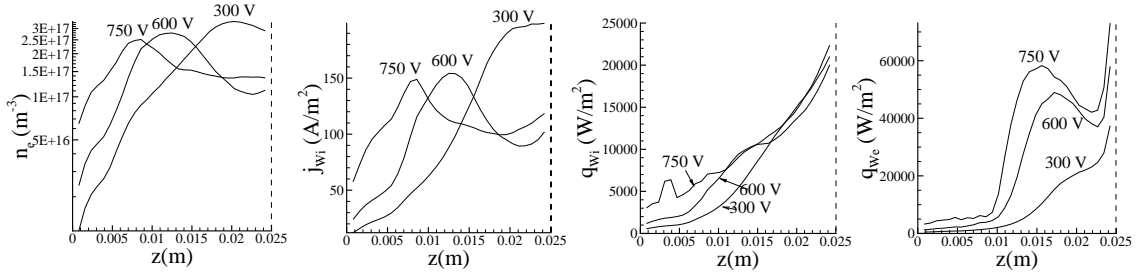
Figure 6.10: Electron density, n_e, ion current to wall, j_{Wi}, ion energy flux to wall, q_{Wi}, and electron energy flux to wall, q_{We} for V_d= 300 V, 600 V and 750 V. All variables are evaluated at the outer wall (r=0.05m). The vertical dashed line represents the thruster exit.
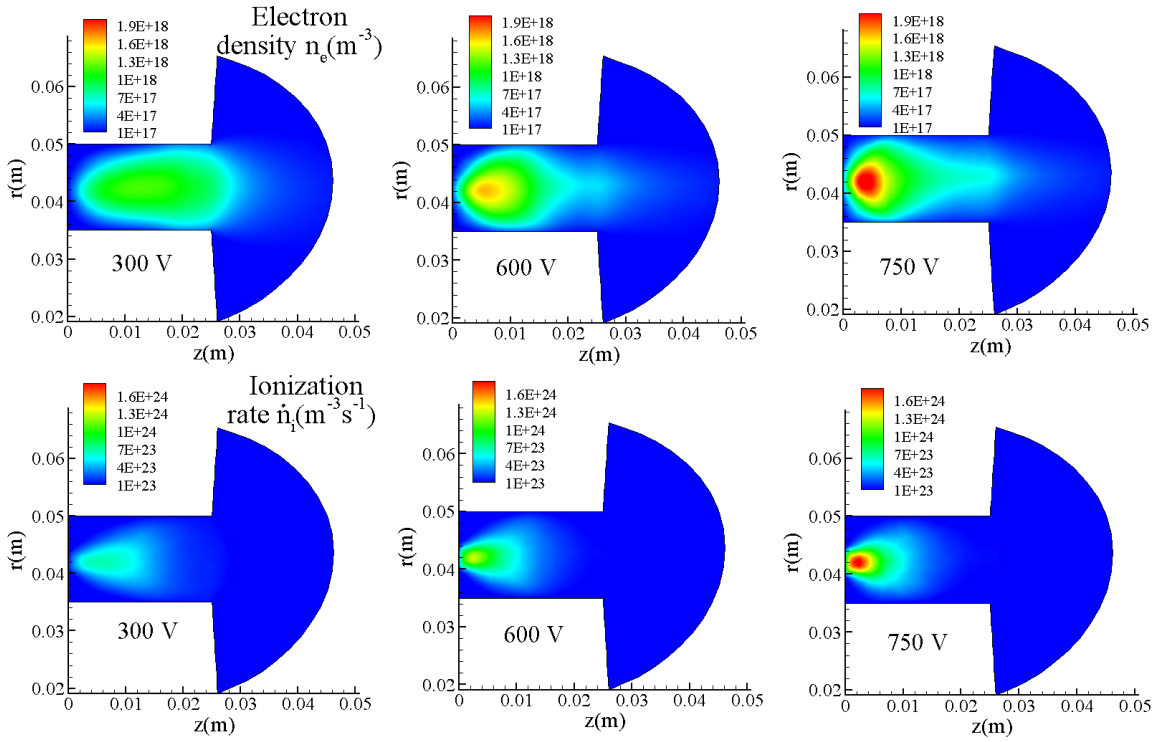
Figure 6.11: Electron density, n_e (upper figures), and total ionization rate, $\dot{n}_i$ (lower figures) at $V_d =$ 300 V, 600 V and 750 V, for the previous parametric variation.

6.4 Two-stage Hall thruster simulations

Figure 6.12 and table 6.3 show the profiles of the main plasma variables and performance parameters when an intermediate electrode 2mm wide, located at z=21mm on the outer wall, and emits different electric currents. Rest of parameters remain nominal, even the magnetic field strength and profile. Both propellant and voltage utilization tend to increase when augmenting the electrode current. However, since the magnetic field has not been optimized (as Ahedo and Parra [32] did) the current utilization and thus the anode efficiency decrease.

$I_{electrode}(A)$	η_a	$I_{sp}(s)$	η_{cur}	η_u	$\eta_{vol,i+}$	$\eta_{p,i+}$
no electrode	0.40	1360	0.80	0.77	0.79	0.75
0.26	0.42	1443	0.78	0.81	0.80	0.78
0.79	0.37	1408	0.70	0.78	0.81	0.78
1.37	0.33	1380	0.62	0.75	0.81	0.79

Table 6.3: Performance parameters for different currents through the electrode corresponding to figure 6.12.
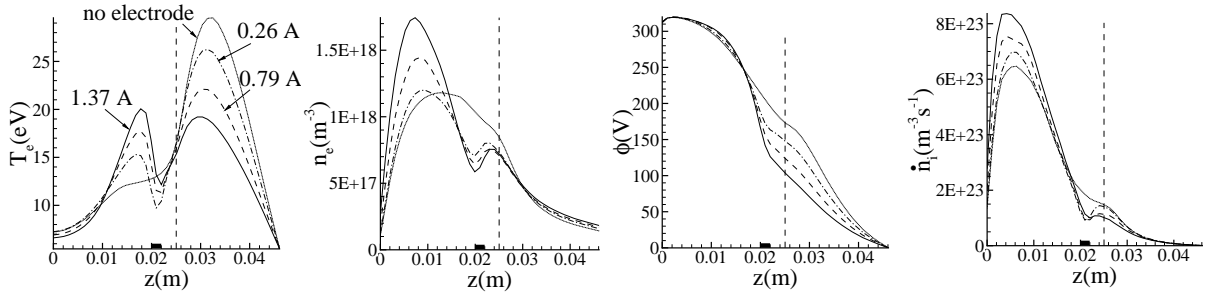
Figure 6.12: Electron temperature, T_e, electron density, n_e, electric potential, ϕ, and total ionization rate, $\dot{n}_i$, profiles for different currents through the electrode. The electrode is 2mm wide and is located on the outer wall at axial position z=21mm. The vertical dashed line represents the thruster exit.

$z_{electrode}(mm)$	$I_{electrode}(A)$	η_a	$I_{sp}(s)$	η_{cur}	η_u	$\eta_{vol,i+}$	$\eta_{p,i+}$
-	no electrode	0.40	1360	0.80	0.77	0.79	0.75
21	1.37	0.33	1380	0.62	0.75	0.81	0.79
16	1.46	0.37	1550	0.61	0.82	0.87	0.81

Table 6.4: Performance parameters for different electrode locations corresponding to figure 6.13.

Table 6.4 displays the different performance variables when modifying the electrode location and maintaining almost constant the electrode current. It is clear that the electrode location affects the thruster response. In fact, in the new electrode location (z=16mm) the anode efficiency is higher than in the previous case. This influence agrees well with the conclusions of Ahedo and Parra[32]. We remind again that the current utilization is very low due to the non-optimal magnetic field.
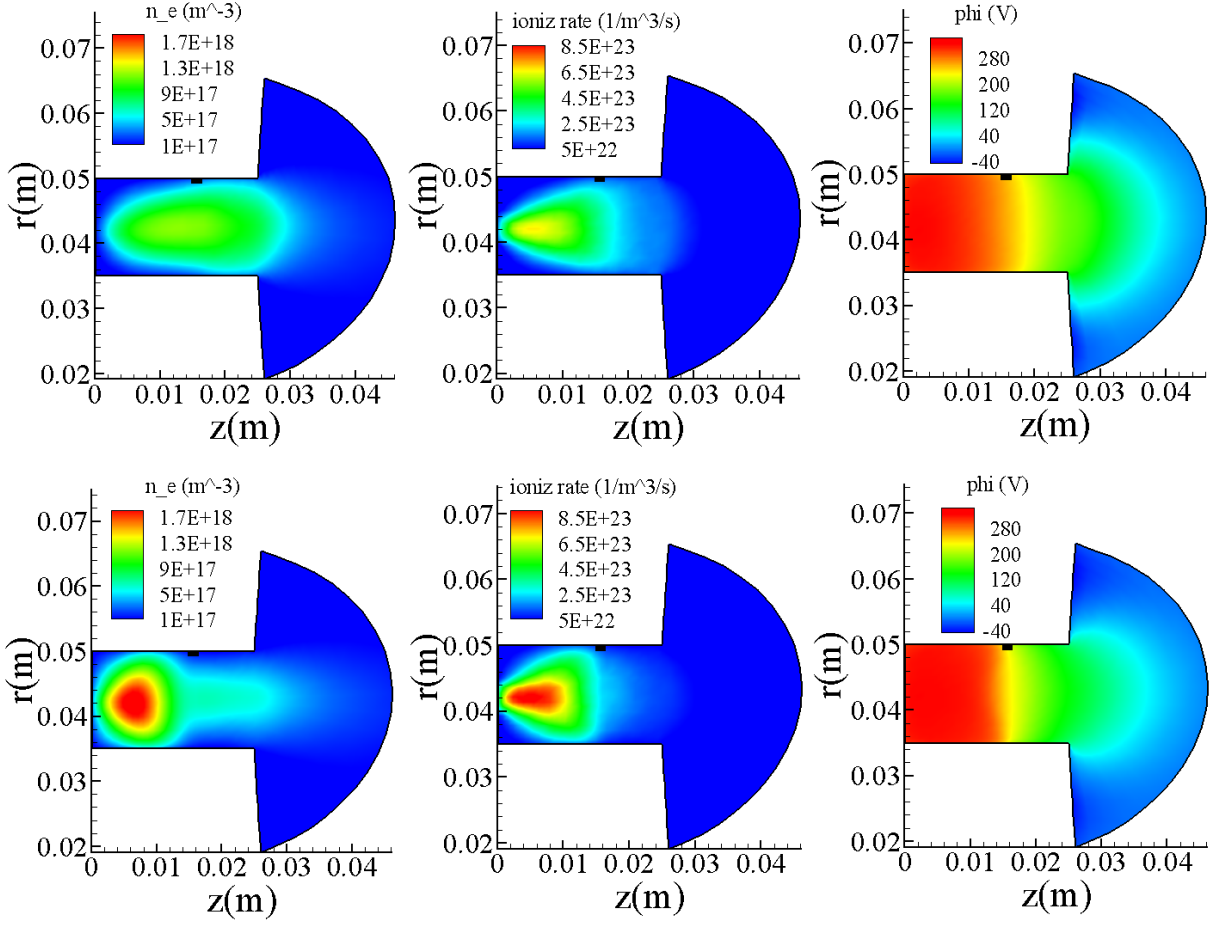
Figure 6.13: Electron density, n_e, ionization rate, $\dot{n}_i$, and electric potential, ϕ, contours for reference case (upper figures) and a case with an electrode 2mm wide on the outer wall at 16mm from anode (lower figures).

6.5 An external cathode model

In a Hall thruster an external cathode injects the electron current, I_C, required to neutralize the ion beam and to sustain the plasma discharge inside the thruster. For a thruster with ceramic walls, that current is equal to the current through the anode, and it is known as the discharge current, I_d.

Let C be the external boundary (in the near plume) of the computational domain, which coincides with a magnetic streamline; see Fig. 6.14. HPHall-2 considers the surface C as the neutralization surface. First, the particle sub-code computes the ion current I_{iC} crossing that boundary. Then, the electron current injected *inwards of* the domain is $I_{eC}^- = I_C - I_{iC}$. This electron current is a boundary condition at C of the electron equations in λ. A second boundary condition is the 'cathode reference potential' ($\phi = 0$ in our plots, generally) set at a point on line C. A third boundary condition, required by the heat equation is the temperature at C, T_{eC}, which we identify as the temperature of the injected electrons. HPHall-2 does not solve the region beyond the neutralization surface.

The new electron model presented in Ref. [14] admits the injection/collection of electrical current through the lateral walls of the thruster, illustrated in Eq.5.18. This enhancement was envisaged to study thrusters with two-stages or internal segmented electrodes, but it is clear that it can also be used for a more flexible and realistic treatment of the electrode injection process. Hence, we decided to model the cathode as an emissive electrode placed in the external walls of the thruster.

Emissive electrodes require a different sheath model for this type of electrodes. This is based on space-charge saturated sheaths and was presented in Ref. [36]. Figure 6.15 plots, for an emissive-electrode sheath, the curves relating the sheath potential fall, ϕ_{WQ}, the net electric current density j_W and the density flux of electron total energy through the sheath edge Q (i.e. the boundary of the quasineutral domain), q_{eQ}^{tot}.
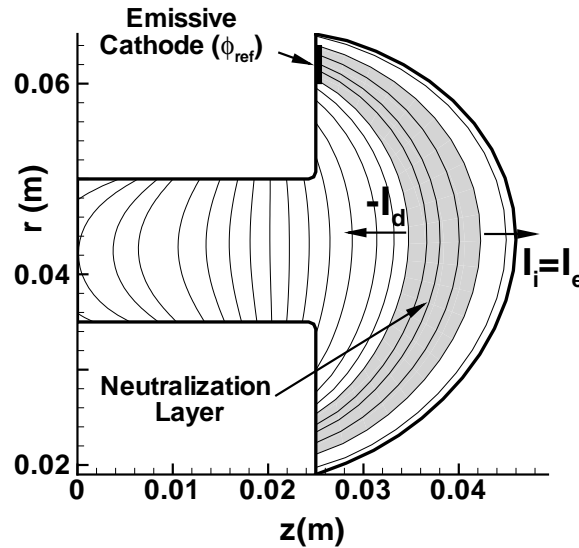
Figure 6.14: Scheme for the new cathode model. The shadowed region is the neutralization layer. The potential of reference is set at the wall position of the cathode.
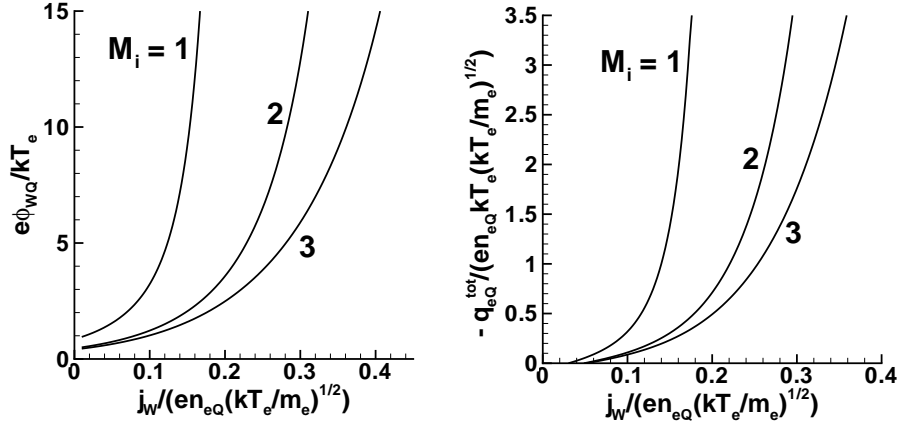
Figure 6.15: Emissive electrode response. Relations among $j_W = \vec{j} \cdot \vec{n}$, the sheath potential fall ϕ_{WQ}, and $q_{eQ}^{tot} = \vec{q}_{eQ}^{tot} \cdot \vec{n}$ for ion Mach numbers $M_i = 1$, 2, and 3. Electrons are emitted cold by the emissive cathode.

The neutralization model we propose is the following. An electrical current I_C is injected into the plasma domain through an annular cathode of finite length, placed on the outer external wall, Fig.6.14. The cathode surface and I_C define the current density j_W. The sheath model determines the energy flux q_{eQ}^{tot} and the sheath potential fall, ϕ_{WQ}. The fluxes j_W and q_{eQ}^{tot} are source terms for the electron equations in λ (hence, I_C is no more a boundary condition). Setting the 'cathode reference potential' at the cathode, the potential fall ϕ_{WQ} provides the boundary condition required for ϕ in the quasineutral domain. The electric current I at the boundary surface C is now set to zero (i.e. the ion beam is neutralized). For the heat equation we impose the condition $\partial T_e / \partial \lambda|_C = 0$, which we intuit more correct than to set the temperature T_{eC}.

Figures 6.17 to 6.18 show the results of a simulation for a cathode placed between $r = 60$ mm and $r = 64$ mm in the external wall, which injects about $\sim 250 \text{mA/cm}^2$, resulting in a total current of ~ 4A. The magnetic lines intersecting the cathode define the *neutralization layer*. The electrical current increases from zero at the external boundary to the ~ 4A current when
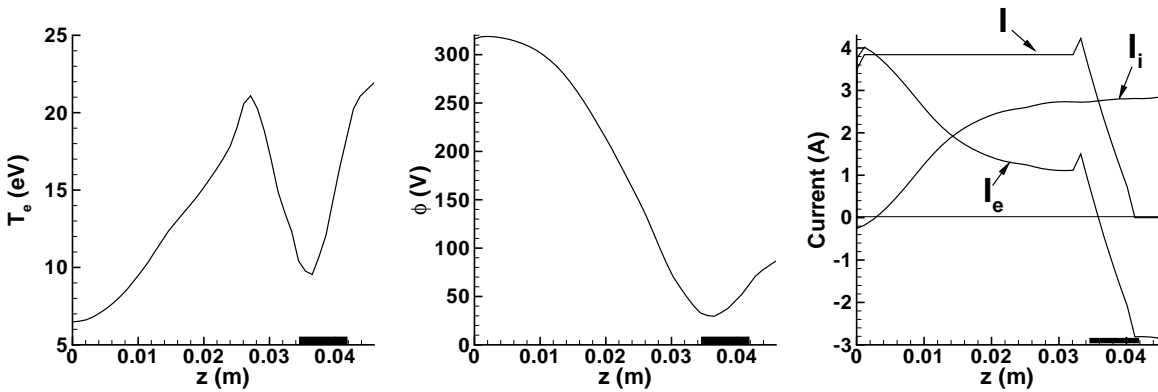
Figure 6.16: Plasma response along the channel median for the case of Fig.6.17. The neutralization layer cuts the median at 34.6-41.8mm. (The peak on $I(z)$ is a numerical defect).
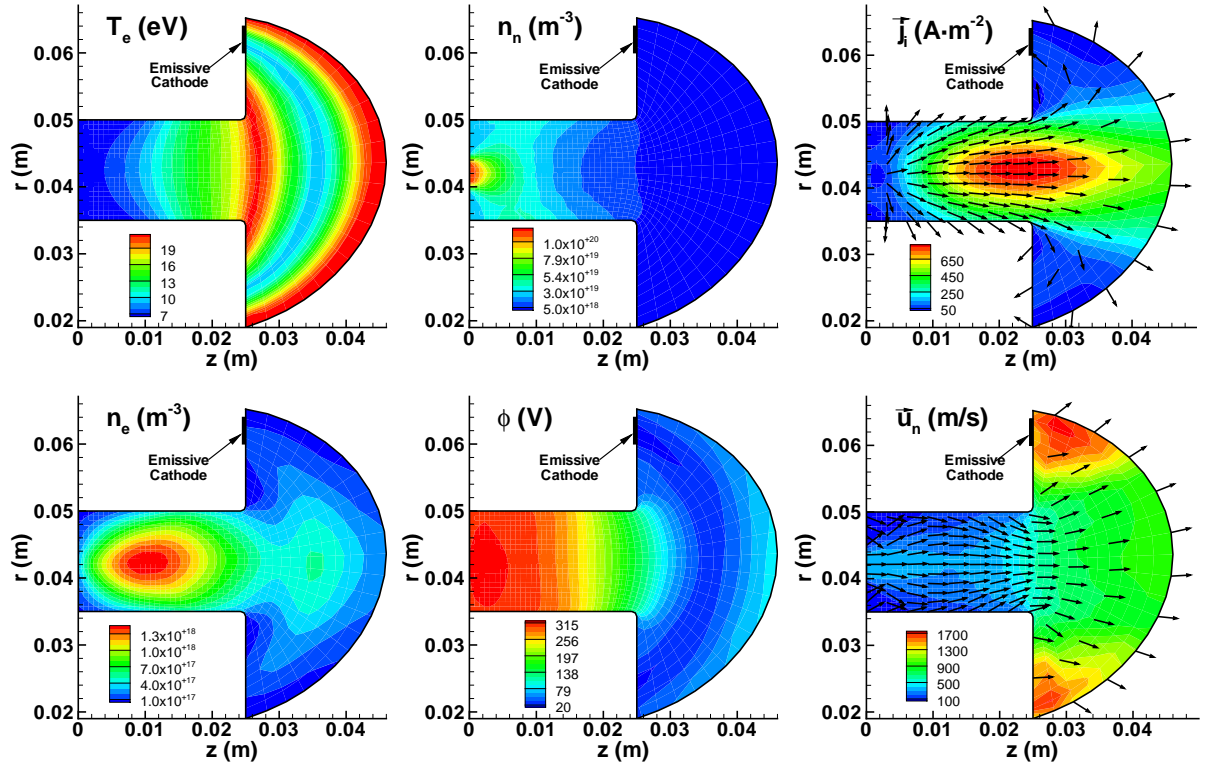
Figure 6.17: 2D plasma response for a cathode placed in the external wall. Arrows for $\vec{j}_i$ and $\vec{u}_n$ do not scale with the vectors magnitudes.

crossing the neutralization layer (Fig. 6.16). Of course, this variation of the electric current comes mainly from the injection of electrons, I_e changing from negative to positive values across the neutralization layer. In the present model, we impose boundary conditions on the gradients of $T_e(\lambda)$, but the value of T_e is imposed nowhere (in the quasineutral plasma). Hence, we find very positive that the simulation yields $T_e \sim 8 - 10\text{eV}$ in the neutralization layer, in good agreement with experimental results. That energy is imparted to the cathode electrons by the potential fall at the cathode sheath; this fall is about 10-15V (Fig.6.18), a very good value too. Along the channel median, plasma potential is minimum in the neutralization region (Fig.6.16), which makes sense, since injected electrons must be driven out of that region (both inwards and outwards). In this process electrons are heated by Joule effect. The strength of Joule heating depends on the plasma perpendicular resistivity, which is proportional to the magnetic strength B (or to B^2 if Bohm diffusion is negligible). For this simulation, the magnetic strength is 200G, at the chamber exit, 130G at the cathode position, and 90G at the external boundary. This would explain that Joule heating is similar outwards and inwards of the neutralization layer. Clearly, the value of T_e at the external boundary is excessive. We expect to correct this defect by placing the cathode more outwards.

The local maximum of n_e at the median of the neutralization layer (Fig. 6.17) would be due by the concentration of slow ions near the minimum of ϕ. Notice in Fig. 6.18 that the plasma density at the thruster external walls is of the order of 10^{16}m^{-3}, yielding Debye lengths of 0.33 mm, thus keeping valid there the hypothesis of quasineutrality.
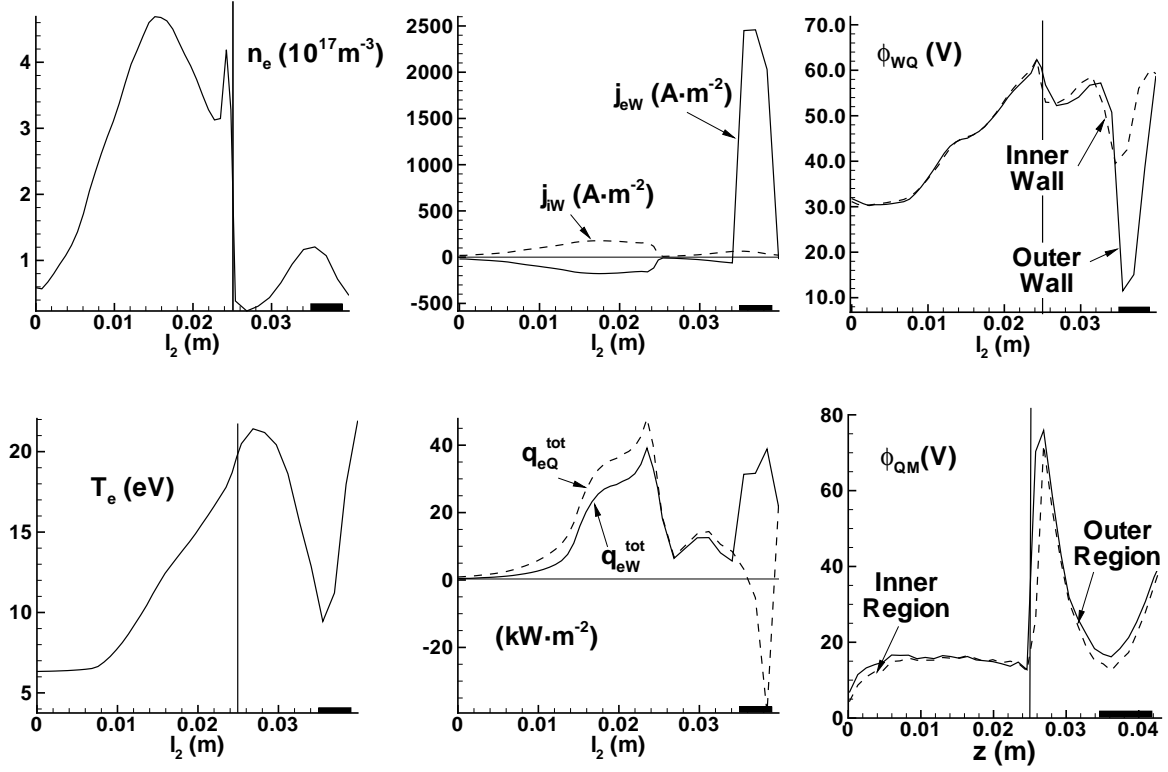
Figure 6.18: Plasma response along the inner and outer walls for the case of Fig.6.17. l_2 refers to the location along the wall. The sign of scalar currents(j) and energy fluxes (q^{tot}) to the walls is determined by the outwards vector $\mathbf{n}$. ϕ_{WQ} is the potential fall at the inner/outer sheath. $\phi_{QM}(z)$ is the potential fall at each streamline $\lambda(r_M, z)$ between the channel median $(r = r_M)$, and the inner/outer sheath edge Q.

Appendix A

TRANSITION FROM NEGATIVE TO POSITIVE ANODE SHEATH

This annex has been submitted for publication in Physics of Plasmas as an independent paper entitled 'Presheath/sheath model of the Hall thruster near-anode region for positive and negative falls'.

A.1 Introduction

There exists a limited understanding of the plasma behavior in the near-anode region of a Hall thruster discharge and its influence on the thruster operation. Experiments and models have centered the research on the ionization and acceleration regions, which seem more relevant for the plasma and thruster responses and are more accessible to direct plasma measurements. Nonetheless, the plasma behavior in the near-anode region is important in determining the anode heating and can affect the stability of the whole discharge. Zhurin *et al.* [37], in a review of the large Russian experience on Hall thrusters, assert that, under normal operation, electron thermal transport is more than sufficient to sustain the discharge and thus a negative (i.e. electron-repelling) sheath needs to be formed. When the thermal flux is insufficient to conduct the discharge current a positive (i.e. electron-attracting) sheath develops; this situation arises for low propellant flows and results in the discharge easily becoming extinguished [37].

Negative sheaths are ion-attracting and result in a noticeable ion backcurrent in the rear part of the chamber. Ion backcurrents (existing for up to a 60% of the channel length) were reported experimentally by Bishaev and Kim [38] and Kim [39]. Direct measurements of the near-anode region have been made recently by Dorf *et al* [40, 41]. In Ref. [40], positive and negative anode falls are found, depending on (i) the metallic anode being clean or coated by a dielectric film, and (ii) the values of the control parameters (discharge voltage V_d, mass flow, etcetera). For clean anodes, potential falls were negative preferentially and tended to decrease when V_d was decreased. In Ref. [41], the near-anode region for clean anodes and three different magnetic configurations are investigated. Since the magnetic lines intersect obliquely the anode, the anode potential fall is not uniform. A positive sheath was measured in part of the anode only for a particular magnetic configuration (which presented an intermediate zero magnetic-field point). Since this saddle point was near the exit of the chamber, its relation with the

behavior of the anode fall is unclear.

The fluid and hybrid(particle-in-cell/fluid) models of Fife [16], Ahedo, Martínez-Sánchez, and co-workers[4],[21],[3], and Barral *et al.* [26] assume the existence of a negative sheath and recover the ion backcurrent region of Bishaev-Kim experiments. In agreement with the observations of Ref. [40], these models also show that, when V_d *decreases*, the anode fall decreases and eventually vanishes. However, Ahedo *et al.* [5] pointed out that electron inertial effects become relevant before the negative sheath vanishes, thus affecting the consistency of the diffusive approximation generally used for modelling the electron fluid. Ahedo and Rus[8] proposed a discharge model with partial electron inertia effects and demonstrated that, for small anode falls, electron inertia limits the electron azimuthal energy to values of the order of the electron internal energy, thus also bounding the energy deposition at the anode. Ahedo and Rus used an anode sheath model proposed by Dorf *et al.* [42], which consists of two regimes: the first one corresponds to the classical large negative sheath solution; the second one assumes that there is no anode sheath. The transition between both lies at the point where the electron flux from the quasineutral discharge into the anode sheath equals the electron thermal flux based on a Maxwellian electron velocity distribution function(VDF).

However, Dorf's no sheath model presents several inconsistencies, that have motivated the present work. First, the assumption that the electron VDF in the anode sheath approaches a near-full Maxwellian distribution is valid only for large negative sheaths. As the negative potential fall tends to zero the electron VDF should approach a half-Maxwellian distribution, which modifies the matching parameters of the sheath and presheath solutions; indeed, it will shown that a complete set of matching conditions between the partially kinetic sheath and the fluid presheath is not obvious. Second, there is no clear extension of Dorf's model into a positive sheath regime. Third, in a positive sheath a kinetic formulation for ions must be used, whereas the electron flux perpendicular to the sheath is expected to be 'supersonic' (in the sense given by the appropriate Bohm condition), which means that electron perpendicular inertia terms (not included in Ref. [8]) cannot be dismissed in the anode presheath.

This paper presents a one-dimensional(1D), two-region model of the near-anode region, which takes into account full inertia terms of ions and electrons. A two-region formalism, based on the asymptotic limit $\lambda_D \ll \ell_{ps}$, with λ_D the Debye length and ℓ_{ps} the spatial scale of the quasineutral anode presheath, is invoked. The goals are to obtain solutions of the near-anode region for the negative and positive sheath regimes, and to demonstrate the existence of a continuous parametric transition between positive and negative falls. Section II discusses a quasineutral, fluid model for the anode presheath and derives a generalized Bohm condition for the anode transition. Section II discusses which is the appropriate kinetic model for the repelled species in a weak sheath. Results are analyzed in Section IV.

A.2   Anode presheath

Figure A.1(a) sketches the two-region model of the near-anode region. The anode is planar, metallic, and clean; it collects all ions and electrons reaching it; secondary particle emission is neglected. The anode sheath AB is seen as a discontinuity in the scale ℓ_{ps} of the anode presheath. Solutions for anode sheath and presheath must be matched at the sheath edge (point B).
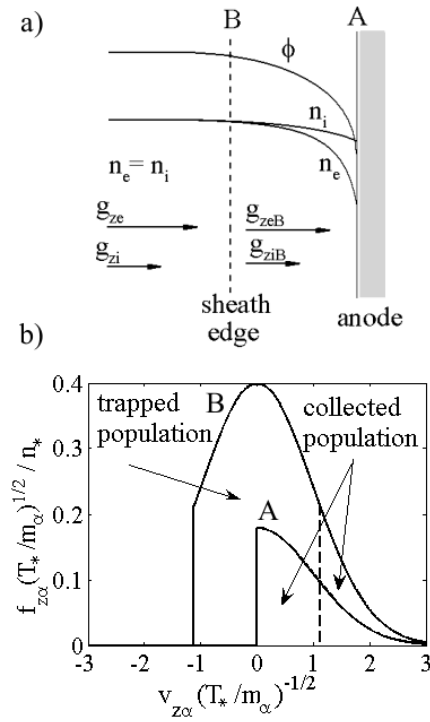
Figure A.1: (a) Sketch of a negative anode sheath and the near-anode region. (b) The cut-off Maxwellian of (repelled) electrons at the negative sheath edge B ($f_{z\alpha} = 0$ for $v_{z\alpha} < -\sqrt{2e\phi_{AB}/m_e}$) and at the anode A ($f_{z\alpha} = 0$ for $v_{z\alpha} < 0$); ϕ_{AB} is the sheath fall.

We propose a presheath model that omits or simplifies those aspects and phenomena that are not essential to understand the near-anode region. Thus, we neglect: (1) plasma production (by either ionization or wall recombination); (2) variations of the ion and electron temperatures; (3) variations on the electron gyrofrequency ω_e (> 0) and the electron (total) collision frequency $\nu_{e_{ps}}$. Formally, this means that the presheath extension ℓ is smaller than the spatial scales characterizing these processes. The presheath model consists of equations for the plasma density, $n = n_e = n_i$, the ion axial velocity u_{zi}, the electron (axial and azimuthal) velocities, u_{ze} and $u_{\theta e}$, and the electric potential ϕ:

$$n_e u_{z\alpha} \equiv g_{z\alpha B} = \text{const}, \quad \alpha = i, e, \tag{A.1}$$

$$(m_i u_{zi}^2 - T_{iB})\frac{1}{u_{zi}}\frac{du_{zi}}{dz} = -e\frac{d\phi}{dz}, \tag{A.2}$$

$$(m_e u_{ze}^2 - T_{eB})\frac{1}{u_{ze}}\frac{du_{ze}}{dz} = e\frac{d\phi}{dz} + m_e(\omega_{eB}u_{\theta e} - \nu_{eB}u_{ze}), \tag{A.3}$$

$$u_{ze}\frac{du_{\theta e}}{dz} = -\omega_{eB}u_{ze} - \nu_{eB}u_{\theta e}. \tag{A.4}$$

Subscript B has been applied to magnitudes that are assumed constant. All these constants (in particular, the ion and electron local fluxes and the local Hall parameter) are inputs of the presheath model, which would be determined from the matching with the solution for the rest of the thruster chamber. This is not afforded here; thus, the presheath equations are integrated from a location 'far from the anode' (which is defined more precisely below) to the sheath edge. We will focus the analysis on situations with $\omega_{eB}/\nu_{eB} \geq O(1)$.

Equation (A.2) yields a explicit expression for $\phi(u_{zi})$,

$$e\phi + \frac{1}{2}m_i u_{zi}^2 - T_{iB}\ln u_{zi} = \text{const}. \tag{A.5}$$

From Eq. (A.1) and quasineutrality the two axial velocities are related by

$$u_{zi}/u_{ze} = g_{ziB}/g_{zeB}. \tag{A.6}$$

In the Hall thruster discharge, the ion-to-electron (i-e) flux ratio can be expressed as $g_{ziB}/g_{zeB} = I_{iA}/I_d - I_{iA}$, where I_d is the discharge (or anode) current and I_{iA} is the ion back-current at the anode. For normal thruster operation $I_{iA}/I_d < 10\%$ typically, and $g_{ziB}/g_{zeB} \approx I_{iA}/I_d$.

Adding Eqs. (A.2) and (A.3), one has

$$\left[m_e u_{ze}^2 + m_i u_{zi}^2 - (T_{eB} + T_{iB})\right]\frac{1}{u_{ze}}\frac{du_{ze}}{dz} = m_e(\omega_{eB}u_{\theta e} - \nu_{eB}u_{ze}), \tag{A.7}$$

which does not include the electric field. Equations (A.4), (A.6), and (A.7) determine the three relevant velocity components of the plasma. Notice that Eq. (A.7) does not include the electric force. Thus, as long as ω_{eB}/ν_{eB} is large, the effective axial accelerating force on the plasma is the magnetic force on electrons.

Since u_{ze} cannot become zero, Eqs. (A.4) and (A.7) state that the *only* singularity (which we identify with the sheath edge B) of the presheath model corresponds to

$$m_e u_{zeB}^2 + m_i u_{ziB}^2 = T_B \equiv T_{eB} + T_{iB}. \tag{A.8}$$

This expression, which includes both u_{zeB} and u_{ziB}, is the sonic condition for this plasma with two drifting species. If both sides are multiplied by n_{eB}, it establishes the known condition that the plasma pressure is equal to the plasma axial momentum flux at a sonic point. We will refer to Eq. (A.8) as the *sonic Bohm condition* since at the sheath side of B, Eq. (A.8) must coincide with the (marginal) Bohm condition for the existence of a valid sheath solution.

It is important to observe that, were $d\phi/dz$ an external electric field, Eqs. (A.2) and (A.3) would yield that the ion and electron fluxes could present singular points at $u_{zi} = \sqrt{T_{iB}/m_i}$ and $u_{ze} = \sqrt{T_{eB}/m_e}$, respectively. However, since the electric field is self-adjusted by the quasineutral plasma, it acts as an additional pressure force and the above two 'sonic' points are just regular points of the plasma flow, where the right-hand side of Eqs. (A.2) and (A.3) vanish. In particular, Eq. (A.2) states that the electric field is zero at $u_{zi} = \sqrt{T_{iB}/m_i}$.

Using Eq. (A.6) and the sonic condition (A.8), the ion and electron axial velocities at point B satisfy

$$u_{ziB}^2 = \frac{T_B g_{ziB}^2}{m_i g_{ziB}^2 + m_e g_{zeB}^2},$$
$$u_{zeB}^2 = \frac{T_B g_{zeB}^2}{m_i g_{ziB}^2 + m_e g_{zeB}^2}. \tag{A.9}$$

There are three distinguished regimes for the near-anode region:

$$\text{(N)} \quad \frac{g_{ziB}}{g_{zeB}} \gg \sqrt{\frac{m_e}{m_i}} : \quad u_{ziB}^2 \simeq \frac{T_B}{m_i}, \quad u_{zeB}^2 \ll \frac{T_B}{m_e}, \tag{A.10}$$

$$\text{(I)} \quad \frac{g_{ziB}}{g_{zeB}} \sim \sqrt{\frac{m_e}{m_i}} : \quad u_{ziB}^2 \sim \frac{T_B}{m_i}, \quad u_{zeB}^2 \sim \frac{T_B}{m_e}, \tag{A.11}$$

$$\text{(P)} \quad \frac{g_{ziB}}{g_{zeB}} \ll \sqrt{\frac{m_e}{m_i}} : \quad u_{ziB}^2 \ll \frac{T_B}{m_i}, \quad u_{zeB}^2 \simeq \frac{T_B}{m_e}. \tag{A.12}$$

Regime N corresponds to the classical low-speed, diffusive-limit for the electrons. Regime P represents the opposite situation: the ion velocity (near the anode) is negligible, plasma dynamics are dominated by the electron fluid, and the sonic condition determines u_{zeB}. Regime I represents the intermediate case with ion and electron kinetic energies of the same order.

Since $u_{ze}u_{\theta e} < 0$, the right-hand-side of Eq. (A.7) never vanishes. Therefore, point B is necessarily singular with

$$-\frac{dn_e}{dz}\Big|_B, \frac{du_{ze}}{dz}\Big|_B, \frac{du_{zi}}{dz}\Big|_B, \to +\infty, \tag{A.13}$$

and

$$\frac{d\phi}{dz}\Big|_B \times \text{sign}(m_i u_{ziB}^2 - T_{iB}) \to -\infty. \tag{A.14}$$

These derivatives are infinite in the quasineutral scale of the presheath. Indeed, they are indicating the transition to the much smaller spatial scale of the non-neutral Debye sheath, where gradients are proportional to the inverse of the Debye length. Only the derivative of $u_{\theta e}(z)$ is regular at point B, and $u_{\theta e}$ is going to be constant inside the Debye sheath.

The sign of $d\phi/dz|_B$ determines whether the anode sheath is going to be positive or negative. Equation (A.14) states that there is a *single no-sheath case* separating the negative- and

positive- sheath regimes, which is characterized by

$$\frac{g_{ziB}}{g_{zeB}} = \sqrt{\frac{m_e T_{iB}}{m_i T_{eB}}} : \quad u_{ziB}^2 = \frac{T_{iB}}{m_i}, \quad u_{zeB}^2 = \frac{T_{eB}}{m_e}. \tag{A.15}$$

For the no-sheath case the electric field at the anode is

$$e \frac{d\phi}{dz}\bigg|_B = -\frac{T_{iB}}{T_{iB} + T_{eB}} m_e (\omega_{eB} u_{\theta eB} - \nu_{eB} u_{zeB}), \tag{A.16}$$

that is, the anode attracts electrons mainly.

A.3   Anode sheath

According to the above presheath model, a negative sheath is expected for

$$\frac{g_{ziB}}{g_{zeB}} > \sqrt{\frac{m_e}{m_i}}, \quad u_{ziB}^2 > \frac{T_{iB}}{m_i}, \quad u_{zeB}^2 < \frac{T_{eB}}{m_e}, \tag{A.17}$$

and a positive sheath arises for the opposite inequality signs. Therefore, for both sheath regimes, the attracted species enters 'supersonically' into the sheath, whereas the repelled species presents a 'subsonic' drift. Hereafter we present the formulation for a negative sheath. Because of the symmetry between the two sheath types, the solution for a positive sheath comes out from just exchanging the roles of ions and electrons. Observe that the symmetry is not perfect because of the electron azimuthal velocity, $u_{\theta e}$, but this is constant within the sheath and does not intervene in the sheath equations.

The thin Debye sheath is collisionless and unmagnetized. Its role is to create a potential fall that adjusts the flux of the repelled species that is collected effectively at the anode to the flux that comes into the sheath from the quasineutral presheath. A kinetic formulation is mandatory for the repelled species. Making the ansatz that the sheath potential profile is monotonic, ϕ can be used as the spatial variable within the sheath. Let v_{ze} represent the velocity of individual electrons perpendicular to the anode, and $f_{ze}(v_{ze}, \phi)$ characterize the 1D electron VDF, once integral moments on the parallel velocity components have already been carried out.

Since electrons satisfy $m_e v_{ze}^2 + 2e\phi = \text{const}$ in the sheath, $f_{ze}(v_{ze}, \phi)$ depends only on the electron VDF at the sheath edge B, $f_{zeB}(v_{ze})$. This distribution must satisfy two requirements: (1) to be consistent with the particle behavior in sheath and anode, and (2) to match appropriately at the sheath edge B with the electron fluid formulation in the presheath. For instance, the usual choice of $f_{zeB}(v_{ze})$ fully Maxwellian [5, 42] is inaccurate since the anode does not return back the tail of electrons reaching it. The inaccuracy is certainly negligible when the sheath potential fall is large (i.e. $e\phi_{AB}/T_{eB} \gg 1$), but here we are mainly interested in the negative-to-positive sheath transition, that is in cases with $e\phi_{AB}/T_{eB}$ small. The drifted Maxwellian (with u_{zeB} as drift velocity) proposed in Ref. [6] is incorrect too, since $f_{zeB}(v_{ze})$ must be symmetric on v_{ze} for electrons that are reflected back within the sheath, that is for $|v_{ze}| < \sqrt{2e\phi_{AB}/m_e}$.

The correct choice, within the 'family' of Maxwellian distributions, is a zero-drift, cut-off distribution [Fig. A.1(b)]

$$f_{ze}(v_{ze}, \phi) = n_\star \sqrt{\frac{m_e}{2\pi T_\star}} \exp\left(e\frac{\phi - \phi_B}{T_\star}\right) \exp\left(-\frac{m_e v_{ze}^2}{2T_\star}\right) H\left(v_{ze} + \sqrt{\frac{2e(\phi - \phi_A)}{m_e}}\right). \tag{A.18}$$

Here, $T_\star$, $n_\star$, and ϕ_{AB} are the three parameters characterizing the VDF, and $H(v_z)$ is the Heaviside step function. The three parameters must be determined from three matching conditions at point B between the plasma formulations in sheath and presheath. The matching conditions we propose are: (1) the continuity of the electron density:

$$\int_{-\infty}^{\infty} dv_{ze} f_{zeB} \equiv n_\star \frac{1 + \operatorname{erf}(\sqrt{e\phi_{AB}/T_\star})}{2} = n_{eB}; \tag{A.19}$$

(2) the continuity of the electron flux:

$$\int_{0}^{\infty} dv_{ze} v_{ze} f_{zeA} \equiv n_\star \sqrt{\frac{T_\star}{2\pi m_e}} \exp\left(-\frac{e\phi_{AB}}{T_\star}\right) = g_{zeB}; \tag{A.20}$$

and (3) the fulfillment of the marginal Bohm condition at the sheath edge B:

$$\frac{d}{d\phi}[n_e(\phi) - n_i(\phi)]_{B^+} = 0^+, \tag{A.21}$$

with $n_e(\phi)$ and $n_i(\phi)$ the density profiles in the sheath.

The general Bohm condition, $d(n_e - n_i)/d\phi_B \geq 0$, comes out from imposing that the solution of the Poisson equation, $d^2\phi/dz^2 = e(n_e - n_i)$, departing from the quasineutral point B presents a monotonic potential [43]. The derivative of

$$n_e(\phi) = n_\star \exp\left(\frac{e\phi - e\phi_B}{T_\star}\right) \frac{1 + \operatorname{erf}(\sqrt{e[\phi - \phi_A]/T_\star})}{2} \tag{A.22}$$

is obtained easily. Then, if the fluid formulation for ions is kept inside the sheath, condition (A.21) becomes

$$\frac{n_{eB}}{T_\star} + \frac{n_\star \exp(-e\phi_{AB}/T_\star)}{2T_\star\sqrt{\pi e\phi_{AB}/T_\star}} = \frac{n_{eB}}{m_i u_{ziB}^2 - T_{iB}}. \tag{A.23}$$

Thus: Eq. (A.19) relates $n_\star$ and n_{eB}, Eq. (A.20) determines ϕ_{AB} in terms of g_{zeB}, and Eqs.(A.23) and (A.8) relate T_* and T_{eB}. As a consequence, the plasma-wall problem can be solved without having to determine the sheath profiles.

Let us check that the present model recovers the classical large sheath and provides a good-matching condition at the positive-to-negative sheath transition. For $e\phi_{AB}/T_\star \gg 1$, Eq. (A.19) and (A.23) yield $n_{eB} \simeq n_\star$ and $u_{ziB} \simeq \sqrt{(T_\star + T_{iB})/m_i}$. This last expression, together with Eq. (A.20) [which assures that $u_{zeB} \ll \sqrt{T_\star/m_e}$] and Eq. (A.8), yields $T_{eB} \simeq T_\star$. Therefore, for $e\phi_{AB}/T_{eB} \gg 1$, f_{zeB} is close to a full-Maxwellian and

$$u_{ziB} = \sqrt{\frac{T_{eB} + T_{iB}}{m_i}}, \quad u_{zeB} = \sqrt{\frac{T_{eB}}{2\pi m_e}} \exp\left(-\frac{e\phi_{AB}}{T_{eB}}\right). \tag{A.24}$$

These results change for moderate and small negative sheaths. In particular, for $e\phi_{AB}/T_\star \ll 1$, f_{zeB} tends to be a half-Maxwellian, $n_{eB} \simeq n_\star/2$, $T_{eB} \simeq 2T_\star/\pi$, and u_{ziB} and u_{zeB} approach the no-sheath values of Eq. (A.15). For positive sheaths, Eqs.(A.18)-(A.24) are applicable if subscripts i and e are exchanged, and ϕ_{AB} is substituted by $-\phi_{AB} = |\phi_{AB}|$.
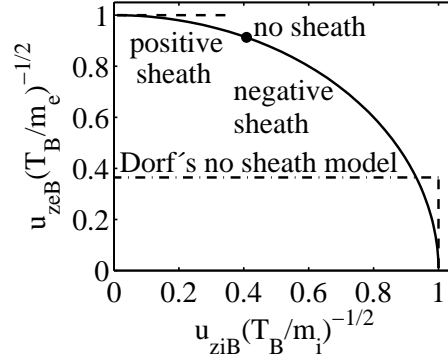
Figure A.2: Ion and electron (axial) velocities versus the i-e flux ratio at the sheath edge. The asterisk represents the transition from positive to negative sheath for $T_{iB}/T_{eB} = 0.2$. Vertical and horizontal dashed lines correspond to the large sheath approximation. The dash-and-dot line is the no-sheath model proposed by Dorf *et al.* .

The continuity of the sonic Bohm condition across the sheath edge was already invoked as a matching condition in the presheath-sheath model of Ref. [10]. There, different *macroscopic* models of a *three-species* plasma in sheath and presheath had to be matched at the sheath edge. The suitability of this matching condition here is well justified too. On the one hand, it is based on the continuity of a *physical* property, the 'sonic' character of point B (i.e. the equality between the static and dynamic pressures). On the other hand, since $\phi_{AB} \to 0$ for $u_{z\alpha B}^2 \to T_{\alpha B}/m_\alpha, (\alpha = i, e)$, it recovers *exactly* the full ranges of the positive and negative sheaths. This is not immediate to satisfy, taking into account the different plasma formulations in sheath and presheath; the models of Refs. [42] and [6] are clear examples. Also, in a previous version of this model [2] we imposed, as third matching condition, that the electron temperature obtained from the VDF [Eq. (4) of Ref. [2]] should coincide with the electron temperature in the presheath, T_{eB}. It turned out that $\phi_{AB} = 0$ for $u_{zeB}/\sqrt{T_{eB}/m_e} \approx 0.9$ so that no satisfactory solution could be found for the range $0.9 < u_{zeB}/\sqrt{T_{eB}/m_e} < 1$. To conclude, it can be said that the matching of the integral moments of f_{zeB} with the fluid formulation is exact up to order one, and only partially exact in order two. Therefore, some differences at point B between sheath and presheath values are expected in high-order plasma magnitudes that. The good news are that for the main macroscopic magnitudes the Fortunately, the differences are small for all common magnitudes. For instance, the flux of electron energy deposited at the anode (a relevant magnitude indeed) is, depending on the sheath regime,

$$Q_{zeA} = g_{zeB} \times \begin{cases} 2T_\star + \frac{1}{2}m_e u_{\theta eB}^2, & \text{for } \phi_B > \phi_A, \\ e|\phi_{AB}| + \frac{5}{2}T_{eB} + \frac{1}{2}m_e(u_{zeB}^2 + u_{\theta eB}^2), & \text{for } \phi_B < \phi_A. \end{cases} \tag{A.25}$$

One has that $Q_{zeA}/g_{zeB} - m_e u_{\theta eB}^2/2$ is equal to πT_{eB} for $\phi_{AB} \to 0^+$ and $3T_{eB}$ for $\phi_{AB} \to 0^-$, the difference being a mere 5% at the positive-to-negative sheath transition.
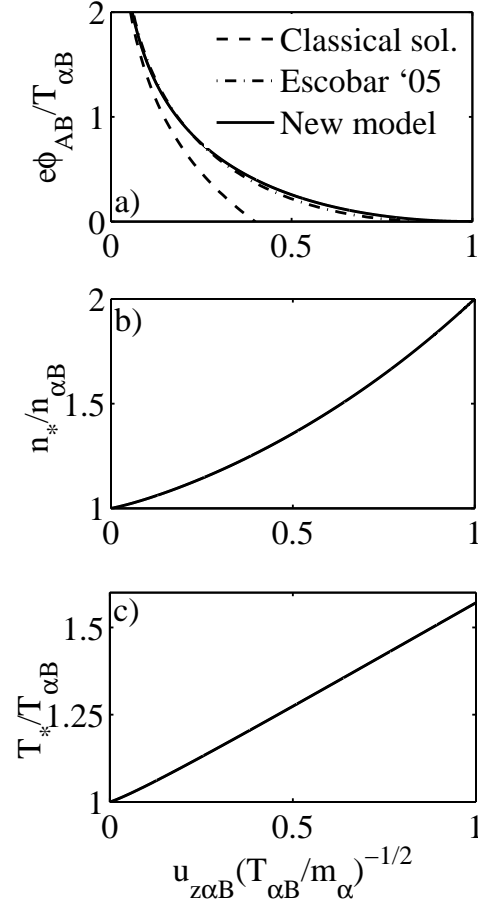
Figure A.3: (a) Sheath potential drop versus the perpendicular macroscopic velocity of the repelled species (called α). The dashed line corresponds to the standard large sheath approximation. The dash-and-dot line corresponds to the model proposed in Ref. [2]. (b)-(c) The two constants $n_\star$ and $T_\star$, defining the cut-off Maxwellian at the sheath edge, $f_{z\alpha B}$.
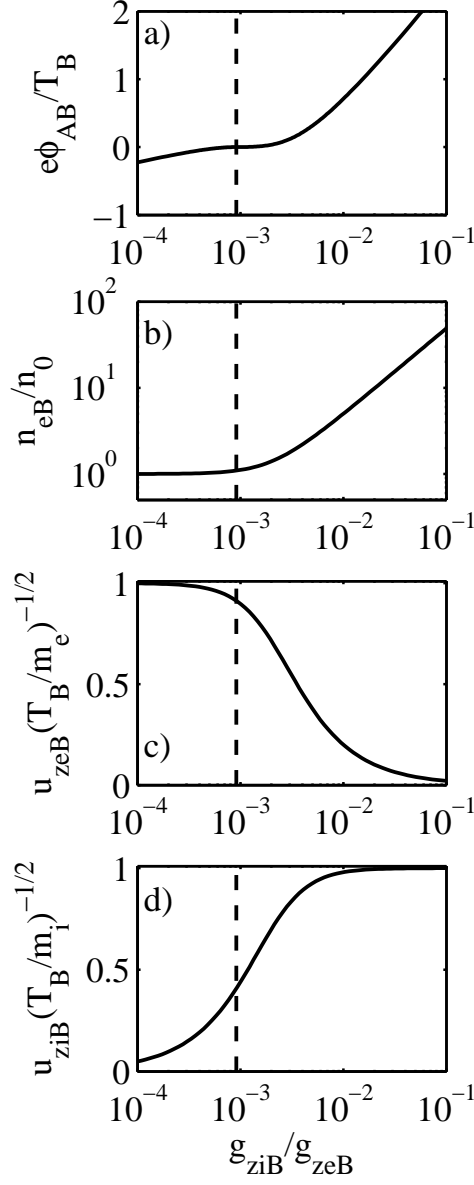
Figure A.4: Plasma parameters at the sheath edge versus the i-e flux ratio, for $T_{iB}/T_{eB} = 0.2$ and $\omega_{eB}/\nu_{eB} = 10$; origin of ϕ placed at anode, $\phi_A = 0$; $n_0 = g_{zeB}(m_e/T_B)^{-1/2}$. The dashed line marks the no sheath case.

A.4 Results

Figure A.2 plots the relative values of u_{zi} and u_{ze} at point B, Eq. (A.9), as the near-anode region evolves from presenting a negative to a positive anode fall. The dimensionless curve of Fig. A.2 is just the universal 'circle' expressed by Eq. (A.8); only the position of the no-sheath point depends on the ratio T_{iB}/T_{eB} and the type of gas, Eq. (A.15). Dashed lines represent the standard 'large sheath' approximations, Eq. (A.24), for positive and negative falls. The horizontal dash-and-dot line is the no-sheath regime proposed by Dorf *et al.* [42], as continuation of the (large) negative sheath regime.

Figure A.3(a) shows the variation of the sheath potential drop with the drift velocity of the repelled species from the 'large sheath' to the 'no sheath' cases. It can be observed that the 'large sheath' model yields already an error of a 20% for $u_{z\alpha B}/\sqrt{T_{\alpha B}/m_\alpha} \sim 0.15$. The approximate model of Ref. [2] is plotted too. Figures A.3(b)(c) depict the two other constants characterizing the cut-off Maxwellian at point B, n_* and T_* in Eq. (A.18), in terms of $n_{\alpha B}$, $T_{\alpha B}$, and the drift velocity.

Figures A.4(a)-(d) depict the evolution of plasma magnitudes at the sheath edge B with the i-e flux ratio in the anode presheath. The main features we observe are: the smooth transition of the potential fall from positive to negative sheaths; the continuous change of u_{ziB} and u_{zeB} with the anode fall; the decrease of n_{eB} as we move towards a positive sheath (if g_{zeB} is kept constant); the no influence of the local Hall parameter, ω_{eB}/ν_{eB}, on the anode fall; and the small range of values of the i-e flux ratio leading to a positive sheath. This range is proportional to the square-roots of the electron-to-ion mass ratio and the ion-to-electron local temperature ratio, Eq. (A.15). In a real Hall thruster discharge, T_{iB}/T_{eB} is expected small but T_{iB} cannot be neglected if the positive sheath regime wants to be recovered: one has $|e\phi_{AB}| \propto T_{iB}$ for a positive sheath. Also the ion velocity at the sheath edge can never be taken zero: for a large positive sheath, the small ion drift plays the same role than the small electron drift for a large negative sheath.

Figure A.5 depict profiles of plasma magnitudes in the anode presheath for different values of g_{ziB}/g_{zeB}, covering both the negative and positive sheath cases. The profiles of the electric potential present a maximum within the presheath where the ion flux satisfies $u_{zi} = \sqrt{T_{iB}/m_i}$, Eq. (A.2). As $|u_{ziB}|$ decreases from $\sqrt{T_{iB}/m_i}$ ('large sheath' limit), the maximum of $\phi(z)$ moves toward the sheath edge B and disappears eventually in the positive sheath regime.

Figure A.6 illustrates the behavior of the electron azimuthal velocity. It plots the dependence of $u_{\theta eB}$ on both the i-e flux ratio and the local Hall parameter, and some examples of spatial profiles of $u_{\theta e}$ in the anode presheath. The main observation is that, except for regime N, the azimuthal velocity differs substantially from the diffusive approximation

$$-u_{\theta e,diff} \simeq u_{ze}\frac{\omega_{eB}}{\nu_{eB}}, \tag{A.26}$$

the difference being maximum at the sheath edge and increasing as ω_{eB}/ν_{eB} increases. Ahedo and Rus [8] already found (within a model of the full Hall thruster discharge with partial inertial effects on electrons) that inertia tends to limit the increase of the azimuthal energy to values of the order of the thermal energy. The behavior of $u_{\theta e}$ in regime P is analyzed below.

The limitation of the azimuthal electron energy are good news for the heat deposited at the anode in the positive sheath regime. Figure A.7 plots the energy deposited by electrons into

the anode for negative and positive sheaths (the energy deposited by ions is much smaller in generally). The relative heath flux $Q_{zeA}/g_{zeB}T_{eB}$ ranges from the classical value of 2 for regime N to ~ 5 at the no-sheath point. Then, in regime P, since the azimuthal energy is almost invariant, the changes of the electron energy flux are due to $|e\phi_{AB}|$, which is proportional to T_{iB}.

A.4.1   On the character and extension of the presheath

The presheath profiles of Figs. A.5 and A.6 were obtained integrating from a location far from the anode, where $m_e u_{ze}^2 + m_i u_{zi}^2 \ll T_B$ and Eq. (A.26) applies. Whereas the solutions for negative and positive sheaths are equivalent (except for $u_{\theta e}$), the presheath behavior for regimes N and P presents very important differences. First, there is the small range of parameters corresponding to regime P (mainly for heavy gases). Second and more relevant, the presheath character, which is determined by the behavior of the attracted species with respect to the applied magnetic field, is totally different: regime N corresponds to an 'unmagnetized' presheath, while regime P pertains to a 'parallel-incidence, magnetized' presheath. An analytical solution for this case (and ω_{eB}/ν_{eB} large) was derived by Ahedo [44]. Appendix A recovers that solution with some improvements. The behavior of $u_{\theta e}(z)$ in regime P is given by Eq. (A.32) and differs substantially from the diffusive behavior for regime N, Eq. (A.26). From Eqs.(A.32) and (A.36), the azimuthal velocity at the sheath edge is

$$\frac{-u_{\theta eB}}{\sqrt{T_B/m_e}} \simeq \sqrt{2\ln\frac{\omega_{eB}}{\nu_{eB}} - \ln 2\pi - 1 + 2\frac{\nu_{eB}}{\omega_{eB}}}. \tag{A.27}$$

This asymptotic solution, plotted in Fig. A.6(a), shows a good agreement with the exact solution. This confirms its suitability to interpret the plasma response in regime P. For instance, it shows that the anode presheath changes from being collisional-diffusive while $u_{ze}/\sqrt{T_B/m_e} < \nu_{eB}/\omega_{eB}$ to being a free-acceleration zone near the sheath, when $u_{ze}/\sqrt{T_B/m_e} = O(1)$. Also, Eq. (A.27) confirms that the electron azimuthal energy remains of the order of the thermal energy except for $\ln(\omega_{eB}/\nu_{eB}) \gg 1$ (but this range is very unlikely in Hall thrusters, at least). Reference [44] yielded only the dominant (logarithmic) term of the right hand side of Eq. (A.27); for $\ln(\omega_{eB}/\nu_{eB})$ not very large, the contributions of the other terms is not negligible, a 27%-40% in Fig. A.6(a).

The extension of the presheath, ℓ_{ps}, also differs substantially for the unmagnetized presheath of regime N and the parallel, magnetized presheath of regime P. An immediate observation, corroborated by Fig. A.5, is that larger forces (i.e. larger gradients) are necessary to accelerate magnetically-trapped electrons in regime P than to accelerate unmagnetized ions in regime N. Figure A.8 plots the change of ℓ_{ps} and the presheath potential drop $\Delta\phi_{ps}$ with the i-e flux ratio and the local Hall parameter; these values are based on the criterion that the anode presheath extends from the sonic point B to the (arbitrary) point where $m_e u_{ze}^2 + m_i u_{zi}^2 = 0.1 T_B$. Observe that $\Delta\phi_{ps}$ is independent of the Hall parameter and has different signs for regimes N to P, as already commented. In regime P, the solution of the Appendix yields that the presheath extension scales as

$$\ell_{ps} \sim \frac{\ell_e}{\sqrt{2\ln\frac{\omega_{eB}}{\nu_{eB}}}}, \tag{A.28}$$
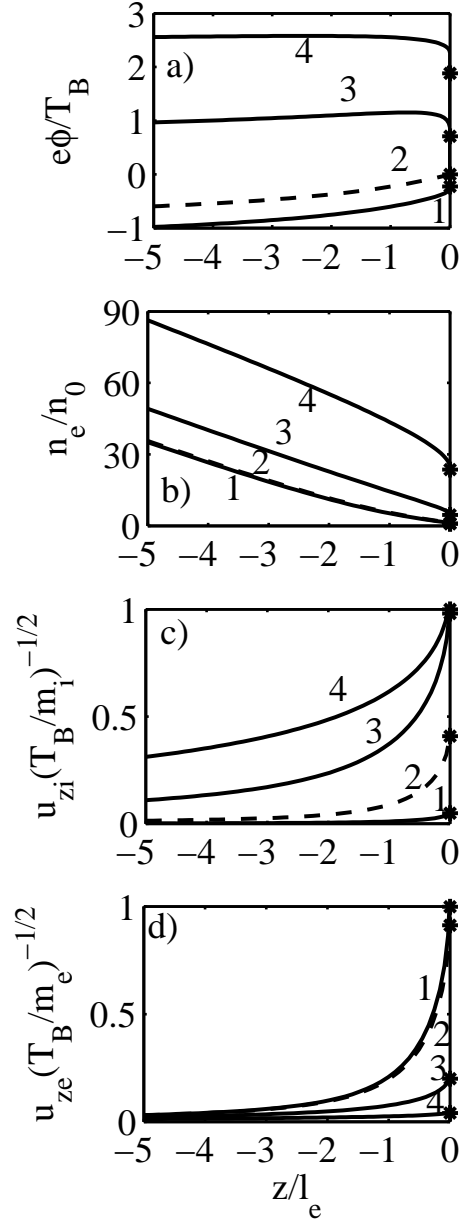
Figure A.5: Plasma profiles in the anode presheath for different values of g_{ziB}/g_{zeB} =0.0001(1), 0.00091(2), 0.01(3), and 0.05(4). Other parameters: $T_{iB}/T_{eB} = 0.2$ and $\omega_{eB}/\nu_{eB} = 10$. Dashed lines (3) represent the no-sheath case. The anode sheath is seen here as a surface discontinuity, black points indicating values at the sheath edge B.
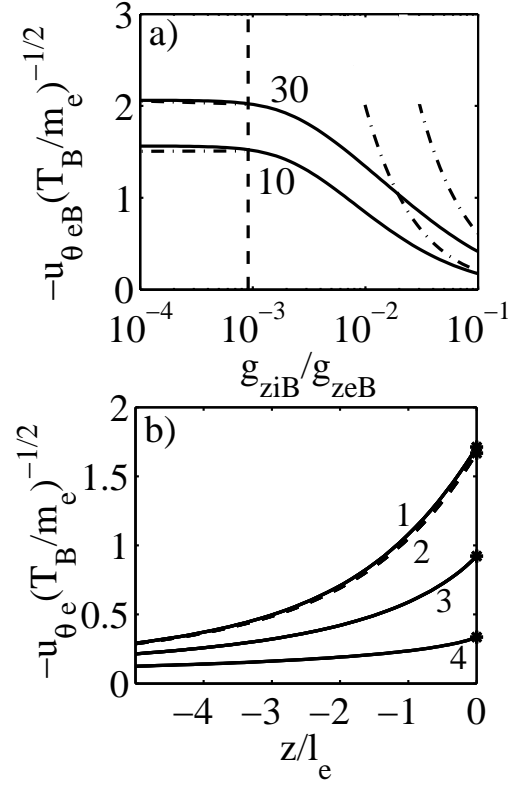
Figure A.6: (a) Electron azimuthal velocity at the sheath edge versus the i-e flux ratio for $\omega_{eB}/\nu_{eB} = 10$ and 30; other parameters as in Fig. A.5. The dashed line marks the no sheath case. The dashed-and-dot lines correspond to the diffusive approximation, Eq. (A.26), in regime N, and to Eq. (A.27) in regime P. (b) Profile of the electron azimuthal velocity in the anode presheath for the same cases than in Fig. A.5.
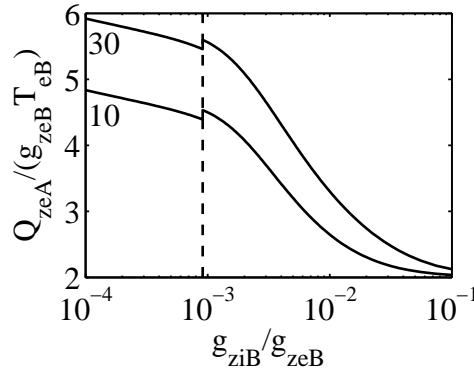
Figure A.7: Energy deposited by electrons at the anode versus the i-e flux ratio, for for $\omega_{eB}/\nu_{eB} = 10$ and 30; other parameters as in Fig. A.5. The dashed line marks the no sheath case.
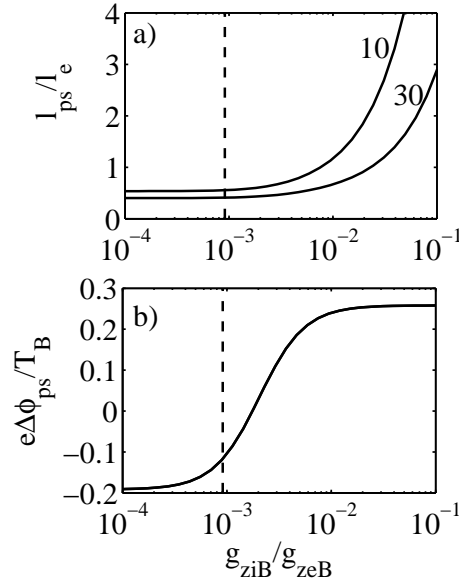
Figure A.8: Length and potential drop of the anode presheath versus the i-e flux ratio for $\omega_{eB}/\nu_{eB} = 10$ and 30. The presheath is considered to extend between point B and the point where $m_e u_{ze}^2 + m_i u_{zi}^2 = 0.1 T_B$.

with ℓ_e the standard electron gyroradius. Equation (A.28) explains the small dependence with the Hall parameter observed in Fig. A.8. In regime N, where the diffusive limit holds, Eq. (A.7) becomes

$$\left(\frac{T_B}{m_i u_{zi}^2} - 1\right) \frac{du_{zi}}{dz} \simeq \frac{\omega_{eB}^2 + \nu_{eB}^2}{\nu_{eB}} \frac{m_e g_{zeB}}{m_i g_{ziB}} \tag{A.29}$$

and the presheath extension is

$$\ell_{ps} \sim \sqrt{\frac{T_B}{m_i}} \frac{\nu_{eB}}{\omega_{eB}^2 + \nu_{eB}^2} \frac{m_i g_{ziB}}{m_e g_{zeB}}, \tag{A.30}$$

which scales linearly with the i-e flux ratio, Fig. A.8(b).

A.5 Discussion

We have presented a model of the near-anode region of a Hall thruster that shows a gentle, continuous, parametric transition between negative and positive sheath regimes. A central result is the non-existence of a no-sheath regime but just a single no-sheath case. Fundamental elements of the model are (1) to include full inertia terms in the fluid equations of ions and electrons, (2) to opt for a cut-off Maxwellian distribution of the repelled species in the sheath, and (3) the use of the (generalized) Bohm sonic condition as the last matching condition between the sheath and presheath formulations. Classical solutions for large negative and positive sheaths (with classical Bohm conditions) are recovered asymptotically. The regime adopted by the plasma depends on the relative flux of ions and electrons reaching the near-anode region. The parametric range for positive sheaths is much smaller because of the small

electron-to-ion mass ratio. The present model model is of interest to any device or problem where large variations of the electron and ion fluxes are likely.

The study has been focused in situations where the local Hall parameter is not small, and the $\boldsymbol{E} \times \boldsymbol{B}$ drift (i.e. azimuthal drift in Hall thrusters) dominates electron dynamics. Then, it has been shown that the diffusive approximation for the azimuthal-to-axial electron drift applies only in the large, negative sheath regime. For the positive sheath regime, the azimuthal electron energy remains of the order of the electron thermal energy, which limits the increase of the electron energy deposited at the anode. Also in the positive sheath regime, the anode presheath has a strongly-magnetized, parallel-incidence character, which reduces greatly the presheath extension (to the order of the electron gyroradius, roughly). The case of a small Hall parameter in the near-anode region has not been discussed in detail here, since it is simpler and straightforward from the present analysis.

The scope of the present model is limited to the near-anode region. Therefore, it can teach nothing about how the main parameters governing the Hall thruster discharge (i.e. magnetic field topology, discharge voltage, mass flow rate) influence the plasma response in the near-anode region. In particular, the coupling of this region with the rest of the channel would yield how the operation parameters determine the i-e flux ratio near the anode and, as a consequence, the near-anode regime. From existing models of the full discharge, strictly valid for non-small negative sheaths only, the i-e flux ratio is known to decrease when[45, 46]: the discharge voltage is decreased, or the magnetic field is increased, or the magnetic field shape is more flat, or the turbulent diffusion decreases. This last case would agree with the assertion of Ref. [41] that the turbulent diffusion is lower for the magnetic field configuration yielding a positive anode fall.

A model of the full Hall thruster discharge which includes all electron inertia terms (and, therefore, the negative-to-positive transition) faces numerical difficulties that have not been solved yet, even in the one-dimensional formulation. Furthermore, in the two-dimensional case, the region near the anode becomes much more complex since fluxes are not uniform and the magnetic field impinges obliquely on the anode and connects it with the lateral dielectric walls.

Appendix: presheath solution for large positive sheaths

In regime P, the ion drift energy can be dropped from Eq. (A.7), yielding

$$\left(u_{ze} - \frac{T_B}{m_e u_{ze}} \right) \frac{du_{ze}}{dz} = \omega_{eB} u_{\theta e} - \nu_{eB} u_{ze}, \tag{A.31}$$

which is solved together with Eq. (A.4). These lead to the first-integral

$$-u_{\theta e} = \frac{\nu_{eB}}{\omega_{eB}} \left(u_{ze} + \frac{T_B}{m_e u_{ze}} \right) + \frac{\nu_{eB}^2 + \omega_{eB}^2}{\omega_{eB}} (z - z_0) \tag{A.32}$$

(z_0 is a constant) which yields $u_{\theta e}$ explicitly; the last term of the right-hand-side is going to dominate for ω_{eB}/ν_{eB} large. Equation (A.32) is to be compared with the diffusive approximation, Eq. (A.26), for regime N.

Substituting Eq. (A.32) in Eq. (A.31), one has

$$\left(\tilde{u}_{ze} - \frac{1}{\tilde{u}_{ze}} \right) \frac{d\tilde{u}_{ze}}{d\tilde{z}} = -\tilde{\nu}_{eB} \left(2\tilde{u}_{ze} + \frac{1}{\tilde{u}_{ze}} \right) - \tilde{z}, \tag{A.33}$$

where the dimensionless variables are

$$\tilde{u}_{ze} = \frac{u_{ze}}{\sqrt{T_B/m_i}}, \quad \tilde{\nu}_{eB} = \frac{\nu_{eB}}{\sqrt{\nu_{eB}^2 + \omega_{eB}^2}}, \quad \tilde{z} = (z - z_0)\sqrt{\frac{m_i(\nu_{eB}^2 + \omega_{eB}^2)}{T_B}}. \tag{A.34}$$

If the Hall parameter is large, i.e. $\tilde{\nu}_{eB} \ll 1$, an approximate analytical solution of Eq. (A.33) is available for the whole range $0 < \tilde{u}_{ze} \leq 1$: for $\tilde{u}_{ze} \ll 1$, the solution is

$$\tilde{u}_{ze}(\tilde{z}) \simeq \tilde{\nu}_{eB}\sqrt{\frac{\pi}{2}} \exp\frac{\tilde{z}^2}{2}\mathrm{erfc}\left(-\frac{\tilde{z}}{\sqrt{2}}\right); \tag{A.35}$$

and, for $\tilde{u}_{ze} = O(1)$, the solution is

$$\frac{\tilde{u}_{ze}^2}{2} - \ln\tilde{u}_{ze} + \frac{\tilde{z}^2}{2} \simeq -\ln(\tilde{\nu}_{eB}\sqrt{2\pi}), \tag{A.36}$$

where the constant in the right hand side has been determined by matching Eqs. (A.35) and (A.36) in the overlapping region $\tilde{\nu}_{eB} \ll \tilde{u}_{ze} \ll 1$, where both solutions are valid.

Setting $\tilde{u}_{ze} = 1$, Eq. (A.36) yields

$$\tilde{z}_B \simeq \sqrt{2\ln\tilde{\nu}_{eB}^{-1} - \ln(2\pi) - 1}, \tag{A.37}$$

which determines z_0 and completes the solution.

Appendix B

PLASMA-WALL MODEL FOR PARTIAL THERMALIZATION

This annex has been published as a paper entitled 'Combined effects of electron partial thermalization and secondary emission in Hall thruster discharges' in Physics of Plasmas (vol. 14, 083501, 2007).

B.1   Introduction

The plasma interaction with the lateral dielectric walls of a Hall thruster chamber leads to plasma recombination, deposition of ion and electron energy, and deposition of electron azimuthal momentum (known as 'wall collisionality') [37, 47, 21]. These plasma depositions affect significantly the thruster performances. In addition, ion impacts on the walls are responsible for wall erosion, which, at the end, limits the thruster lifetime. An accurate model of the plasma wall interaction is one of the main open problems in Hall thruster research. The electron velocity distribution function (EVDF) and the characteristics of the secondary electron emission (SEE) from the wall are two key aspects of this problem.

Hobbs and Wesson [9], assuming a Maxwellian EVDF and cold SEE, showed that, as the SEE yield increases, the potential fall at the Debye sheaths around the dielectric walls decreases and the electron energy deposition increases. For a SEE yield close to 1 ($\sim 98.3\%$ for xenon), they found that the negative (i.e. electron-repelling) sheath reaches the charge-saturation limit(CSL) and regime, which prevent the vanishing of the negative sheath and place an upper-bound on the deposition of electron energy at the walls. Ahedo and coworkers applied the Hobbs-Wesson sheath model to macroscopic and hybrid two-dimensional(2D) models of the Hall thruster discharge, and found out that it yields excessive energy losses and, consequently, unreasonably strong deterioration of thruster performances [21, 10, 3, 48].

Recent works suggest that the plasma is not collisional enough to replenish the tail of high-energy electrons that impact the wall, so that the distribution function of bulk electrons is non-Maxwellian, thus presenting a smaller 'effective' temperature in the direction parallel to the magnetic field [49, 33, 26, 34, 50, 51]. Since the role of an electron-repelling sheath next to a dielectric wall is to balance the electron and ion fluxes, a partially-depleted tail of the EVDF reduces certainly the sheath potential fall. However, the effects of a depleted tail on the ion

flux itself and the energy losses, the two main magnitudes of plasma-wall interaction, need to be quantified. In addition, these magnitudes are also affected by the amount and behavior of the SEE.

Turning now to the characterization of the SEE, there are three subjects that require attention: (1) a correct secondary electron emission model; (2) the trapping and thermalization of the SEE beams within the bulk of the plasma; and (3) the magnetic effects on the SEE. Both the SEE yield and the energy distribution of emitted electrons are poorly known for the low energy range of electrons impacting with Hall thruster walls. SEE seems to be constituted by slow or 'true-secondary' electrons (coming from internal layers of the wall) plus elastically and inelastically reflected electrons, with different average energies and emission yields [52, 53, 54, 55]. At low impacting energies, elastically reflected electrons dominate, with an emission yield of about 20-60%. The one-parameter SEE model of Hobbs-Wesson considers cold true-secondary electrons only. In a model of the full discharge, Barral et al. [26] took into account SEE with true-secondary electrons and a constant yield of reflected electrons with partial energy accommodation; no parametric investigation was carried out. Taccogna et al. have proposed a very detailed, multi(> 10)-parameter SEE model [55]. Here, we will investigate the relevance of different parameters characterizing SEE, in order to propose a relative simple model that retains the main ones only. The charge saturation limit will be studied too.

Fife[16] and Ahedo[10] assumed total thermalization of the SEE beams within the main plasma. This justified the use of a single, Maxwellian electron population in the quasineutral plasma, even for high SEE. Later, Ahedo and Parra [35] pointed out that weak collisionality could allow to partial recollection of the SEE beams by the walls, and demonstrated that, when the recollected fraction is large, the sheaths do not reach charge-saturation and electron energy losses to the walls are much lower. Indeed the losses are similar to the zero SEE limit, i.e. about 100 times lower than for total thermalization and a charge-saturated sheath. Sydorenko et al.[51, 56] recover this behavior of SEE at low thermalization with a particle-based model.

Magnetic effects on true-secondary electrons have been considered partially by Sydorenko et al. too. They included the effect of the $E \times B$ (azimuthal) drift imparted to beam electrons once they leave the (thin) emission sheath, and pointed out that, in the weakly-collisional case, this increment of energy facilitates the partial recollection of SEE and increases the re-emission yield.

The goals of this paper are (1) to derive an quasi-analytical model of plasma-wall interaction that takes into account the combined effects of partial depletion of the main electron population and partial recollection of the SEE beams, and (2) to investigate which are the main SEE characteristics that must be retained in a SEE analytical model. Emphasis will be put on (a) comparing the low and high thermalization limits, (b) evaluating the different roles of secondary and primary electrons in the response, (c) the sensitivity of CSL conditions to different parameters, and (d) deriving simple expressions for particle and energy losses, which can be implemented in full models of the plasma discharge, such as HPHall[3, 16]. Progresses on this work were presented in two conference papers [57, 58].

As in similar works, the analysis of the collisional processes determining the state of the EVDF remains out of this paper scope. The approximate expressions used for the EVDF *within the sheaths* will be based on first-principles models. Magnetic effects on the SEE will not be included in the present model. Strictly, this limits the model validity to (i) magnetic lines perpendicular to the wall and (ii) a weak enough axial (i.e parallel to the wall) electric

field, E_z. Although there are uncertainties on the value of the azimuthal velocity, $u_\theta \sim E_z/B$, (which is measured indirectly only) experiments and simulations would suggest that, in most Hall thrusters, $m_e u_\theta^2 \ll 3T_e$, except in a very localized zone at the center of the acceleration region, where E_z is maximum.

B.2 Formulation of the electron model

A stationary plasma, confined between two planar, ceramic walls is considered (Fig.B.1). A one-dimensional model is proposed (which corresponds to the radial direction in a Hall thruster chamber); when necessary, axial plasma contributions are included as source terms. The zero Debye length limit is invoked, leading to a two-scale structure, consisting of the bulk region of quasineutral *plasma* and two collisionless, space-charge *sheaths* adjacent to the walls. Let point M be the channel median, points W and W' the two walls and points Q and Q' the edges of the two sheaths. The sheaths are semi-infinite regions in their natural scale (the Debye length) and discontinuity surfaces in the quasineutral scale (so that $r_Q = r_W = h/2$ and $r_{Q'} = r_{W'} = -h/2$). We consider only sheaths with monotonic potentials, which means that the model will not go beyond the CSL. Then, the electric potential ϕ, instead of r, can be used as the independent variable inside the sheath (thus avoiding to define a different spatial variable for the sheath). Let $\phi_{WQ} = \phi_Q - \phi_W$ be the potential drop in the sheath, which is part of the solution if the walls are dielectric. In order to neglect all magnetic effects in the model, we assume that the magnetic field $\boldsymbol{B}$ is radial and near-uniform, and the azimuthal drift velocity, u_θ, is much smaller than the electron thermal velocity, $c_e = \sqrt{T_e/m_e}$.

The velocity of each electron is divided into components parallel and perpendicular to $\boldsymbol{1}_r$, $\boldsymbol{v} = v_r \boldsymbol{1}_r + v_\perp, \boldsymbol{1}_\perp$ and the electron distribution function has the functional form $f(r, v_r, v_\perp)$. The symmetry of the problem with respect to the median M implies that

$$f(r_M + \Delta r, v_r, v_\perp) = f(r_M - \Delta r, -v_r, v_\perp). \tag{B.1}$$

B.2.1 The electron distribution function

The EVDF $f(r, \boldsymbol{v})$ is obtained from the one-dimensional (radial) Boltzmann equation

$$v_r \frac{\partial f}{\partial r} + \frac{e}{m_e} \frac{d\phi}{dr} \frac{\partial f}{\partial v_r} = \dot{f}(r, \boldsymbol{v}), \tag{B.2}$$

where $\dot{f}$ accounts for collisional processes (e-e thermalization, e-n elastic collisions, ionization), the effect of plasma instabilities, and transverse (i.e. axial) plasma diffusion (required anyway to balance the net production or loss of plasma).

In the zero Debye length limit, $\dot{f}$ can be dropped within the two thin sheaths and the EVDF depends only of the constants of motion. These consist of the the parallel and perpendicular components of the electron total energy:

$$v_\perp = \text{const}, \quad m_e v_r^2/2 - e\phi = \text{const}. \tag{B.3}$$

Therefore, the EVDF in the sheath has the functional form

$$f(\phi, v_r, v_\perp) = f_Q(v_{rQ}(\phi, v_r), v_\perp) \equiv f_W(v_{rW}(\phi, v_r), v_\perp), \tag{B.4}$$

(a)

(b)
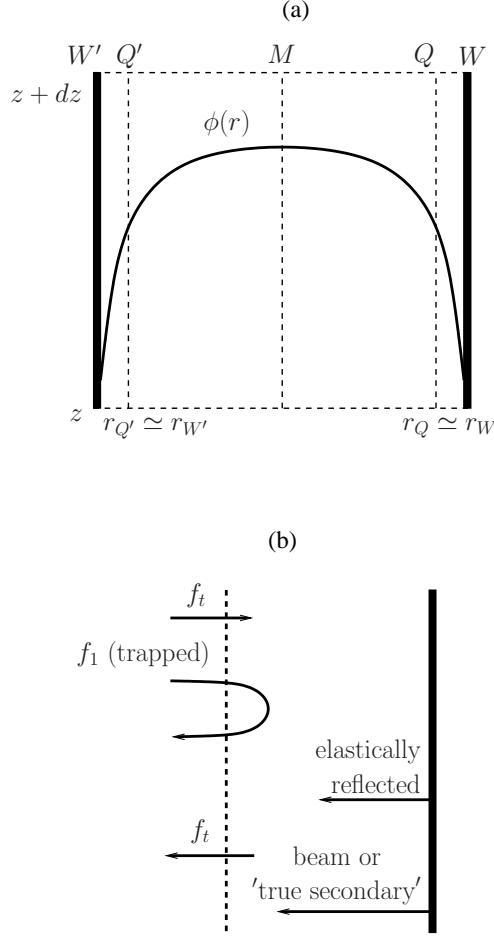
Figure B.1: (a) Sketch of the radial model with the bulk region and the two Debye sheaths. (b) Electron populations in the sheath and secondary electron emission.

where ϕ is used as independent variable,

$$v_{rQ}(\phi, v_r) = \text{sign}(v_r)\sqrt{v_r^2 + 2e(\phi_Q - \phi)/m_e}, \tag{B.5}$$

and $v_{rW}(\phi, v_r)$ satisfies a similar expression. Then, we just need to determine $f_Q(\boldsymbol{v})$ or $f_W(\boldsymbol{v})$ to know the EVDF in the sheath.

A consistent determination of the EVDF inside the sheath requires solving the Boltzmann equation in the bulk quasineutral region. Even using the simple Bhatnagar-Gross-Krook formulation [59] for $\dot{f}$, the problem faces two big difficulties: first, the quasineutrality condition implies that the potential profile $\phi(r)$ is part of the solution, and second, $\dot{f}$ depends on velocity moments of $f(r, \boldsymbol{v})$. Based on phenomenological considerations and the simple analysis carried out in Ref. [57], we assume that the distribution function at the sheath edge Q can be expressed as

$$f_Q(v_r, v_\perp) = \begin{cases} f_{fQ}(v_r, v_\perp), & v_r < -v_{WQ}, \\ f_1(v), & |v_r| < v_{WQ}, \\ f_{tQ}(v_r, v_\perp), & v_r > v_{WQ}, \end{cases} \tag{B.6}$$

where $v_{WQ} = \sqrt{2e\phi_{WQ}/m_i}$, f_{tQ} corresponds to electrons impinging into the wall W, f_{fQ} corresponds to electrons emitted or reflected at wall W, and f_1 corresponds to the population of primary (or bulk or thermalized) electrons. The population f_f of electrons *from* the wall depends on the SEE properties of wall W and will be discussed below. A Maxwellian function is used to define the primary population,

$$f_1(v) = n_1 \left(\frac{m_e}{2\pi T_1}\right)^{3/2} \exp\left(-\frac{m_e v^2}{2T_1}\right), \tag{B.7}$$

where n_1 and T_1 are constants (notice that the actual distribution function of primary electrons is determined below). The population at Q of electrons going *to* the wall satisfies

$$f_{tQ}(v_r, v_\perp) = (1-\sigma)f_{fQ'}(v_r, v_\perp) + \sigma f_1(v), \tag{B.8}$$

where the first term in the right-hand side is the non-thermalized fraction at Q of electrons coming from wall W', the second term corresponds to primary electrons, and

$$\sigma(\boldsymbol{v}) = 1 - \exp[-h/\lambda_{ther}(\boldsymbol{v})] \tag{B.9}$$

is the function representing the thermalization fraction, that depends on the thermalization mean-free-path, $\lambda_{ther}(\boldsymbol{v})$, and the channel width h. In the absence of a reliable model for the electron thermalization, we take $\sigma(\boldsymbol{v}) = $ const as in Ref. [51].

Secondary electron emission at wall W depends on the distribution of electrons impacting the wall,

$$f_{tW}(v_r, v_\perp) = \sigma e^{-\hat{\phi}_{WQ}} f_1(v) H(v_r) + (1-\sigma) f_{fW'}(v_r, v_\perp); \tag{B.10}$$

here, Eqs.(B.4) and (B.8) have been used, $\hat{\phi}_{WQ} = e\phi_{WQ}/T_1$, and $H(v_r)$ is the Heaviside step function. For the purposes of the present work, only the main aspects of the experimental data on SEE are modelled. Thus, the SEE yield is assumed to have contributions of elastically reflected electrons and 'true-secondary' or beam electrons,

$$\delta_s(E) = \delta_{sb}(E) + \delta_{sr}(E), \tag{B.11}$$

with $E = mv^2/2$ the energy of the impacting electron. Subscripts r and b stand for 'reflected' and 'beam', with the last name justified on their emission energy ($\sim 1 - 3$ eV) being generally much less than the sheath potential fall and the temperature of primary electrons ($\sim 5 - 50$ eV). Based on experimental data [52, 53, 60, 61] and previous models [26, 55, 62], the partial SEE yields are assumed to follow the simple linear laws

$$\delta_{sb} = E/E_b, \quad \delta_{sr} = \delta_0 \exp(-E/E_r); \tag{B.12}$$

in particular, the exponentially-decaying law for $\delta_{sr}(E)$ is suggested by results from Refs. [52, 53, 55]. A constant value for δ_{sr} was used by Barral et al. [26]. A possible small threshold energy (of few eV) in δ_{sb} has been neglected because of its small impact on the response. Typical values for Boron Nitride ceramics, used in Hall thrusters, would be $E_r \sim E_b \sim 50$eV and $\delta_0 \sim 0.4-0.6$, $E_b \sim 40$eV. Notice that the cross-over energy for the total SEE yield, E_1, comes out from

$$E_1 = [1 - \delta_{sr}(E_1)]E_b. \tag{B.13}$$

The distribution of electrons from wall W is modelled as

$$f_{fW}(v_r, v_\perp) = \delta_{sr}(E)f_{tW}(-v_r, v_\perp) + f_2(v)H(-v_r), \tag{B.14}$$

where the first term in the right-hand side corresponds to reflected electrons and

$$f_2(v) = g_2 \sqrt{\frac{2\pi m_e}{T_2}} \left(\frac{m_e}{2\pi T_2}\right)^{3/2} \exp\left(-\frac{m_e v^2}{2T_2}\right) \tag{B.15}$$

models the distribution of emitted beam electrons, with

$$g_2 = \int d^3 v v_r \delta_{sb}(E)[1 - \delta_{sr}(E)]f_{tW}(v_r, v_\perp) \tag{B.16}$$

representing their particle flux. Obviously, only electrons collected by the wall can produce true-secondary emission. The emission temperature $T_2(\sim 1 - 3\text{eV})$ is the fourth parameter of the SEE model, and, as commented before, T_2/T_1 is small in most or all the thruster chamber.

The populations of electrons to and from the wall, Eqs.(B.10) and (B.14), can now be expressed as linear combinations of distributions f_1 and f_2,

$$f_{tW}(v_r, v_\perp) = \left[\sigma e^{-\hat{\phi}_{WQ}} f_1(v) + (1 - \sigma)f_2(v)\right]\kappa H(v_r), \tag{B.17}$$

$$f_{fW}(v_r, v_\perp) = \left[\delta_{sr}\sigma e^{-\hat{\phi}_{WQ}} f_1(v) + f_2(v)\right]\kappa H(-v_r). \tag{B.18}$$

Here

$$\kappa(\delta_{sr}, \sigma) = \frac{1}{1 - (1 - \sigma)\delta_{sr}} \tag{B.19}$$

is a gain factor representing the cumulative effect of the subsequent collisions of reflected electrons with the walls, Fig.B.2. The two contributions to f_{tW} in Eq.(B.17) are the replenished tail of primary electrons, and the total number of beam electrons. Since one has $\sigma\kappa < 1$ for $\sigma < 1$ and $\forall\delta_{sr}$, partial thermalization always implies a partial depletion of the incident tail of primary electrons. On the contrary, $(1 - \sigma)\kappa$ can be larger than one (in particular, for $\sigma \ll 1$ and $\delta_{sr} > 0$).

We can now express the electron distribution function at any location inside the sheath (defined by its local potential ϕ) as the sum of the contributions of the distributions of primary and beam electrons,

$$f(\phi, \boldsymbol{v}) = f_p(\phi, \boldsymbol{v}) + f_b(\phi, \boldsymbol{v}), \tag{B.20}$$

with

$$f_p(\phi, v_r, v_\perp) = f_1(v)e^{e(\phi-\phi_Q)/T_1} \times \begin{cases} \delta_{sr}\sigma\kappa, & v_r < -v_{r0}, \\ 1, & |v_r| < v_{r0}, \\ \sigma\kappa, & v_r > v_{r0}, \end{cases} \tag{B.21}$$

$$f_s(\phi, v_r, v_\perp) = f_2(v)e^{e(\phi-\phi_W)/T_2} \times \begin{cases} \kappa, & v_r < -v_{r0}, \\ 0, & |v_r| < v_{r0}, \\ (1 - \sigma)\kappa, & v_r > v_{r0}, \end{cases} \tag{B.22}$$

where $v_{r0} = \sqrt{2e(\phi - \phi_W)/m_e}$.
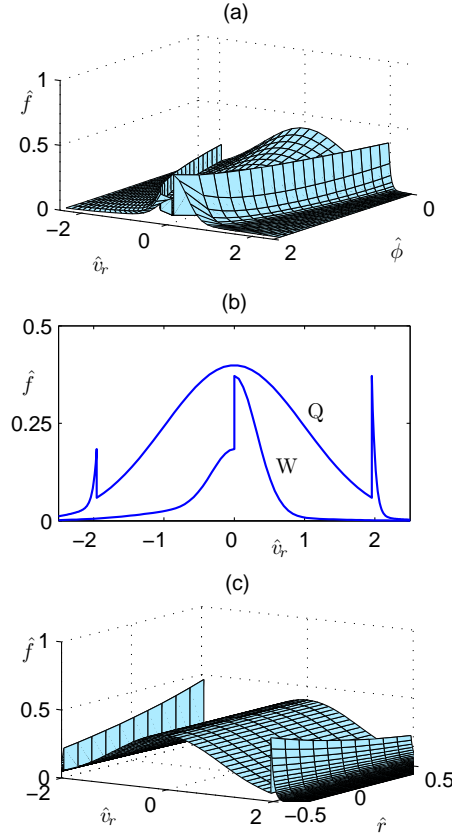
Figure B.2: (a) Evolution of the distribution function in the sheaths for $\sigma = 0.6$, $T_2/T_1 = 0.1$, $\delta_{sr} = 0.25$, $E_b/T_1 = 1.5$, and $\hat{\phi}_{WQ} = 1.91$. Dimensionless variables are $\hat{r} = r/h$, $\hat{v} = v_r \sqrt{m_e/T_1}$, and $\hat{f}(r,v_r) = n_1^{-1} \sqrt{T_1/m_e} \int_0^\infty dv_\perp 2\pi v_\perp f(r,v_r,v_\perp)$. Regions $v_r < 0$ and $v_r > 0$ correspond to distributions f_f and f_t, respectively, of electrons from wall and to wall. (b) Comparison of the EVDF at the two sheath ends, Q and W. (c) Illustration of the evolution of the distribution function in the bulk region (for $\phi = $ const)

B.2.2 Fluxes of particles and energy

The fluxes of particles and energy at the wall satisfy

$$g_e = \int d^3v v_r f_W(v_r, v_\perp), \tag{B.23}$$

$$q_{eW} = \int d^3v v_r \frac{1}{2} m v^2 f_W(v_r, v_\perp). \tag{B.24}$$

Notice that particle fluxes are constant across the sheath but energy fluxes are not; at the sheath edge: $q_{eQ} = q_{eW} + \phi_{WQ} g_e$.

Because of the presence of δ_{sr} in function κ, the above integrals cannot be expressed in a simple non-integral form except for $\delta_{sr}(E) = $ const (i.e. $E - r = \infty$) or $\sigma = 1$. We solve

next the problem for $\delta_{sr} =$ const and postpone the more general case to Sec. IV.B. Using Eqs. (B.17) and (B.18), one has

$$g_e = g_p - g_b, \qquad q_{eW} = 2T_1 g_p - 2T_2 g_b, \tag{B.25}$$

with

$$g_p = (1 - \delta_{sr})\sigma\kappa e^{-\hat{\phi}_{WQ}} n_1 \sqrt{T_1/2\pi m_e}, \qquad g_b = \sigma\kappa g_2, \tag{B.26}$$

the *net* fluxes or primary and beam electrons, respectively. Notice that g_2, Eq.(B.16), is only the flux of 'new' beam electrons; g_2 and g_b coincides only for total thermalization, $\sigma = 1$.

For $\delta_{sb}(E)$ linear, this flux of emitted beam electrons, satisfies

$$g_2 = (1 - \delta_{sr})q_{tW}/E_b, \tag{B.27}$$

where

$$q_{tW} = \frac{g_p}{1 - \delta_{sr}}\frac{2T_1}{E_b} + \kappa(1 - \sigma)\frac{2T_2}{E_b}g_2, \tag{B.28}$$

is the energy flux incident into the wall. Solving Eq.(B.27) for g_2, the net beam (or 'true-secondary') yield (defined as the ratio between beam and primary net fluxes) is

$$\frac{g_b}{g_p} \equiv \gamma_{bp} = \sigma\kappa\gamma_{2p}, \qquad \gamma_{2p} = \frac{2T_1}{E_b - \kappa(1 - \sigma)(1 - \delta_{sr})2T_2}, \tag{B.29}$$

where $\gamma_{2p} \equiv g_2/g_p$ is the average emission yield of true-secondary electrons.

Appendix A gives expressions for other magnitudes of interest, such as the partial densities of primary and beam electrons, n_p and n_b, respectively, and the temperature, T_{rpQ}, of primary electrons, in the direction parallel to the magnetic field (it is immediate that the perpendicular temperature of primary electrons is T_1).

B.3   Closure of the sheath model

The parameters involved in the EVDF model can be divided in several groups. The first one consists of the type of gas, which defines the ratio $\sqrt{m_i/m_e}$, and the reference values n_1, T_1. These are used to define non-dimensional variables:

$$\hat{n} = \frac{n}{n_1}, \quad \hat{g} = \frac{g}{n_1\sqrt{T_1/m_i}}, \quad \hat{T} = \frac{T}{T_1}, \quad \hat{\phi} = \frac{e\phi}{T_1}, \tag{B.30}$$

and so on. The second group consists of the thermalization factor σ and the four parameters of the SEE model: T_2, E_b, E_r, and δ_0. Finally, there is the sheath potential fall ϕ_{WQ}.

If the potential fall is known (for a conducting wall, for instance) the model of Sec. II would be complete in order to determine the EVDF and the electron-wall interaction. Figures B.2(a)-(b) plot an example of the evolution of the EVDF inside a sheath, with ϕ acting as spatial variable. Figure B.2(b) compares the EVDF at the two sheath ends; beam electrons and the partially depleted tail of primary electrons are clearly observable in f_Q. Figure B.2(c) has illustrative purposes only: it shows the profiles of the EVDF in the bulk of the plasma for constant electric potential there. Observe the two counterstreaming beams of secondary electrons and their partial thermalization.

For dielectric walls, the potential fall $\hat{\phi}_{WQ}$ is determined from the condition of zero electric current at the wall,

$$g_e = g_i \equiv j_{iW}/e, \tag{B.31}$$

with j_{iW} the ion density current into sheath and wall. This condition couples the ion and electron problems. Since j_{iW} is going to depend weakly on σ and the SEE model, it is convenient to rewrite the expressions of Eq. (B.25) in the form

$$g_p = \frac{g_i}{1 - \gamma_{bp}}, \qquad q_{eW} = \frac{2T_1 - 2T_2\gamma_{bp}}{1 - \gamma_{bp}} g_i. \tag{B.32}$$

Substituting g_p in the first equation with Eq.(B.26) and solving for the sheath potential one has

$$\exp \hat{\phi}_{WQ} = \sqrt{\frac{m_i}{2\pi m_e}} \frac{\sigma\kappa}{\hat{g}_i}(1 - \delta_{sr})(1 - \gamma_{bp}). \tag{B.33}$$

The ion current at the sheath edge depends on the plasma behavior in the bulk region. As an example and in order to close the model, we determine next j_{iW} for the simplest case of a stationary regime and singly-charged, quasi-cold ions.

B.3.1   A simple ion model

In a stationary regime, the ion current into the sheath is determined self-consistently from the Bohm condition at the sheath edge. The Poisson equation for the sheath potential is

$$\frac{d^2\phi}{dr^2} = \frac{e}{\epsilon_0} \left[n_e(\phi) - n_i(\phi) \right], \tag{B.34}$$

where the ion and electron densities depend only on ϕ. It is well known that the development of a space-charge, monotonic solution from point Q^+ (on the sheath side) requires to satisfy the generic Bohm condition

$$\frac{d}{d\phi} \left[n_e(\phi) - n_i(\phi) \right]_{Q^+} \geq 0. \tag{B.35}$$

Furthermore, if the response is stationary in the quasineutral region, only the marginal (or sonic) form of the Bohm condition applies.

The density of a quasi-cold, singly-charged ion population satisfies

$$n_i(\phi) = g_i \left[(g_i/n_{eQ})^2 + 2e(\phi_Q - \phi)/m_i \right]^{-1/2}, \tag{B.36}$$

where quasineutrality at Q has been applied. Then, the marginal case of Eq.(B.35) leads to

$$g_i = n_{eQ}u_{riQ}, \qquad u_{riQ} = \sqrt{\frac{en_{eQ}}{m_i} \frac{d\phi}{dn_e}\bigg|_{Q^+}}, \tag{B.37}$$

which is further developed in Eq.(B.49) of the Appendix. This expression states that, for a cold ion population, g_i depends only on the electron density around Q. For the simple case of zero SEE and a non-depleted Maxwellian distribution, the Bohm condition states that ions enter the sheath with the sound velocity $\sqrt{T_1/m_i}$.

B.3.2   The charge saturation limit

The above plasma model assumes that the electric field is monotonic in each half channel. This condition is no longer valid when the electric field in the sheath becomes zero at the wall boundary, i.e. $d\phi/dr|_W = 0$, which is known at the charge saturation limit [9]. The integration the Poisson equation across the sheath shows that the condition $d\phi/dr|_W \leq 0$ is equivalent to

$$\int_{\phi_W}^{\phi_Q} e(n_i - n_e)d\phi \geq 0, \tag{B.38}$$

that is the net electric charge inside a monotonic sheath is non-negative. This equation, detailed in the Appendix, will be used to determine the CSL. The plasma response beyond the CSL [54] is not considered in this paper.

B.4   Results

The main magnitudes of plasma-wall interaction affecting Hall thruster performances are: (i) the plasma flux to the wall, g_i ($= g_e$), Eq.(B.32), which is recombined and requires to be reionized; (ii) the deposition of electron energy, q_{eW}, which is the main source of plasma-cooling and wall-heating; and (iii) the ion energy flux into the wall,

$$q_{iW} = \left(m_i u_{iQ}^2/2 + e\phi_{WQ}\right) g_i, \tag{B.39}$$

which, apart from producing additional wall heating, is the responsible for wall sputtering. The present radial model gives information only on the flux of radial energy $q_{iW,r} = \left(m_i u_{riQ}^2/2 + e\phi_{WQ}\right) g_i$.

B.4.1   Influence of the thermalization level

Figure B.3 depicts, for the simplest SEE model ($\delta_{sr} = 0$ and $T_2/T_1 \ll 1$), the combined influence of the electron thermalization level, σ, and SEE cross-over energy, $E_1(= E_b)$, on the main plasma-wall variables. Both parameters affect strongly the plasma response. The plasma flux $\hat{g}_i$, governed by Bohm condition, remains close to one always (except for $\sigma \to 0$). The sheath potential fall, $\hat{\phi}_{WQ}(\sigma)$, presents a maximum for an intermediate thermalization level. This behavior of $\hat{\phi}_{WQ}$ is easy to understand from Eq.(B.33): The first factor in the right-hand-side of Eq.(B.33) is large (~ 200 for xenon), the second one is the effect of partial thermalization on the primary electron population, and the last one is the contribution of secondary, beam electrons. Therefore, for any of the last two factors to affect the value of ϕ_{WQ} significantly, they must be small. This occurs for either $\sigma \ll 1$, i.e. the low-thermalization limit, or $1 - \gamma_{bp} \ll 1$, which corresponds to the vicinity of the charge-saturation limit. The density of beam electrons at the sheath edge (and in the bulk region) is negligible. A partial exception is at the CSL, where $\hat{n}_{bQ}$ is the responsible for the increment of $\hat{g}_i$.

The most dramatic dependence with σ corresponds to the deposition of electron energy, q_{eW}, which increases from $q_{eW}/2T_1 g_i \simeq 1$ at $\sigma \ll 1$ to $q_{eW}/2T_1 g_i \simeq 100$ at the CSL. This increment is due to the increase of the flux of primary electrons g_p, Eq.(B.32). The evolution of $q_{iW,r}(\sigma)$ follows that of ϕ_{WQ}, with a maximum at an intermediate thermalization level (which can lead to maximum wall sputtering there).

In our first approach to this model [57], we assumed a constant-frequency model (i.e. $\lambda_{ther}/v_{re} = $ const) instead of a constant-mean-free-path one. It can be checked now that both models lead to the same trends in the solution, with the present model working with much simpler expressions.
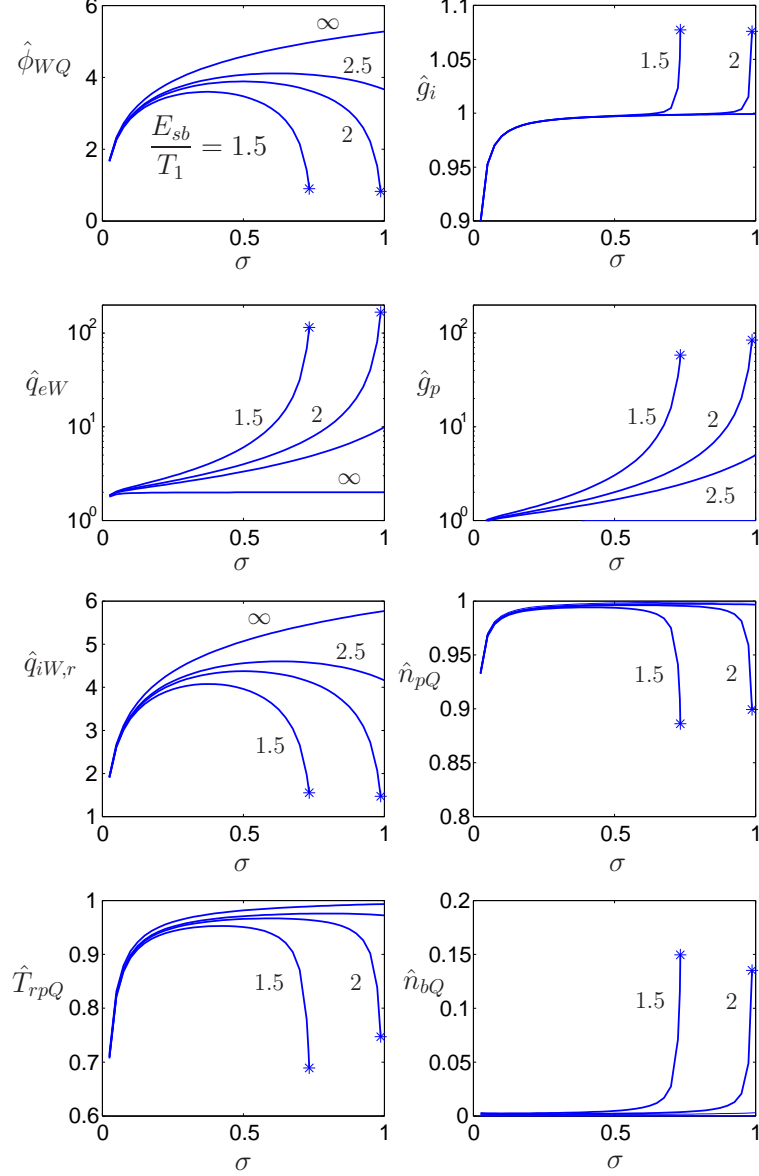
Figure B.3: Influence on the plasma-wall response of the electron thermalization level and SEE cross-over energy for $E_b/T_1 = 1.5$, 2, 2.5, and ∞, $T_2/T_1 = 0.01$, and $\delta_{sr} = 0$ (thus $E_1 = E_b$). Asterisks correspond to the CSL. This and following figures are for xenon ($\sqrt{m_i/m_e} \simeq 490$).

B.4.2 Influence of the emission model

Figure B.4 shows the effect of a finite temperature of true-secondary electrons, T_2. The increase of T_2/E_b yields a larger δ_{sb} and thus a larger γ_{bp}. This leads to larger g_p and q_{eW}, and lower ϕ_{WQ}. The exception is $\sigma \simeq 1$, when the only effect of increasing T_2 is to reduce q_{eW}. The

parameter T_2/E_b is small always and we expect solutions for $T_2/E_b \simeq 0$ to yield errors of order $O(T_2/E_b)$. In Sec. VI we will see that this is no longer true for the CSL, where errors are of order $O(\sqrt{T_2/E_b})$.
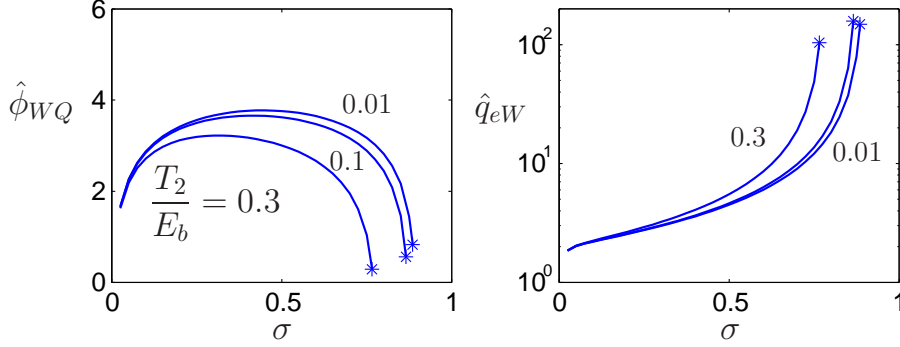
Figure B.4: SEE model. Effect of the emission energy of 'true-secondary' electrons: $T_2/E_b = 0.01$, 0.1, and 0.3; $E_b/T_1 = 1.8$ and $\delta_{sr} = 0$. Asterisks correspond to the CSL.

The presence of elastically reflected electrons modifies the sheath parameters more deeply, since these electrons are hot and δ_{sr} is not small always. Figures B.5(a)-(d) show the effect of a SEE yield with a 0-60% fraction of elastically reflected electrons. Notice that the plots differ on the SEE energy that is kept constant: $\hat{E}_b$ in Figs. 5(a)-5(b) and $\hat{E}_1 = (1 - \delta_{sr})\hat{E}_b$ in Figs. 5(c)-5(d). The different plasma behavior is due to $\partial \gamma_{bp}/\partial \delta_{sr}$ being positive for $\hat{E}_b = $ const, and negative for $\hat{E}_1 = $ const. This illustrates that in order to understand correctly the plasma response we must interpret first the role and relevance of the several plasma conditions and parameters. The analysis shows that the zero-electric-current and Bohm conditions are those affecting the most the plasma response. Since g_i varies weakly, the key parameter (for T_2/E_b small) is the relative beam-to-primary net electron flux, $\gamma_{bp} \equiv g_p/g_b$, which, through Eq.(B.32), self-determines the primary flux g_p and therefore the energy losses q_{eW}. The sheath potential fall, Eq.(B.33, is then self-adjusted in order the wall collects the appropriate flux of primary electrons.

Up to here we have assumed $\delta_{sr}(E) = $ const in order to obtain simple relationships among the parameters that facilitate their interpretation. There is no difficulty in obtaining results with E_r finite in Eq.(B.12): expressions for g_p and γ_{bp} just keep their integral form. Figure B.6 plots some solutions with E_r finite. As expected there are no qualitative changes with respect to the case $\delta_{sr} = $ const. This leads us to propose an approximate emission model that keeps the dependence of δ_{sr} on the energy of impacting electrons but profit simultaneously from the simple expressions of Secs. II and III. The idea is to substitute the 'exact' yield $\delta_{sr}(E)$ by an 'average' one, $\tilde{\delta}_{sr}$, which depends directly on the main electron temperature T_1. A satisfactory enough agreement is reached using the approximate SEE yield

$$\tilde{\delta}_{sr}(T_1) = \delta_0 \frac{E_r^2}{(E_r + T_1)^2} \tag{B.40}$$

in the analytical expressions of Secs. II and III. The dashed lines of Fig.B.6 correspond to this approximate model.
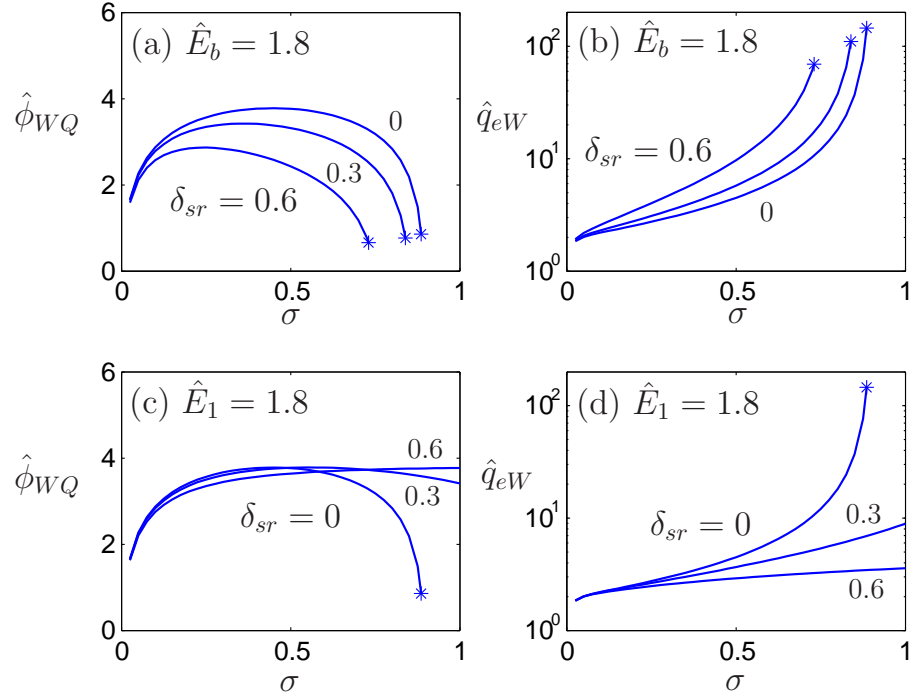
Figure B.5: SEE model. Effect of the presence of elastically-reflected electrons: $\delta_{sr} = 0$, 0.3 and 0.6; $T_2/T_1 = 0.01$; and $E_b/T_1 = 1.8$ in (a)-(b), $E_1/T_1 = 1.8$ in (c)-(d). Asterisks correspond to the CSL.

B.5 The low-thermalization limits

For total thermalization, the present model recovers the results of Ref. [10]. The case of low thermalization is of special interest here because (i) it presents important differences with total thermalization, (ii) it admits some asymptotic expressions; and (iii) it could be the appropriate one for Hall-thruster discharges (a value of $\sigma \sim 1\%$ is suggested in Ref.[56], which, for $T_1 = 30\text{eV}$ and a chamber width of 15mm, corresponds to a thermalization frequency of $\sim 2.4 \times 10^6 \text{s}^{-1}$).

Let us analyze now how low-thermalization of beam and primary electrons affect in a different way the plasma response. For $\sigma \ll 1$, the effective secondary yields are

$$\gamma_{bp} \simeq \frac{\sigma}{1 - \delta_{sr}}\gamma_{2p}, \qquad \gamma_{2p} \simeq \frac{2T_1}{E_b - 2T_2}. \tag{B.41}$$

Therefore, independently of the emission of beam electrons (γ_{2p}) being small or large, low thermalization makes the two counter-streaming SEE beams of almost equal current and leads
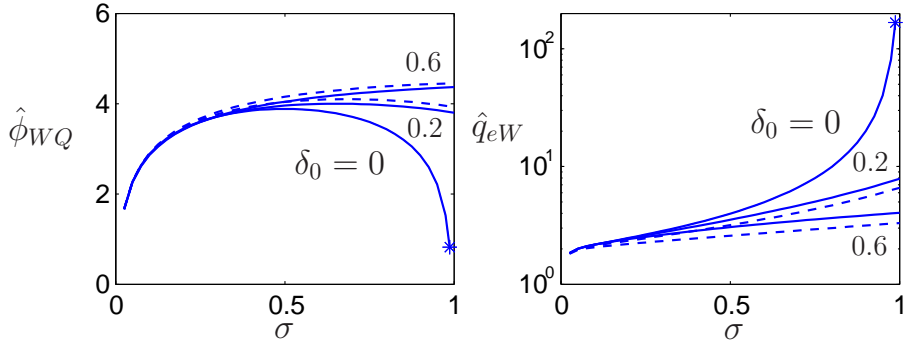
Figure B.6: SEE model. Effect of $\delta_{sr}(E) = \delta_0 \exp(-E/E_r)$ for $\delta_0 = 0$, 0.2, and 0.6, $E_r/T_1 = 2$, $(1 - \delta_0)E_b/T_1 = 2$, and $T_2/T_1 = 0.01$. Dashed lines correspond to use the approximate function $\tilde{\delta}_{sr}(T_1)$ of Eq.(B.40). Asterisks correspond to the CSL.

to an effective beam-to-primary flux ratio, γ_{bp}, very small [35]. The consequences are $g_p \simeq g_i$ and $q_{eW} \simeq 2T_1 g_i$, that is energy losses at their minimum. On the other hand, the sheath potential fall satisfies

$$\hat{\phi}_{WQ} \simeq \ln\left(\frac{\sigma}{\hat{g}_i} \sqrt{\frac{m_i}{2\pi m_e}} \right). \tag{B.42}$$

Here, the factor σ is measuring the depletion of the tail of primary electrons impinging the wall; $\sigma \ll 1$ indicates that a lower $\hat{\phi}_{WQ}$ is needed to adjust the electron flux to the ion flux. In addition, $\gamma_{bp} \ll 1$ makes that SEE beams do not affect the sheath potential fall.

The behavior of $\hat{\phi}_{WQ}$ for very low thermalization is not immediate since Eq. (B.49) indicates that $\hat{g}_i \to 0$ goes to zero when $\hat{\phi}_{WQ} \to 0$. From Eqs. (B.33), and (B.47)-(B.49), the asymptotic plasma behavior for the 'very-low thermalization limit'(VLTL),

$$\sigma' = \sigma(m_i/m_e)^{1/2} \ll 1, \tag{B.43}$$

is

$$\hat{g}_i \simeq \frac{\sigma'}{\sqrt{2\pi}}, \quad \hat{\phi}_{WQ} \simeq \frac{\sigma'}{4}, \quad \hat{n}_{eQ} \simeq \hat{n}_{pQ} \simeq \sqrt{\frac{\sigma'}{2}}, \quad \hat{T}_{rpQ} \simeq \frac{\sigma'}{6}. \tag{B.44}$$

Figure B.7 shows the evolution of these parameters in the low and very-low σ ranges. Notice that as long as $\sigma \geq O(m_e/m_i)^{1/2} \sim 2 \cdot 10^{-3}$, the order of magnitude of the main plasma parameters remains unchanged. Only in the VLTL, one can say that there is a strong depletion of the EVDF, leading to T_{rpQ}/T_1 clearly below 1. It is interesting to observe that, for the VLTL, the ion velocity at the entrance of the sheath satisfies

$$m_i u_{riQ}^2 \simeq 3T_{rpQ}. \tag{B.45}$$

Therefore, at the VLTL, the Bohm condition is preserved but the relevant temperature is the parallel to the magnetic field. The factor 3 is due to the strong distortion of the EVDF shape from a Maxwellian one and would indicate a one-dimensional adiabatic behavior.
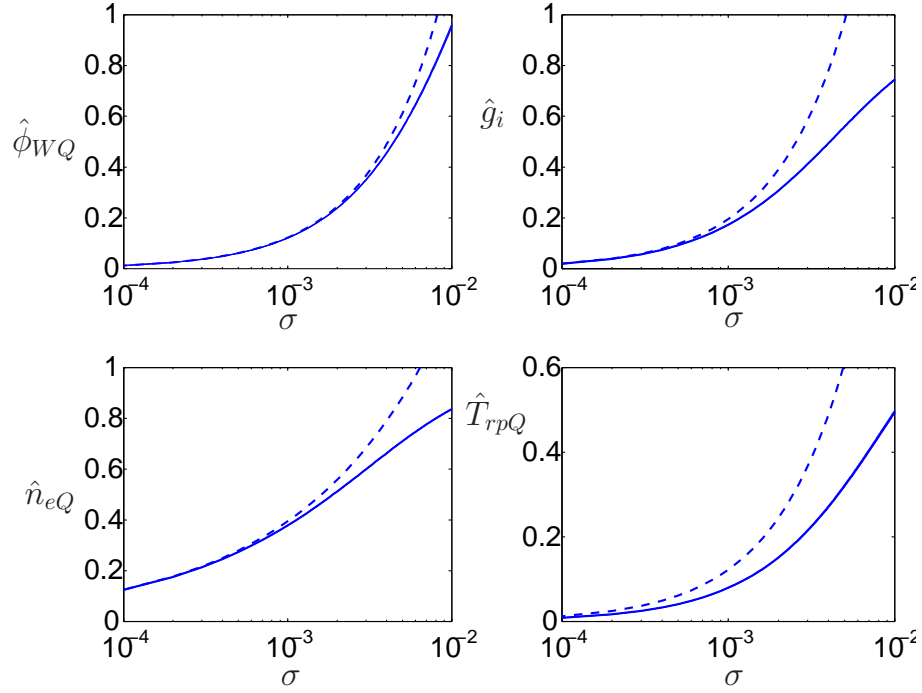
Figure B.7: Low thermalization limit. Same four cases than in Fig.B.3. Dashed lines correspond to the very-low thermalization limit, Eqs. (B.44).

B.6   The charge saturation limit

This limit is the transition to a non-monotonic structure of the Debye sheath [54]. Its importance here lies in that it sets a local minimum of the sheath potential fall and a maximum of deposition of (dimensionless) electron energy. The CSL is defined by condition (B.50). The numerical computations confirm that, in order to reach the CSL, the flux of primary electrons must be much larger than the ion flux (i.e. $g_p/g_i \gg 1$), which means that the beam and primary fluxes are very similar, that is $\gamma_{bp} \simeq 1$ in Eq.(B.32). The ratio g_p/g_i is plotted in Fig.B.8, together with main plasma magnitudes at the CSL; an asterisk is used as superscript for parameters at the CSL.

The temperature of primary electrons (T_1) leading to sheath charge-saturation can be obtained from the approximation $\gamma_{bp} = 1$. Solving this equation for T_1 and using Eqs.(B.13) and (B.40), one has

$$2\frac{T_1^*}{E_1} \simeq \frac{1}{\sigma} + \frac{\delta_{sr}^*}{1 - \tilde{\delta}_{sr}^*} - \frac{(1-\sigma)(1-\tilde{\delta}_{sr}^*)}{\sigma}2\frac{T_2}{E_1}, \tag{B.46}$$

with $\tilde{\delta}_{sr}^* = \tilde{\delta}_{sr}(T_1^*)$. This expression is explicit for T_1^* only if the yield for backscattered electrons, $\tilde{\delta}_{sr}(T_e)$, is constant. Figure B.8 and Eq.(B.46) show that the plasma temperature T_1^* required to reach the CSL decreases as: a) electron thermalization in the bulk of the plasma (i.e. σ) increases; b) the average SEE yield is higher (i.e. E_b is lower); or c) the 'average' temperature of the SEE increases (i.e. either δ_{sr} or T_2 increase). For typical values of E_b, T_2 and T_1 in Hall thrusters, the CSL is unattainable for low thermalization [say for $\delta_{sr} \geq 0.3$ and $\sigma \leq 0.20$ (i.e $\lambda_{ther}/h > 4.5$)]. A second positive aspect of low thermalization and CSL is that energy losses
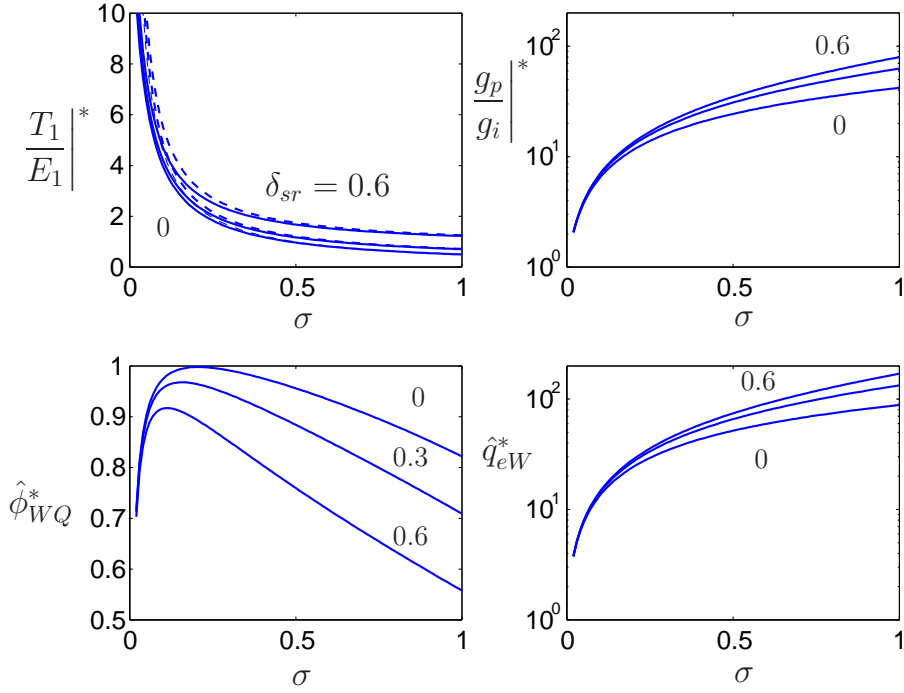
Figure B.8: Charge saturation limit. Variation of main parameters with σ for $\delta_{sr} = 0$, 0.3, 0.6; other parameters: $T_2/T_1 = 0.1$. Dashed lines for T_1^* correspond to Eq.(B.46).

are typically one order of magnitude less than for total thermalization. The CSL behavior obtained here is the same obtained in Ref. [35] (for $\delta_{sr} = 0$) except for the value of potential fall, $\hat{\phi}_{WQ}^*$, which was larger there since the depletion of primary population was not taken into account.

The approximation $\gamma_{bp} = 1$ cannot be used, of course, to compute the large values of parameters $(g_p/g_i)^*$ and $(q_{eW}/2T_1 g_i)^*$, Eq.(B.32), and the potential fall at the CSL, $\hat{\phi}_{WQ}^*$, Eq.(B.33). The importance of computing exactly enough $(g_p/g_i)^*$ is illustrated in Table I, which compares the results of the Hobbs-Wesson model with ours. The case treated by these authors corresponds to $\sigma = 1$, $\delta_{sr} = 0$, and $T_2/T_1 = 0$, *except that* they computed the density of primary electrons, n_p, using the complete Maxwellian distribution (including the empty tail of electrons collected by the wall). This inconsistency would not be important if the potential fall at the CSL was large, but Table I shows that it leads to errors of 20% on $(g_p/g_i)^*$ and the deposition of electron energy. The influence of the temperature T_2 of beam electrons on $(g_p/g_i)^*$ is also worth to comment. In most of the Hall thruster chamber, the ratio T_2/T_1 is of the order of 0.1, which makes plausible to treat the 'beam secondary' population as cold [9, 10] (except in the very vicinity of the wall). Errors on energy deposition and sheath potential fall are expected to be of order T_2/T_1. This turns out to be true *except for* the CSL, when they are of order $\sqrt{T_2/T_1}$, as Eq.(B.52) explains and Table I illustrates. Therefore, 'small' contributions (or details) of the electron model have a significant effect on the plasma parameters at the CSL.

	$(g_p/g_i)^*$	$(q_{eW}/2T_1 g_i)^*$	$\hat{\phi}_{WQ}^*$	$\hat{g}_i^*$
FM, $\hat{T}_2 = 0$	59.7	59.7	1.02	1.08
CM, $\hat{T}_2 = 0$	74.1	74.1	0.91	1.03
CM, $\hat{T}_2 = 0.01$	79.8	79.0	0.82	1.04
CM, $\hat{T}_2 = 0.1$	94.5	85.1	0.63	1.06

TABLE 1. CSL parameters. FM stands for the full-Maxwellian distribution assumed by Hobbs and Wesson; CM stands for the corrected-Maxwellian with the empty tail of collected electrons. Other parameters: $\sigma = 1$ and $\delta_{sr} = 0$.
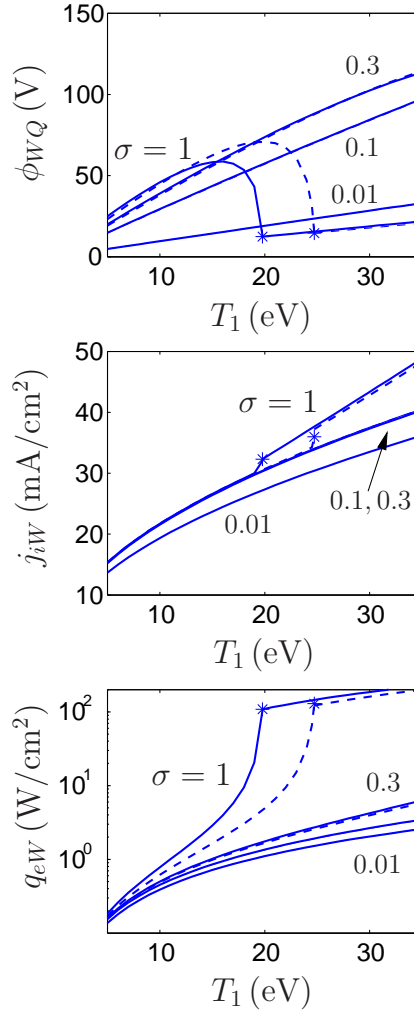
Figure B.9: Main plasma-wall parameters (sheath potential fall, ion current to wall, and electron energy deposition at walls) as function of the perpendicular temperature of primary electrons T_1 for: different thermalization levels (σ_1 =0.01,0.1,0.3, and 1); $n_{eQ} = 3 \cdot 10^{17} \text{m}^{-3}$; $E_1 = 40\text{eV}$; $T_2 = 2\text{eV}$; and $\delta_{sr} = 0$ (solid lines), $\delta_0 = 0.45$ and $E_r = 50\text{eV}$ (dashed lines). The region to the right of the asterisk for the solid curve of $\sigma = 1$ corresponds (approximately) to the charge-saturation regime.

B.7   A practical example and additional considerations

Figures B.3 to B.8 have presented dimensionless curves which allow to evaluate the relevance of the different aspects of the model. In order to complete the illustration of the influence of partial thermalization, Fig.B.9 presents dimensional results for typical plasma values of a conventional stationary plasma thruster(SPT) of the 1-2kW range [63] and lateral walls made of Boron Nitride; the SEE data for this material has been taken from Ref.[55]. A crossover energy E_1 of 40 eV is taken, and solid and dashed lines differ on the contributions of true-secondary and elastically-reflected electrons. Thermalization levels from $\sigma = 0.01$ to $\sigma = 1$ are considered; for a chamber width of $h = 15$mm and electron energies of 50eV, the range $\sigma = 10^{-2} - 10^{-1}$ corresponds to mean free paths of $0.14 - 1.4$m and thermalization frequencies of $2 \cdot 10^6 - 2 \cdot 10^7 \mathrm{s}^{-1}$. Figure B.9 plots the sheath potential fall, the ion/electron current to the wall, and the electron energy deposited at the wall; ion energy losses follow the trends of the sheath potential fall. Notice that particle and energy fluxes to the wall are proportional to the plasma density at the sheath edge, n_{eQ} (which is about a 50-60% of the electron density at the channel median). The plots shows that the thermalization level is very crucial when estimating plasma-wall parameters. In particular electron energy losses can vary by two orders of magnitude, but for the range of temperatures of interest, the large electron energy losses at the charge-saturation regime(CSR) are attained only if the thermalization level is high. On the other hand, the presence of a significant fraction of 'hot' backscattered electrons (i.e. dashed lines) has a secondary effect, except for the retardation of the CSL at high thermalization. These are positive news for modelling since the uncertainties on the distribution function of secondary electrons are large. The values of ion current to the wall in Fig.B.9 are of the order of those measured by Kim et al.[63]. As explained before, the ion current into sheath and wall depends mainly on the plasma physics in the bulk region, and is weakly affected by the thermalization level and the SEE details. The reduction of the ion current for $\sigma = 0.01$ is due to the a decrease of the effective parallel temperature of primary electrons; the increase of the ion current for $\sigma = 1$ at the CSR is the effect of an increase of the secondary beam density (see $\hat{n}_{bQ}$ in Fig.B.3).

The curves for $\sigma = 1$ and $\delta_{sr} = 0$ in Fig.B.9 correspond to the model presented in Ref.[10] and implemented now in the simulation code HPHall-2 of the plasma discharge[3]. There are no difficulties on implementing the five-parameter SEE model proposed here in the simulation code, but we can predict that changes are going to be limited. However, the implementation of a partial thermalization model for electrons in the simulation code is far more challenging. The electron fluid model currently implemented in HPHall-2 (and in other hybrid codes) for the bulk, quasineutral region is based on a one-temperature, quasi-Maxwellian electron distribution. An electron fluid-type model for low thermalization requires to assume (i) a two-temperature distribution for primary electrons. and (ii) an independent distribution for the true-secondary electron beams. This implies, at least, to postulate (i) conditions relating the parallel and perpendicular temperatures of primary electrons, (ii) equations for the macroscopic magnitudes of beam electrons, and (iii) source terms 'transforming' beam electrons into primary ones. An additional, important challenge is that the fluid equations for magnetized electrons must be expressed in the non-cartesian reference frame linked to the curved magnetic streamlines.

Therefore, we believe that there are several important issues related to the evolution of secondary electrons that remain largely unsolved. These should be understood prior to affording

the implementation of a new electron model in codes such as HPHall-2. First, the determination and evaluation of the main physical processes that thermalize (or isotropize) the EVDF are poorly known. Second, Sydorenko et al. [64] have shown recently that the two-stream instability can 'heat' and trap an important fraction of the secondary beams, thus indicating the existence of a *trapping* process for secondary electrons independent of the *thermalization* of the primary EVDF (modelled through σ). Third, a consistent model for trapped secondary electrons and their 'thermalization' into primary electrons (in a slower time-scale) must be derived. And fourth, the fluid model of the secondary beams should take into consideration the different magnetic effects acting on them, such as the $E \times B$ and curvature drifts, magnetic mirror trapping, and the oblique incidence of the magnetic field.

B.8   Conclusions

A model of the plasma interaction with the dielectric walls of a Hall thruster has been presented. It accounts for partial thermalization of the electron population through a single parameter σ and includes a two-population, four-parameter model for SEE. Analytical expressions are obtained for the main parameters characterizing that interaction, such as the particle and energy fluxes to the walls and sheaths, which are needed as boundary conditions of quasineutral models of the full discharge.

The behavior for low thermalization is shown to differ greatly from the commonly-used, high-thermalization case. This is very relevant for Hall thrusters, where there is a growing conviction that electron thermalization is low (at least for primary electrons). At low thermalization, energy losses are close to its minimum, the charge saturation limit is not attainable, and the sheath potential is small; the different roles of beam and primary electrons on these characteristics have been analyzed. Significant decreases of the parallel temperature of primary electrons and, therefore, of the plasma flux into the sheath (through fulfilment of the Bohm condition) take place only at the very-low thermalization limit ($\sigma \ll \sqrt{m_e/m_i}$).

The investigation of the emission model for secondary electrons has shown that the presence of a relevant fraction of elastically reflected electrons affects greatly the response. They tend to amplify the relative densities of untrapped electrons; their effect on the net primary and beam fluxes comes out from the zero electrical current balance. It is reiteratively found that the role of the sheath potential fall is to adjust the primary electron flux to wall and not viceversa. Although most of the analysis is carried out for an energy-independent yield of reflected electrons, a temperature-dependent yield expression is proposed, which avoids integrals expressions at the same time that it recovers approximately the reduction of that yield with the impact energy.

The charge saturation limit is attained when net beam-to-primary net fluxes ratio, γ_{bp}, is very close to one, that is the ratio between the primary-electron to ion flux ratio, $g_p/g_i \equiv (1 - \gamma_{bp})^{-1}$, is very large. The CSL requires larger plasma temperatures as the thermalization decreases and the average yield of reflected electrons increases. Additionally, the sensitivity of the value of g_p/g_i at the CSL to small variations on the model properties has been stood out. As examples we have shown that the influence of a small emission energy of true-secondary electrons (T_2) or the (inconsistent) inclusion of the collected tail of primary electrons are less marginal than what could be expected.

Appendix: electron magnitudes in the sheath

The electron density $n_e(\phi) = \int d\boldsymbol{v} f(\phi, \boldsymbol{v})$ has contributions from primary and beam electrons. Using Eq.(B.20) for the EVDF and writing $\hat{n}_e = \hat{n}_p + \hat{n}_b$, one has

$$
\begin{aligned}
\hat{n}_p(\hat{\phi}) &= \mathrm{e}^{\hat{\phi} - \hat{\phi}_Q} \left[1 - \frac{2 - (1 + \delta_{sr})\sigma\kappa}{2} \mathrm{erfc}\sqrt{\hat{\phi} - \hat{\phi}_W} \right], \\
\hat{n}_b(\hat{\phi}) &= \frac{\mu_b}{2} \sqrt{\frac{T_1}{T_2}} \mathrm{e}^{-\hat{\phi}_{WQ}} \mathrm{e}^{(\hat{\phi} - \hat{\phi}_W)/\hat{T}_2} \mathrm{erfc}\sqrt{(\hat{\phi} - \hat{\phi}_W)/\hat{T}_2},
\end{aligned}
\tag{B.47}
$$

with $\mu_b \equiv (2 - \sigma)(1 - \delta_{sr})\kappa\gamma_{bp}$.

The parallel-to-perpendicular temperature ratio of the primary population at point Q, is of interest also. It is readily seen that the perpendicular temperature is T_1. Then, the temperature ratio, $\hat{T}_{rpQ}$, satisfies

$$
\hat{T}_{rpQ}\hat{n}_{pQ} \;\simeq\; \int \frac{m v_r^2 f_{pQ}}{n_1 T_1} d^3 v \;=\; 1 - \left[(1 + \delta_{sr})\frac{\sigma\kappa}{2} - 1 \right] \left(2\frac{\hat{\phi}_{WQ}^{1/2}}{\pi^{1/2}} \mathrm{e}^{-\hat{\phi}_{WQ}} + \mathrm{erfc}\,\hat{\phi}_{WQ}^{1/2} \right), \quad \text{(B.48)}
$$

where the integration domain is the whole velocity space and the small contribution of the macroscopic radial kinetic energy of electrons has been neglected.

Using the above expressions for the electron densities, the sonic Bohm condition (B.37) for $\hat{g}_i$ becomes

$$
\frac{\hat{n}_{eQ}^3}{\hat{g}_i^2} = \hat{n}_{pQ} + \hat{n}_{bQ}\frac{T_1}{T_2} + \left[2 - (1 + \delta_{sr})\sigma\kappa - \mu_b\frac{T_1}{T_2} \right] \frac{\mathrm{e}^{-\hat{\phi}_{WQ}}}{2\sqrt{\pi\hat{\phi}_{WQ}}}.
\tag{B.49}
$$

Finally, the 3 contributions to the CSL condition,

$$
\int_W^Q [\hat{n}_i - \hat{n}_p - \hat{n}_b]\, d\hat{\phi} = 0,
\tag{B.50}
$$

are

$$
\begin{aligned}
\int_W^Q \hat{n}_i\, d\hat{\phi} &= \left(\sqrt{\hat{g}_i^2 + 2\hat{\phi}_{WQ}\hat{n}_{eQ}^2} - \hat{g}_i \right) \frac{\hat{g}_i}{\hat{n}_{eQ}}, \\
\int_W^Q \hat{n}_p\, d\hat{\phi} &= \hat{n}_{pQ} - \hat{n}_{pW} - \frac{2 - (1 + \delta_{sr})\sigma\kappa}{\sqrt{\pi}} \mathrm{e}^{-\hat{\phi}_{WQ}} \hat{\phi}_{WQ}^{1/2}, \\
\int_W^Q \hat{n}_b\, d\hat{\phi} &= (\hat{n}_{bQ} - \hat{n}_{bW})\frac{T_2}{T_1} + \frac{\mu_b}{\sqrt{\pi}} \mathrm{e}^{-\hat{\phi}_{WQ}} \hat{\phi}_{WQ}^{1/2}.
\end{aligned}
\tag{B.51}
$$

For $T_2/T_1 \ll 1$ (and $\hat{\phi}_{WQ} \sim 1$), one has

$$
\int_W^Q \hat{n}_b\, d\hat{\phi} \simeq \mu_b \mathrm{e}^{-\hat{\phi}_{WQ}} \left[\sqrt{\frac{\hat{\phi}_{WQ}}{\pi}} - \frac{1}{2}\sqrt{\frac{T_2}{T_1}} \right].
\tag{B.52}
$$

Bibliography

[1] D. Escobar, A. Antón, and E. Ahedo. Simulation of high-specific-impulse and double-stage Hall thrusters. In *Proc. 29th International Electric Propulsion Conference, Princeton, USA*, IEPC-2005-040. Electric Rocket Propulsion Society, Fairview Park, OH, 2005.

[2] D. Escobar, E. Ahedo, and F. I. Parra. On conditions at the sheath boundaries of a quasineutral code for Hall thrusters. In *Proc. 29th International Electric Propulsion Conference, Princeton, USA*, IEPC-2005-041. Electric Rocket Propulsion Society, Fairview Park, OH, 2005.

[3] F.I. Parra, E. Ahedo, M. Fife, and M. Martínez-Sánchez. A two-dimensional hybrid model of the Hall thruster discharge. *Journal of Applied Physics*, 100:023304, 2006.

[4] E. Ahedo and M. Martínez-Sánchez. One-dimensional plasma structure in Hall thruster. In *Proc. 34th Joint Propulsion Conference, Cleveland, OH*, AIAA-98-8788. American Institute of Aeronautics and Astronautics,Washington, DC, 1998.

[5] E. Ahedo, J.M. Gallardo, and M. Martínez-Sánchez. Model of the plasma discharge in a Hall thruster with heat conduction. *Physics of Plasmas*, 9(9):4061–4070, 2002.

[6] E. Ahedo. On the near anode region of the Hall thruster discharge. In *Proc. 40th Joint Propulsion Conference, Fort Lauderdale, FL*, AIAA 2004-3774. American Institute of Aeronautics and Astronautics,Washington, DC, 2004.

[7] L. Dorf, V. Semenov, and Y. Raitses. Anode sheath in Hall thrusters. *Applied Physics Letters*, 83(13):2551 – 2553, 2003.

[8] E. Ahedo and J.Rus. Vanishing of the negative anode sheath in a Hall thruster. *Journal of Applied Physics*, 98:043306, 2005.

[9] G.D. Hobbs and J.A. Wesson. Heat flow through a Langmuir sheath in the presence of electron emission. *Plasma Physics*, 9:85–87, 1967.

[10] E. Ahedo. Presheath/sheath model of a plasma with secondary emission from two parallel walls. *Physics of Plasmas*, 9(10):4340–4347, 2002.

[11] R. R. Hofer and A. D. Gallimore. Efficiency Analysis of a High-Specific Impulse Hall Thruster. In *40th Joint Propulsion Conference, Fort Lauderdale, FL*, AIAA-2004-3602. American Institute of Aeronautics and Astronautics,Washington, DC, 2004.

[12] F. Parra, E. Ahedo, M. Martínez-Sánchez, and J.M. Fife. Improvement of the plasma-wall model on a fluid-PIC code of a Hall thruster. In *SP-555: 4th Spacecraft Propulsion Conference, Sardinia (Italy)*. European Space Agency, Noordwijk, The Netherlands, 2004.

[13] A. Antón, D. Escobar, and E. Ahedo. Contour algorithms for a Hall thruster hybrid code. In *42th Joint Propulsion Conference, Sacramento, CA*, AIAA-2006-4834. American Institute of Aeronautics and Astronautics,Washington, DC, 2006.

[14] D. Escobar and E. Ahedo. Improved electron formulation for a Hall thruster hybrid model. In *42th Joint Propulsion Conference, Sacramento, CA*, AIAA-2006-4326. American Institute of Aeronautics and Astronautics,Washington, DC, 2006.

[15] F.I. Parra and E. Ahedo. Fulfillment of the Bohm condition on the HPHall fluid-PIC code. In *Proc. 40th Joint Propulsion Conference, Fort Lauderdale, FL*, AIAA 2004-3955. American Institute of Aeronautics and Astronautics,Washington, DC, 2004.

[16] J. M. Fife. *Hybrid-PIC Modeling and Electrostatic Probe Survey of Hall Thrusters*. PhD thesis, Massachusetts Institute of Technology, 1998.

[17] C.K. Birdsall and A.B. Langdon. *Plasma Physics via Computer Simulation*. Institute of Physics Publishing, Bristol, 1991.

[18] J.P. Verboncoeur. Symmetryc spline weighting for charge and current density in particle simulation. *J. Computational Physics*, 174:421 –427, 2001.

[19] J.P. Verboncoeur K.L. Cartwright and C.K. Birdsall. Loading and injection of Maxwellian distributions in particle simulations. *Journal of Computational Physics*, 162:483–513, 2000.

[20] F.I. Parra. Actualización y mejora de un código pic-fluido bidimensional para el flujo de plasma en motores de efecto hall. Master's thesis, Escuela Técnica Superior de Ingenieros Aeronáuticos, Universidad Politécnica de Madrid, 2004.

[21] E. Ahedo, J.M. Gallardo, and M. Martínez-Sánchez. Effects of the radial-plasma wall interaction on the axial Hall thruster discharge. *Physics of Plasmas*, 10(8):3397–3409, 2003.

[22] J.A. Bittencourt. *Fundamentals of Plasma Physics*. Pergamon, Oxford, 1986.

[23] Y. Raitses, A.A. Litvak, L.A. Dorf, and N.J. Fisch. Parametric investigations of segmented electrode Hall thruster . In *Electric Rocket Propulsion Society, Fairview Park, OH*, IEPC-99. 26th International Electric Propulsion, Kytakyushu, Japan, 1999.

[24] G.S. Janes and R.S. Lowder. Anomalous electron diffusion and ion acceleration in a low-density plasma. *Physics of Fluids*, 9(6):1115–1123, 1966.

[25] A.I. Morozov, Y.V. Esipchuk, G.N. Tilinin, A.V. Trofimov, Y.A. Sharov, and G.Y.Shchepkin. Plasma accelerator with closed electron drift and extended acceleration zone. *Soviet Physics-Tech. Physics*, 17(1):38–45, 1972.

[26] S. Barral, K. Makowski, Z. Peradzynski, N. Gascon, and M. Dudeck. Wall material effects in stationary plasma thrusters. II. Near-wall and in-wall conductivity. *Phys. Plasmas*, 10(10):4137 – 4152, 2003.

[27] M. Mitchner and C.H. Kruger Jr., editors. *Partially ionized gases.* Wiley, 1973.

[28] R.S.Jankovsky, D. T. Jacobson, C. J. Sarmiento, L. R. Piñero, D. H. Manzella, R. R. Hofer, and P. Y. Peterson. NASA's Hall thruster program 2002. In *38th Joint Propulsion Conference, Indianapolis, IN*, AIAA 2002-3675. American Institute of Aeronautics and Astronautics,Washington, DC, 2002.

[29] Y. Yamagiwa and K. Kuriki. Performance of double-stage-discharge Hall ion thruster. *J. Propulsion and Power*, 7(1):65–70, 1991.

[30] B. Pote and R. Tedrake. Performance of a high specific impulse Hall thruster. In *27th International Electric Propulsion Conference, Pasadena, CA, USA*, IEPC-01-035. Electric Rocket Propulsion Society, Fairview Park, OH, 2001.

[31] R.R. Hofer, P.Y. Peterson, A.D. Gallimore, and R.S. Jankovsky. A high specific impulse two-stage Hall thruster with plasma lens focusing. In *7th International Electric Propulsion Conference, Pasadena, CA, USA*, IEPC-01-036. Electric Rocket Propulsion Society, Fairview Park, OH, 2001.

[32] E. Ahedo and F.I. Parra. A model of the two-stage Hall thruster discharge. *Journal of Applied Physics*, 98:023303, 2005.

[33] N.B. Meezan and M.A. Capelli. Kinetic study of wall collisions in a coaxial Hall discharge. *Physical Review E*, 66:036401, 2002.

[34] O. Batishev and M. Martínez-Sánchez. Charge particle transport in the Hall effect thruster. In *Proc. 28th International Electric Propulsion Conference, Toulouse, France*, IEPC-03-188. Electric Rocket Propulsion Society, Fairview Park, OH, 2003.

[35] E. Ahedo and F.I. Parra. Partial trapping of secondary electron emission in a Hall thruster plasma. *Physics of Plasmas*, 12(7):073503, 2005.

[36] D. Escobar, A. Antón, and E. Ahedo. Simulation of high-specific-impulse and double-stage Hall thrusters. In *Proc. 29th International Electric Propulsion Conference, Princeton, USA*, IEPC-2005-040. Electric Rocket Propulsion Society, Fairview Park, OH, 2005.

[37] V.V. Zhurin, H.R. Kaufman, and R.S. Robinson. Physics of closed drift thrusters. *Plasma Sources Sci. Technol.*, 8:R1–R20, 1999.

[38] A.M. Bishaev and V. Kim. Local plasma properties in a Hall-current accelerator with and extended acceleration zone. *Sov. Physics-Tech. Physics*, 23(9):1055–1057, 1978.

[39] V. Kim. Main physical features and processes determining the performance of stationary plasma thrusters. *J. Propulsion Power*, 14(5):736–743, 1998.

[40] L. Dorf, Y. Raitses, and N. Fisch. Experimental studies of anode sheath phenomena in a Hall thruster discharge. *Journal of Applied Physics*, 97:103309, 2005.

[41] L. Dorf, Y. Raitses, and N. J. Fisch. Effect of magnetic field profile on the anode fall in a Hall-effect thruster discharge. *Physics of Plasmas*, 13:057104, 2006.

[42] L. Dorf, V. Semenov, Y. Raitses, and N.J. Fisch. Hall thruster modeling with a given temperature profile. In *38th Joint Propulsion Conference, Indianapolis, IN*, AIAA 2002-4246. American Institute of Aeronautics and Astronautics,Washington, DC, 2002.

[43] E.R. Harrison and W.B. Thompson. The low pressure plane symmetric discharge. *Proc. Physical Society of London*, 74:145–152, 1959.

[44] E. Ahedo. Structure of the plasma-wall interaction in an oblique magnetic field. *Physics of Plasmas*, 4:4419–4430, 1997.

[45] E. Ahedo, P. Martínez-Cerezo, and M. Martínez-Sánchez. 1-D performance analysis of a Hall thruster. In *SP-465: 3rd Spacecraft Propulsion Conference, Cannes (France)*, pages 323–330, Noordwijk, The Netherlands, 2000. European Space Agency.

[46] E. Ahedo and D. Escobar. Influence of design and operation parameters on Hall thruster performances. *Journal of Applied Physics*, 96(2):983–992, 2004.

[47] A.I Morozov and V.V. Savelyev. *Reviews of Plasma Physics*, volume 21, chapter 2. Kluwer Academic, New York, 2000.

[48] E. Ahedo, I. Maqueda, A. Antón, Y. Raitses, and N. Fisch. Numerical simulations of a 2kW Hall thruster. In *42th Joint Propulsion Conference, Sacramento, CA*, AIAA-2006-4655. American Institute of Aeronautics and Astronautics,Washington, DC, 2006.

[49] J. J. Szabo. *Fully kinetic numerical modeling of a plama thruster*. PhD thesis, Massachusetts Institute of Technology, 2001.

[50] K. Sullivan, J. Fox, O. Batischev, and M. Martínez-Sánchez. Kinetic study of wall effects in SPT. In *40th Joint Propulsion Conference, Fort Lauderdale, FL*, AIAA-2004-3777. American Institute of Aeronautics and Astronautics,Washington, DC, 2004.

[51] D. Sydorenko, A. Smolyakov, I. Kaganovich, and Y. Raitses. Kinetic simulation of secondary electron emission effects in Hall thrusters. *Physics of Plasmas*, 13:014501, 2006.

[52] S.A. Fridrikhov and A.R. Shulman. An investigation of the secondary electron emission by certain dielectrics at low primary electron energies. *Soviet Physics-Solid State*, 1:1153–1159, 1960.

[53] N.P Bazhanova, V.P. Belevskii, and S.A. Fridrikhov. Secondary electron emission from barium oxide and yttrium oxide due to low-energy primary electrons(1-100ev). *Soviet Physics-Solid State*, 3:1899–1905, 1962.

[54] V.L. Sizonenko. Effects of strong secondary electron emission on a plasma layer. *Sov. Phys. Tech. Phys*, 26(11):1345 –1350, 1981.

[55] F. Taccogna, S. Longo, and M. Capitelli. Plasma sheaths in Hall discharge. *Physics of Plasmas*, 12:093506, 2005.

[56] I.D. Kaganovich, Y. Raitses, D. Sydorenko, and A. Smolyakov. Kinetic Effects in Hall Thruster Discharge. In *42th Joint Propulsion Conference, Sacramento, CA*, AIAA 2006-4831. American Institute of Aeronautics and Astronautics, Washington GC, 2006.

[57] E. Ahedo, V. de Pablo, and M. Martínez-Sánchez. Effects of partial thermalization and secondary emission on the electron distribution function of Hall thrusters. In *Proc. 29th International Electric Propulsion Conference, Princeton, USA*, IEPC-2005-118. Electric Rocket Propulsion Society, Fairview Park, OH, 2005.

[58] E. Ahedo and V. de Pablo. Effects of electron secondary emission and partial thermalization on a Hall thruster plasma. In *42th Joint Propulsion Conference, Sacramento, CA*, AIAA-2006-4328. American Institute of Aeronautics and Astronautics,Washington, DC, 2006.

[59] P.L. Bhatnagar, E.P. Gross, and M. Krook. A model for collision processes in gases. I. Small amplitude processes in charged and neutral one-component systems. *Physical Review*, 94(3):511 – 525, 1954.

[60] V. Viel-Inguimbert. Secondary electron emission of ceramics used in the channel of SPT. In *28th International Electric Propulsion Conference, Toulouse, France*, IEPC-03-258. Electric Rocket Propulsion Society, Fairview Park, OH, 2003.

[61] A. Dunaevsky, Y. Raitses, and N. J. Fisch. Secondary electron emission from dielectric materials of a Hall thruster with segmented electrodes. *Physics of Plasmas*, 10(6):2574 – 2577, 2003.

[62] A.I. Morozov. Steady-state uniform Debye sheaths. *Sov. J. Plasma Physics*, 17(6):393–397, 1991.

[63] V. Kim, V.I. Kozlov, A.I. Skrylnikov, L.N. Umnitsin, V.V. Svotina, A. Bouchoule, and M. Prioul. Investigation of the Local Plasma Parameter Distributions in the SPT Accelerating Channel Under Increased Discharge Voltages. In *29th International Electric Propulsion Conference, Princeton, USA*, IEPC-2005-004. Electric Rocket Propulsion Society, Fairview Park, OH, 2005.

[64] D. Sydorenko, A. Smolyakov, I. Kaganovich, and Y. Raitses. Effects of non-Maxwellian electron velocity distribution function on two-stream instability in low-pressure discharges. *Physics of Plasmas*, 14:0134508, 2007.